# A First Principles Model-Based Study of Fuel Cell Gas Turbine Hybrid Power Sources for Transport Applications

Submitted to the University of Hertfordshire in partial fulfilment of the requirement of the degree of Doctor of Philosophy

Report by
Adrian Isidore Felix

School of Physics, Engineering and Computer Science

Principal Supervisor
Dr Christos Kalyvas

Secondary Supervisor
Dr Peter Thomas

Date
14/03/2024

# ABSTRACT

There are multiple types of power sources that can contribute to decarbonising transport including the adoption of battery electric vehicles (BEVs), fuel cell electric vehicles (FCEVs), hybrid FC-battery systems, hybrid gas turbine (GT)-battery systems, and Fuel Cell-Gas Turbine (FC-GT) hybrid systems. Each option has its advantages and challenges. Battery-only systems can provide zero emissions at the point of use but are limited by battery weight, energy density, and charging infrastructure. Fuel Cell-only systems can deliver clean energy with quick refuelling but may face challenges with hydrogen storage and infrastructure. Hybrid FC-Battery systems combine the benefits of both technologies, providing improved range and efficiency, but have very low power and energy density. GT-Battery systems can offer high power density but have lower efficiency than FC systems. Fuel Cell-Gas Turbine (FC-GT) systems combine the high efficiency of fuel cells with high power density and load following ability of gas turbines, making them suitable for applications where long range and high power are required. This study presents a First Principles Model-Based analysis FC-GT Hybrid Power Sources for Transport Applications, aiming to address the urgent need for sustainable energy solutions in the transportation sector.

The research focuses on Proton Exchange Membrane Fuel Cells (PEMFC) and Solid Oxide Fuel Cells (SOFC), exploring their potential integration with gas turbines to enhance electrical efficiency and reduce carbon emissions. PEMFCs, known for their operation below boiling point and high power density, have great potential as propulsive and auxiliary power sources in road and air transport. The electrical efficiency of a PEMFC can be improved by pressurising its air stream. Typically, this is done by a motor-driven compressor which draws power from the PEMFC and therefore reduces its usable power output. This parasitic loss can be reduced by the addition of a turbine at the PEMFC outlet that is driven by the fuel cell's exhaust gases and assists the compressor motor. Such a system is called a "Turbocharged PEMFC". SOFCs, which operate at high temperatures (500°C to 900°C) and high efficiency, are examined for their suitability in creating highly efficient propulsive power sources in marine and rail transport, as well as long-endurance air transport. The SOFC can be added to a Brayton cycle between the compression and combustion stages where fuel cell receives pressurised air from the compressor and the unutilised fuel from the SOFC is burned in the combustor.

FC-GT systems show good potential in various transport applications:

- *Aviation:* Both PEMFCs and SOFCs are considered for auxiliary power units (APUs) and potentially for primary propulsion in long endurance UAVs.
- *Road Transport:* PEMFCs are considered for use in passenger vehicles, buses, and trucks, where their high power density and quick refuelling capabilities provide significant advantages.
- *Marine:* SOFCs are explored for use in ships, where their high efficiency and ability to

utilise various fuels such as methanol and ammonia can significantly reduce emissions.

- *Rail:* SOFCs are also considered for trains, offering a cleaner alternative to diesel engines, especially for long-distance routes.

Beyond transport applications, FC-GT systems can also be used for stationary power generation for residential and industrial power generation, with SOFC-GT systems showing especially great potential in combined heat and power generation. However, the design considerations for stationary power and transport applications are different. For stationary applications, efficiency, longevity, and integration with existing infrastructure get the most emphasis and they can be larger and heavier. Transport applications require greater focus on factors like weight, volume, fuel storage, and dynamic load-following capabilities. These systems must be robust, reliable, and capable of operating under varying conditions. The design and development FC-GT system for transport applications is therefore more challenging as there are more design constraints and performance targets to meet. Modelling and simulation-based design plays an important role in making this challenging process quicker and more cost-effective.

The document details the development of agile, fast-solving models for simulating these hybrid systems in various transport applications. It begins with a literature review to identify optimal system configurations and proceeds with the design and implementation of these models. The performance of turbocharged PEMFC and SOFC-GT systems is analysed, demonstrating their potential to significantly contribute to the decarbonisation of the energy and transport sectors.
The study also delves into the challenges associated with hybrid system development, including thermal management, system integration, and the optimisation of operating parameters. These challenges can be tackled through analytical models based on first principles. Through analytical modelling and simulation studies, the research offers insights into the capabilities of FC-GT systems, providing recommendations for future work in the field.

This project sets a foundational step towards establishing an FC-GT research lab at the University of Hertfordshire, aiming to propel the design and optimisation of concepts and operating strategies for sustainable transport solutions. By addressing both technical and environmental challenges, the research underscores the potential of FC-GT hybrid systems in revolutionising power sources for transportation and other sectors, aligning with global decarbonisation goals.

# ACKNOWLEDGEMENTS

Firstly, I extend my profound appreciation to my supervisor, Dr Christos Kalyvas, for his invaluable guidance, unwavering support, and mentorship throughout this research journey. His expertise and insights have significantly shaped this work, and their encouragement has been a constant source of motivation.

I am very thankful to my second supervisor Dr Peter Thomas, for his constructive feedback, critical reviews, and helpful suggestions that immensely contributed to the refinement of this dissertation.

My gratitude extends to the faculty and staff of the School of Physics, Engineering and Computer Science whose support has been fundamental to my academic and professional development.

A special word of thanks goes to my fellow researchers Emre Ustun, Dawid Hnatyk, Hemant Joshi, Waruna Maddumage, and Dr Surya Maruthupandian for stimulating discussions, shared moments of challenges and triumphs, and most of all, friendship.

I am forever grateful to my parents, my brother, and the Maliyil family for their endless love, patience, and encouragement. Your belief in me has been my strength and inspiration.

# TABLE OF CONTENTS

# LIST OF FIGURES

# LIST OF TABLES

# 1 INTRODUCTION

The need for reducing the carbon footprint of the transport sector is a topic that needs little introduction. As of 2019, road transport accounts for 15.9% of global $CO_2$ emissions, while air and maritime transport accounts for 3.6% [1]. The UK has set out a target of reducing the country's carbon footprint by 60% during the period between 2002 and 2050 [2], and The Paris agreement of the United Nations Framework Convention on Climate Change (UNFCCC) set out targets of keeping the global average temperature below 2° C more than pre-industrial levels with member nations agreeing to pursue those targets post 2020 [3], [4]. To decarbonise transport and meet those targets, electric propulsion combined with electrochemical power sources and energy storage are gaining popularity as replacements for internal combustion engines and fossil fuels due to their lack of CO2 emissions and higher efficiency during operation [4], [5], [6], [7], [8] .

Fuel cells are devices that convert chemical energy of a fuel into electric power through an exothermic electrochemical reaction. In conventional cases, the heat released by the reaction is lost to the environment and hence, the concept of fuel cell - gas turbine hybrid has been gaining interest in academia and industry for a few decades now where the heat released from the fuel cell complements the heat added by combustion in a Brayton cycle [8], [9], [10]. However, the design and development of such systems is a challenging process due to the non-linear relationship between fuel cell performance and operating conditions, sizing of individual components depending on performance targets, need for accurate thermal control and electro-mechanical control, etc [6], [11], [12]. Finding remedies to these issues through iterative prototyping and physical testing can become very expensive and time consuming due to the complexities involved and therefore, model-based design and testing – which is more inexpensive and agile – plays an important role than usual in FC-GT system development [13], [14], [15]. This research project was conceived to take the first step towards setting up an FC-GT research lab within the Energy and Sustainable Design Group at University of Hertfordshire. Those first steps were the development of analytical models for the design and optimisation of concepts and operating strategies of such systems.

This chapter presents an introduction to the types of fuel cells studied and how they can be combined with gas turbines to form highly efficient power sources, followed by the aims and objectives of the project.

## *1.1 Types of fuel cells*

Fuel cells are electrochemical power sources that convert chemical energy stored in fuel to electric power through a redox reaction between the fuel and an oxygen carrier (typically air) as ion transfer between the fuel and the oxygen carrier creates an electric current [9], [16].

Based on the mechanism by which this energy conversion is achieved, and the materials used in the components, fuel cells can be classified into many types as shown in Table 1.1. They are:

- Proton Exchange Membrane Fuel Cells (PEMFC)
- Solid Oxide Fuel Cells (SOFC)
- Alkaline Fuel Cells (AFC)
- Phosphoric Acid Fuel Cells (PAFC)
- Direct Methanol Fuel Cells (DMFC)

**Table 1.1 Types of fuel cells [9], [16]**

| Fuel Cell type | Operating Temperature | System Efficiency | Fuels | Electrode catalyst | Electrolyte material |
|---|---|---|---|---|---|
| PEMFC | Around 80ºC | Up to 50% | $H_2$ | Pt | Nafion polymer membrane |
| SOFC | 550ºC to 1000ºC | Up to 65% | $H_2$, CO, $CH_4$, and $NH_3$ | Ni alloys | Zirconia, ceria |
| AFC | 20ºC to 70ºC | Up to 65% | $H_2$ | Pt or Ni | Alkaline solution |
| PAFC | Around 180ºC | Up to 40% | $H_2$ | Pt | Phosphoric acid |
| DAFC | 60ºC to 80ºC | Up to 25% | Methanol, ethanol | Pt and Ru | Nafion polymer |
| MCFC | 550ºC to 700ºC | Up to 55% | $H_2$, CO, $CH_4$, | Ni alloys | Molten carbonate |

The main advantage of fuel cells over conventional power sources such as combustion engines is the low to net-zero greenhouse gas (GHG) emissions. One of the most common fuels used in fuel cells is hydrogen, the oxidation of which only produces water vapour as a by-product. This has made fuel cells, especially PEMFCs and SOFCs, very popular alternative power sources in transport over the past few decades [17], [18], [19]. The main disadvantages of fuel cells are lower power density than heat engines, slow response to load changes, cost, low energy density of hydrogen storage, and lower technological maturity than conventional power sources. To tackle these disadvantages to some degree, fuel cells can be combined with other technologies and that is where SOFC-GT hybrid systems and turbocharged PEMFC systems come in.

The high operating temperature and exothermic nature of SOFCs makes them suitable for

combined cycles with other power sources as the heat dissipated from them can be used as a heat source to another power source where otherwise, an external source would be required. An example of such a system is an SOFC-GT Brayton cycle where the SOFC is introduced into a Brayton Cycle Gas Turbine between the compression and heat addition processes. This results in a hybrid system that combines the high efficiency of the SOFC and high power density of the gas turbine. SOFC efficiency is boosted by using pressurised air from the GT compressor, and the system can quickly respond to load changes as the GT has good load-following capabilities [10], [20]. A more detailed review of SOFCs, SOFC-GT systems, and how these systems can fit into transport is discussed in Chapter 2.1 of this report.

PEMFCs have lower operating temperatures than SOFCs but have much higher power densities. Due to the higher power density, PEMFCs have been the most popular choice for transport propulsive power out of all fuel cell types. Most PEMFC systems in transport nowadays use compressed air on the cathode side to increase power density even further. However, the power required to run the motor-driven compressor is drawn from the fuel cell which reduces system efficiency. The addition of a turbine to the system which is coupled to the compressor and expands gases from the fuel cell exhaust can recuperate some of the enthalpy in the exhaust stream and use it to assist the compressor motor. This can reduce the load on the compressor motor and hence improve system efficiency [9], [21], [22]. Chapter 2.2 of this report discusses PEMFCs and “turbocharged PEMFCs” in more detail.

**Table 1.2 Comparison of typical SOFC and PEMFC in numbers [9], [23]**

| | PEMFC | SOFC |
|---|---|---|
| Charge carrier | Hydrogen ion ($H^+$) | Oxygen ion ($O^{2-}$) |
| OCV at ambient conditions | 1.25 V | 1.18 V |
| Typical operating temperature | 60ºC to 80ºC | 500ºC to 1000ºC |
| Typical operating pressures | 1 bar to 3 bar | 1 bar to 6 bar |
| Electrical efficiency of turbomachinery-combined cycle | Up to 55% | Up to 65% |
| Cost/kW at 100,000 units p.a. | £50 to £70 | £100 to £120 |
| Typical gravimetric power density for stack | Up to 3.5 kW/kg | up to 0.75 kW/kg |
| Typical volumetric power density for stack | Up to 3.5 kW/litre | Up to 0.85 kW/litre |
| Compatible fuels | Hydrogen | Hydrogen, Carbon Monoxide, Methane |
| Temperature control | Excess air and external cooling | Excess air |

**Fuel cell voltage and current**

The maximum voltage developed across fuel cell unit, also known as Nernst potential, is given by Equation 1.1 [9].

**Equation 1.1**

$$E_{T,P} = \left(\frac{\Delta H}{nF} - \frac{T\Delta S}{nF}\right) + \frac{RT}{nF} ln \left(\frac{P_{H_2} P_{O_2}^{0.5}}{P_{H_2O}}\right)$$

Where,

$T$ is the fuel cell temperature,

$\Delta H$ is enthalpy of the electrochemical reaction,

$\Delta S$ is entropy of the electrochemical reaction,

$R$ is the universal gas constant,

$n$ is the number of electrons transferred per molecule of reactant,

$F$ is Faraday's constant,

$P_{H_2}$ is partial pressure of hydrogen at anode-electrolyte boundary,

$P_{O_2}$ is partial pressure of oxygen at the cathode-electrolyte boundary, and

$P_{H_2O}$ is partial pressure of water vapour in the anode-electrolyte boundary.

However, in practice, there are irreversibility losses to fuel cell voltage, and they are of three types:

- Activation loss: Losses due to energy spent in initiating and sustaining the electrochemical reaction at the electrode-electrolyte boundaries.
- Concentration loss: Losses due to the drop in concentration of reactants at the electrode-electrolyte interface resulting in lowering of the rate at which the electrochemical reaction occurs.
- Ohmic loss: Losses due to ohmic resistance in the electrolyte, electrodes, and interconnects.

Fuel cell current is a function of the rate at which hydrogen is oxidised in the cell. For a single cell, it is given by Equation1.2 [9].

**Equation 1.2**

$$I = \dot{n_{fuel}} \times n_{el} \times F$$

Where,

$\dot{n_{fuel}}$ is molar rate at which fuel is consumed,

$n_{el}$ is number of electrons participating in the redox reaction,

$F$ is Faraday's constant.

It was clear from existing knowledge that the two most promising types of such systems for

transport applications were SOFC-GT hybrid systems and Turbo-charged PEMFC systems due to their balance between efficiency and power density which is critical for transport. A 2016 study by NASA found that a power source for electric aircraft has to overcome the barrier of 60% electrical efficiency and 300 W/kg gravimetric power density to be adopted into aviation [6] and SOFC-GT and Turbocharged PEMFC systems are able to meet this. SOFC-GT systems are therefore feasible as turbofan/turbojet-integrated Auxiliary Power Units (APU) [15], [46], [47], in high altitude long endurance aircraft propulsion where range and fuel efficiency take importance over dynamic performance [48]–[50], and in road or rail transport cases where hydrocarbon fuels are the only option due to regional and infrastructural limitations [51]–[53]. PEMFC systems on the other hand, are more suited to being primary propulsive power sources in passenger cars, long-distance road transport, and small capacity passenger aircraft [54]–[58].

## *1.2 SOFC-GT systems and challenges*

### 1.2.1 SOFC principles

Solid Oxide Fuel Cells are solid-state electrochemical power sources that operate at temperatures above 550ºC and typically have an oxide-ion conducting electrolyte. The electrolyte is usually made of ceramic material and the high operating temperatures are required because oxide-ion conductivity of the material is a function of temperature and only conduct ions in the operating temperature range between 500ºC and 1000ºC depending on the material. Fuel is passed over the anode and oxygen over the cathode. Oxygen undergoes reduction at the cathode-electrolyte boundary, which releases $O^{2-}$ ions that migrate through the electrolyte to the anode. At the anode, the fuel – usually $H_2$ or CO – undergoes oxidation courtesy of the oxide ions that have migrated from the cathode. Therefore, oxygen is consumed at the cathode and the oxide of the fuel is produced at the anode with electricity as a by-product, along with heat courtesy of the electron and ion movement during the reaction [9], [23]. Figure 1.2 shows a schematic of a hydrogen fuelled SOFC cell working principle.

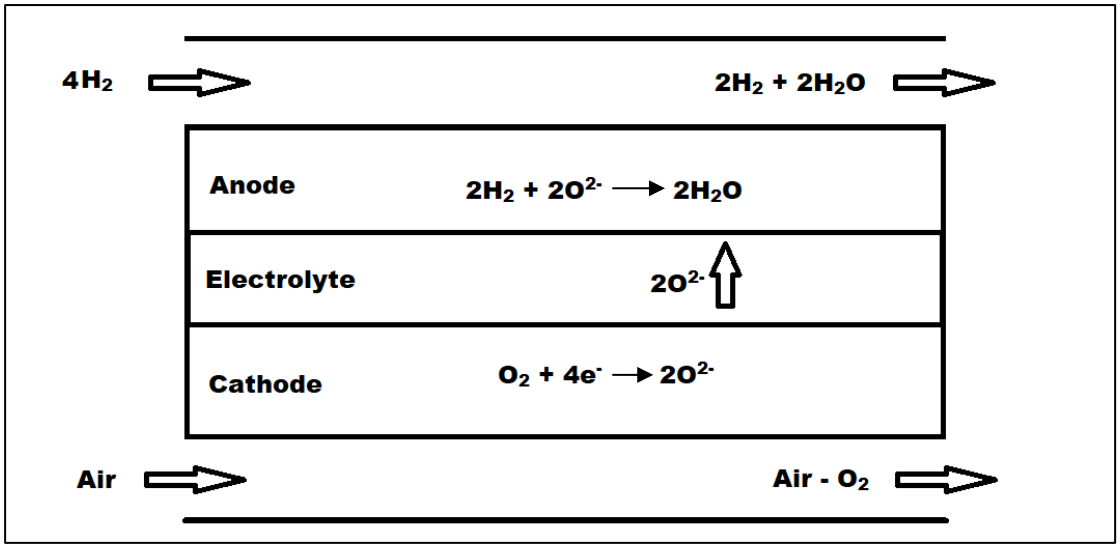


**Figure 1.1 Solid Oxide Fuel Cell working principle.**

### 1.2.2 SOFC-GT combined cycle

SOFC-GT hybrid systems can be broadly classified into two groups: pressurised systems and non-pressurised systems. In a pressurised system, the air passing through the fuel cell is pressurised by the compressor and then unused fuel from the fuel cell is burned and its energy recuperated by a turbine. In a non-pressurised system, the fuel cell operates with ambient air and heat transfer between the fuel cell and gas turbine combustor is the only interaction between GT and SOFC. Though non-pressurised systems are low-risk and simpler, pressurised systems are more efficient and most of the research in the SOFC-GT field has focused on them [24], [25]. Higher efficiencies are possible with pressurised systems because cell voltage increases with pressure. It also lowers energy consumed to achieve the a higher Turbine Inlet Temperature (TIT) as the heat dissipated from SOFC increases stream temperature to a value closer to a given TIT, reducing the heat needed from combustion [26]. Additionally, the exothermic nature of SOFCs means excess air over the stoichiometric fuel-to-air ratio is required to maintain temperature control. Gas turbines can improve the efficiency of excess air flow creation [27]. Therefore, given the dynamic loads, high efficiency, and high specific-power requirements of transport applications, pressurised SOFC-GT systems are considered more suitable for the field.

The other advantages of a pressurised SOFC-GT cycle are more efficient start-up and improved load-following for the SOFC. SOFCs require to be heated to temperatures above 550ºC to produce electricity which makes their start-up procedure inefficient as energy is spent on heating the stack but with little to no useful electric power output. However, in a SOFC-GT system, the excess heat from the gas turbine burner can be used during start-up [12].

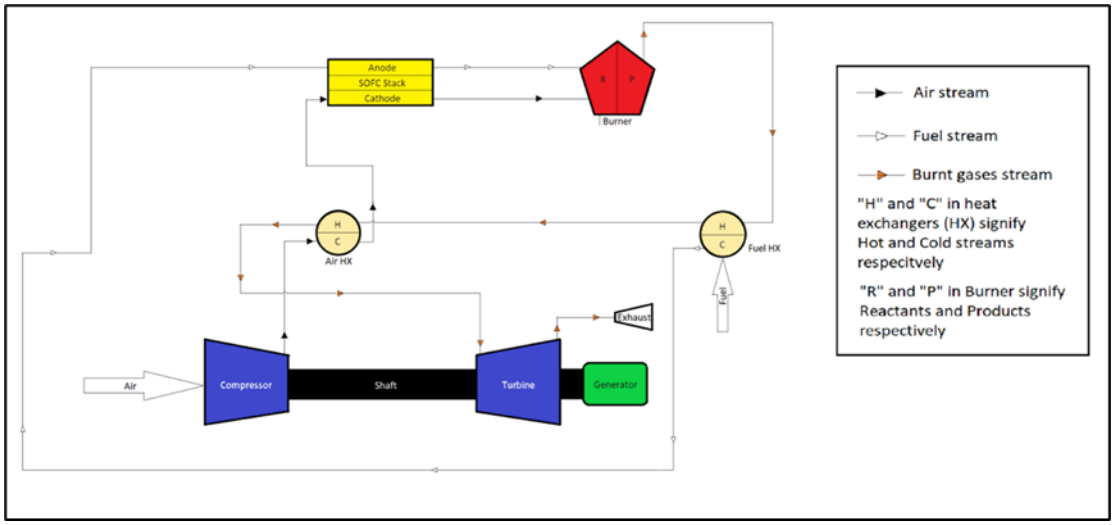


**Figure 1.2 Schematic diagram of a SOFC-GT system**

The simplest and lightest SOFC-GT configuration is where the fuel cell is placed between the compression process and the heat addition process in a Brayton Cycle. Going one step further, heat exchanger where the SOFC exhaust stream heat up the inlet stream can be added as shown in Figure 1.2. Air is pressurised by the compressor and then sent to the fuel cell cathode where it provides the oxygen for the electrochemical reaction. Unused fuel and air from the fuel cell along with fresh fuel are then reacted in the gas turbine burner and the hot tail gases from this process are expanded in the turbine. The turbine converts enthalpy in the tail gas mixture to mechanical power that drives the compressor and the generator, and the exhausted gases are released into the atmosphere. Tail gas from the burner is also used to pre-heat air and fuel streams going into the fuel cell via heat exchangers to maximise efficiency of the system.

### 1.2.3 Major challenges for SOFC-GT system development

**Thermal degradation of stack**

One of the main challenges for SOFCs is their operating temperature and the thermo-mechanical degradation and potential failure modes that come with it. The cause of this drawback is inherent to the SOFC working principle of charge transfer through mobility of oxide ions and electrolyte material properties.

Table 1.3 shows potential failure modes and degradation in SOFCs and how the high operating temperatures play a role in most of them.

**Table 1.3 Typical failure mechanisms of SOFC stacks [16], [28], [29], [30]**

| Failure mechanism | Causes | Potential solutions |
|---|---|---|
| Thermo-mechanical deformation | High operating temperature<br><br>Mismatch in coefficient of thermal expansion (CTE) between materials of cell components | Lowering operating temperature<br><br>Optimise material selection to minimise CTE mismatch |
| Reduced electron conductivity and diffusivity of electrodes due to poisoning by chromium and other impurities. | High temperatures lead to deposition of Cr from interconnects and impurities like sulphur from fuels. | Protective coatings and use of ceramic cathodes.<br><br>Use of high-purity fuels |
| Phase of electrode and electrolyte material leading to reduced electron and ion conductivity | Temperatures above 500ºC | Lowering operating temperatures.<br><br>Use of materials that are stable at high operating temperatures.<br><br>Layered manufacturing of PEN structure and addition of barrier layers |
| Changes in electrode microstructure leading to reduced diffusivity | High temperatures and impurities in the materials lead to coarsening of particles and reduced interstitial spaces | Lower operating temperatures.<br><br>Optimise particle distribution and purity of materials |

**System integration**

Another major challenge in SOFC-GT system development is the integration of the stack with the gas turbine and the rest of the system.

The heaviest component of a SOFC-GT system barring fuel storage is the fuel cell itself. Therefore, to maximise specific power of the whole system, power density of the fuel cells should be maximised, and weight of the stack should be minimised [31].

Power density of an SOFC is usually expressed specific to active area of each cell, i.e., power/area ($W/cm^2$). To maximise power density and efficiency, polarisation losses to cell

voltage caused to ohmic resistance, concentration deficit of reacting species, and activation overpotential of electrolyte reaction should be minimised. Polarisation leads to decrease in cell voltage and energy loss in the form of heat. Theoretically, these losses can be reduced by increasing the ionic conductivity of electrolyte and gaseous diffusivity of electrodes [6]. In practice, availability of materials with the required properties and lack of manufacturing processes to achieve the required dimensions and diffusivity are major challenges [32].

Therefore, optimisation of operating parameters like pressure and temperature are used to boost power density and efficiency of the system. SOFC temperature determines the Turbine Inlet Temperature (TIT) in a hybrid system which has a significant impact on gas turbine and consequently system performance. If TIT values wander outside the operating range of the turbine, the system will go into stall or surge and fail, therefore, robust control strategies that incorporate temperature sensors and valves for controlling temperatures by varying excess air ratios is required [11]. Furthermore, achieving high power densities at lower stack temperatures is important as high temperatures give rise to challenges in stack design and integration with gas turbines.

## *1.3 Turbocharged PEMFC systems*

Proton exchange membrane fuel cells (PEMFC) have been the most popular choice of fuel cells in transport propulsion due to the high gravimetric power density compared to other types of fuel cells. In this section, a brief overview of PEMFC principles and turbocharged PEMFC systems is given.

### 1.3.1 PEMFC principles

A Proton Exchange Membrane Fuel Cell (PEMFC) uses a perfluoro-sulphonic acid (PFSA) polymer membrane as the electrolyte. This membrane becomes conductive to protons (or $H^+$ ions) when humidified and facilitate electrochemical oxidation of hydrogen as shown in Figure 1.3. Hydrogen is passed over the anode and humidified air over the cathode. $H_2$ undergoes oxidation at the anode-electrolyte boundary, which releases $H^+$ ions that migrate through the electrolyte to the cathode. At the cathode, the $O_2$ in air undergoes reduction courtesy of the $H^+$ ions that have migrated from the anode. Therefore, hydrogen is consumed at the anode and $H_2O$ is produced at the cathode with electricity and heat as by-products [9], [16].

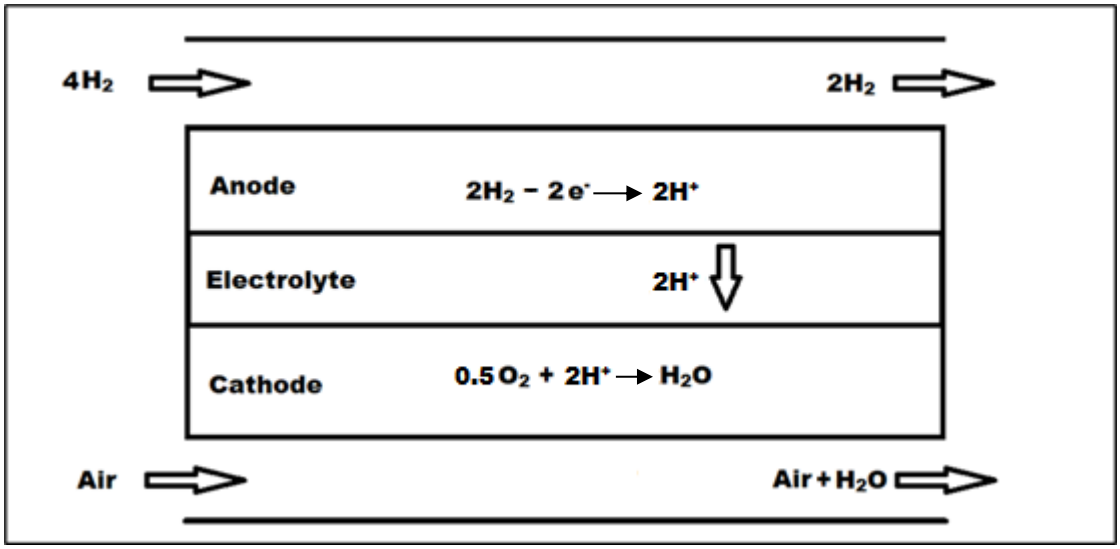


**Figure 1.3 PEM Fuel cell working principle**

## 1.3.2 Challenges for PEMFC systems

**Humidification and cooling**

The PFSA electrolyte conducts electrons through the sulphonic acid (-$SO_3$) group in the side chain of its polymer structure. When hydrated, some molecules of the electrolyte attract $H^+$ ions from $H_2O$ as shown in Figure 1.4.

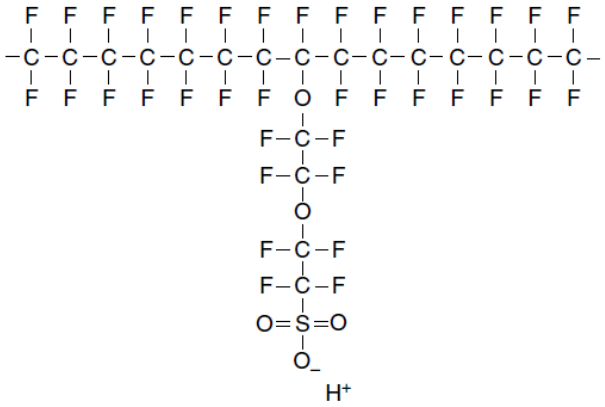

**Figure 1.4 Chemical structure of a perfluoro-sulphonic PFSA polymer [9]**

Because of the presence of $SO_3^-$ and $H^+$ ions, positive and negative ions from each molecule are strongly attracted to each other, causing sidechains to cluster together within the material's structure. Sulfonic acid is highly hydrophilic and attracts water, resulting in the creation of hydrophilic regions within an otherwise hydrophobic PTFE substance. In these hydrated regions, $H^+$ ions are weakly attracted to $SO_3^-$ groups, resulting in the creation of a dilute acid. This creates different microdomains in the macromolecular structure, including dilute acid regions where $H^+$ ions are attached to water molecules to form hydronium ions ($H_3O^+$), within a

strong and resilient hydrophobic structure. $H^+$ ions move by "hopping" from one water cluster to another, aided by the weak hydrogen bonds that must be formed and broken with each ion movement [9].

Therefore, PEMFC stacks require the proper amount of water for the membrane to function correctly. However, too much or too little water can cause problems. Inadequate humidification can cause the membrane to dry out and crack, while excessive humidification can flood the cells and reduce performance. At shutdown, the stack needs to be dehumidified or residual water in the electrolyte and electrodes can freeze and damage them. The PEM fuel cell electrochemical reaction is exothermic and therefore, stacks also require external cooling with precise temperature control to prevent condensation and ensure optimal performance. If the temperature is too low, water can condense and accumulate in the system, leading to corrosion and reduced efficiency. On the other hand, if the temperature is too high, the $H_2O$ evaporates, leading to insufficient hydration of the membrane. This causes parasitic losses in system as power for the cooling system is taken from the fuel cell electrical output [33].

**Pressurisation**

Open circuit voltage of a PEMFC is directly proportional to the square root of the partial pressure of oxygen at the cathode. Therefore, pressurisation of the air stream (cathode stream) boosts efficiency and power density of the stack. However, pressurisation of air in PEMFC systems generally use a compressor driven by a motor that is powered by the fuel cell itself. This results in parasitic losses that reduce the efficiency of the system, reducing the efficiency gains from pressurisation. This is demonstrated by the following analysis done by Dicks and Rand [9].

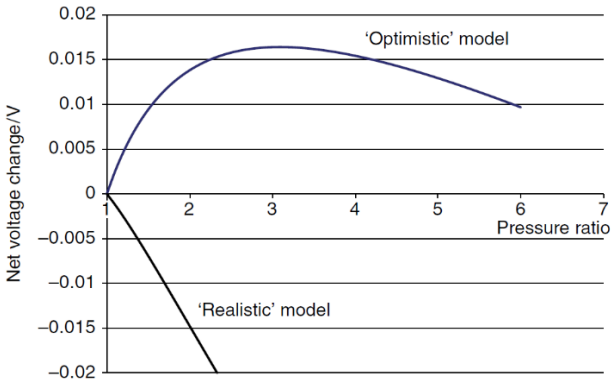


**Figure 1.5 Results of pressurisation study by Dicks and Rand [9]**

An “optimistic” and a “realistic” analysis with the parameters shown in Table 1.4 and results in Figure 1.5 shows that for the optimistic model, there is a net gain of about 17 mV per cell when the pressure is boosted by a ratio of about 3, but the gain diminishes at higher pressures. For the more ‘realistic’ model, however, there is always a net loss because of the higher pressure because the power gained is always exceeded by the power needed to drive the compressor.

This shows that pressurisation with a motor-driven compressor is only beneficial with highly efficient compression.

**Table 1.4 Parameters used in pressurisation study [9]**

| Parameter | Optimistic model | Realistic model |
|---|---|---|
| Voltage gain constant per unit (atm) pressure | 0.10 V | 0.06 V |
| Inlet gas temperature | 15ºC | 15ºC |
| Mechanical efficiency of electric compressor | 0.95 | 0.90 |
| Isentropic efficiency of compressor | 0.75 | 0.70 |
| Excess air ratio | 1.75 | 2.0 |

### 1.3.3 Turbocharged PEMFC

A turbocharged PEMFC (T-PEMFC) system is a pressurised PEMFC system where the compressor motor is assisted by a turbine that is driven by fuel cell off-gas.

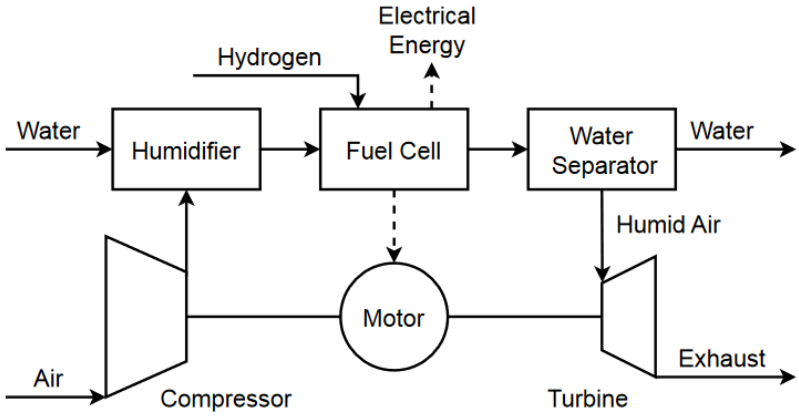


**Figure 1.6 Schematic of a Turbocharged PEMFC system [34]**

A schematic of such a system is shown in Figure 1.6. and depicts the following components:
Compressor: Ambient air is drawn into the system through a compressor, where it is pressurised before entering the humidifier. The compressor serves to increase the partial pressure of oxygen in the air supply, enhancing the efficiency of the electrochemical reaction within the fuel cell.

Humidifier: The compressed air passes through a humidifier, where it is mixed with water vapor. The humidification of the air is essential to maintain the hydration of the PEMFC membrane, thereby ensuring its ionic conductivity and preventing membrane dry-out.

Fuel Cell: Within the fuel cell, hydrogen is supplied to the anode side, while the humidified air is supplied to the cathode. At the anode, hydrogen molecules are dissociated into protons and electrons. The protons migrate through the proton exchange membrane to the cathode, while the electrons are directed through an external circuit, generating electrical energy. At the cathode, the protons, electrons, and oxygen from the air combine to produce electricity and water.

Water Separator: The byproduct of the electrochemical reaction, water, is separated from the humid air stream. The separator ensures that excess water is removed from the system, preventing flooding of the fuel cell which could otherwise impede the reaction.

Turbine: The humid air, now depleted of oxygen, exits the fuel cell and expands through a turbine. The turbine recovers energy from the air stream, which can be used to drive the compressor, thus improving the overall efficiency of the system.

Motor: The motor is mechanically connected to the compressor and turbine. It converts part of the electrical energy generated by the fuel cell to mechanical energy to drive the compressor, thus forming a closed loop that enhances the system's efficiency.

Exhaust: The air stream, having passed through the turbine, is expelled from the system as exhaust.

Turbocharging enhances the performance of Proton Exchange Membrane Fuel Cells (PEMFC) by increasing the power density through pressurisation. However, this is achieved with lower parasitic electric demand from the compressor motor with the presence of a turbine that recuperates some of the heat transferred from the fuel cell to the air stream, allowing for a reduction in the size of the fuel cell stack, yielding a system that is not only more compact and lighter—advantageous for mobile and portable applications—but also more cost-effective. This downsizing of the fuel cell stack inherently decreases the system's overall cost, enhancing its affordability and widening its application scope. Additionally, turbocharging improves the system's response time to transient loads by assisting the compressor motor and ensuring a swifter supply of air to the fuel cell, a critical feature in scenarios demanding rapid fluctuations in power output [35].

## *1.4 Analytical Modelling of Fuel Cells*

The development of mathematical models for fuel cell systems is guided by various classification criteria, leading to a array of models tailored to specific analytical needs. The choice of a model is influenced by the desired balance between accuracy, computational

demands, and data availability.

Models can be categorised based on their treatment of time into steady-state and dynamic models. Steady-state models, which disregard time variability, simulate fuel cell performance under unchanging conditions through algebraic equations that encapsulate the thermodynamic, fluidic, and electrochemical processes inherent to fuel cell operation. Conversely, dynamic models incorporate time-dependence through differential equations, offering a more nuanced simulation of transient behaviours, thereby aligning more closely with real-world conditions where operational states are seldom constant [15].

Spatial considerations further differentiate models into 0D, 1D, 2D, and 3D categories, with each providing varying levels of detail about the spatial distribution of physical phenomena within the system. Zero-dimensional (0D) models abstract away spatial details, focusing on system outputs given specific inputs and boundary conditions. One-dimensional (1D) models offer insights into the variation of physical properties along a single dimension, beneficial for examining processes along the direction of gas flow or diffusion in fuel cells. Two-dimensional (2D) models extend this analysis across two dimensions, frequently employed in the design of channels and manifolds through computational fluid dynamics (CFD). Three-dimensional (3D) models offer the most comprehensive spatial representation, combining the capabilities of 1D and 2D models to simulate the full geometry of fuel cells, albeit at a higher computational cost [13], [36].

Furthermore, models are classified based on their foundational principles into first-principles (or physics-based), empirical, or semi-empirical. First-principles models employ theoretical equations to simulate physical phenomena, adaptable across different system configurations but potentially limited in their capacity to capture complex behaviours without significant complication. Empirical and semi-empirical models, derived from experimental data, offer practical insights into system behaviour with reduced computational demands, athough their applicability is constrained by the breadth and detail of their data sources [37].

### 1.4.1 The case for First-Principles 0D Modelling in Fuel Cell Systems Engineering

First-principles 0D models of fuel cell systems are constructed on the fundamentals of mass, energy, and charge conservation laws, alongside thermodynamic and electrochemical principles, to predict system-level performance indicators like efficiency and power output. This modelling strategy is lauded for its computational efficiency and its ability to offer insights without delving into the intricacies of spatial process variations. Highlighted in the literature, these models have been pivotal in advancing fuel cell technology by guiding the design and

optimisation of more efficient systems [14].

Advantages of 0D modelling include computational efficiency and the facilitation of rapid prototyping and system-level insights, which are crucial during the initial stages of design and optimisation. However, its inherent simplifications may limit accuracy in systems characterised by complex spatial dynamics. Recent advancements aim to refine the accuracy of 0D models through the integration of more detailed physical principles, transient behaviours, and multi-scale simulations. Moreover, the incorporation of data-driven and machine learning sub-models into first principles models promises to augment their predictive capabilities [38], [39].

In systems engineering, analytical models are essential for understanding, designing, and optimising complex systems. These models, by putting the focus on system essentials, enable the analysis of system behaviour, performance evaluation under various scenarios, and informed decision-making. Their utility is grounded not in absolute accuracy but in their ability to meaningfully represent the impact of different parameters on system-level outcomes, as supported by the scientific literature and the principles of model-based systems engineering (MBSE) and satisficing. This underscores the value of analytical models in effectively guiding the engineering process through a balance between simplicity and predictive accuracy [40].

## *1.5 Aims and objectives*

The knowledge contribution of this study is centred around design and development of mathematical models of fuel cell-gas turbine systems that can be used in sizing and feasibility studies. The models developed on this project are to be used in design, development, and optimisation of fuel cell systems to enable setting up of FC-GT research laboratories.

### 1.5.1 Aims of the project

**1) Enable future research and development of FC-GT:** The primary aim of this project is to enable the setting up and running of FC-GT prototype rigs in a university laboratory with no existing experimental data or equipment. This presents itself with a list of requirements and challenges.

Requirements:

- The work should generate data regarding component sizing, optimal system configurations, and the resource requirements for purchasing and assembling FC-GT system rigs that stay within the dimensional and operational constraints of the laboratory.

Challenges:

- There was no in-house data or previous work that can feed into this project.

**2) Development of analytical system models:** As described in Aim 1, this project is aimed at the initial stages of development of the FC-GT “product”. This phase corresponds to the left side of the “System V” of system development shown in Figure 1.7. In model-based systems engineering, this phase is served by 0D and 1D analytical models. These models are used for analytical system design to define concepts that meet a set of performance targets for the product.

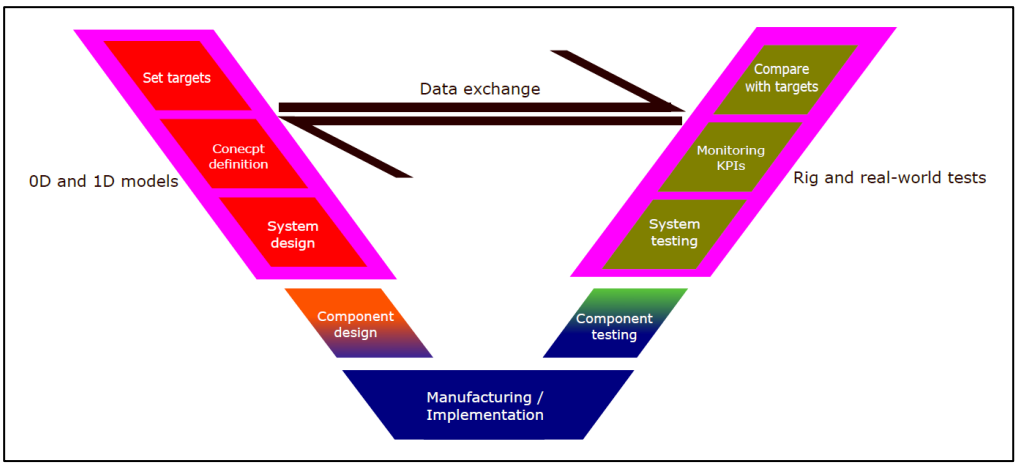


**Figure 1.7 System V of product development**

In the context of systems engineering and product development, System V is a model that describes a structured process for the development and lifecycle management of systems. The "V" in System V refers to the shape of the model, which resembles the letter "V" and represents the sequence of steps involved in the development and subsequent testing of systems. This model is particularly useful in complex systems such as FC-GT power sources that require rigorous testing and validation to meet specified requirements.

To set about working towards this aim, the requirements and challenges relevant to it are listed below:

Requirements:

- The models should be able to work without empirical or test data as such data are not available.
- The models must be flexible and adaptable to study the effects of varying designs and configurations of the FC-GT systems.
- Since the users of the models in the future will be from varying backgrounds of electrical, chemical, and mechanical engineering and science, the models should be implemented in such a way that they do not require specialised programming or modelling skills.

Challenges:

- Fuel cells are complex devices whose working principles involve electrochemical, thermodynamic, and fluid dynamics phenomena interlinked with each other. Modelling this behaviour accurately requires higher computational effort than more conventional power systems due to the higher number of governing equations that represent those

phenomena.

- Following on from the previous point, simplified equations must be used to model fuel cell behaviour in the analytical models to reduce computational effort. However, this comes at a penalty to accuracy and the main challenge is finding the right compromise.

**3) Identify most significant system design and operating parameters:** The third aim of this project is to deploy the right models and demonstrate their abilities in system parameterisation, sizing, and analysis of FC-GT hybrid systems. Through this, the project aims to contribute to FC-GT research in the following ways:

- System Integration: FC-GT hybrid systems combine the advantages of fuel cells and gas turbines. Identifying significant parameters is crucial for integrating these technologies in a way that maximises their complementary characteristics.
- Efficiency Improvement: By focusing on the most impactful parameters, the project can significantly improve the system's overall efficiency. This includes optimising fuel usage and minimising energy losses, which is critical for the economic and environmental aspects of the system.
- Reliability and Durability: Identifying and controlling key parameters can lead to improvements in system reliability and longevity. This is particularly important for FC-GT systems, where operational conditions can greatly affect component lifespan and system uptime.
- Cost Reduction: Through the careful analysis and optimisation of critical design and operating parameters, it's possible to reduce capital and operational costs. This makes the FC-GT hybrid system more economically viable and competitive in the market.
- Knowledge Base Expansion: The process of identifying these parameters contributes to the broader knowledge base surrounding hybrid systems, helping to guide future projects and research in this area.

**4) Quantify improvements in performance over conventional and other alternative power sources:** The final aim of this project is to quantify the environmental impact of FC-GT power sources on transport applications when compared to conventional and existing power sources. This aim is important for several compelling reasons, each contributing to demonstrating the value and advancement these hybrid systems bring to the sector:

- Comparative Analysis: By quantifying performance improvements, one provide a clear, analytical basis for comparing FC-GT hybrid systems against conventional power sources such as standalone gas turbines, and existing fuel cell power sources. This helps in illustrating the specific advantages in efficiency, and load following.
- Investment Justification: Quantitative data on performance improvements is essential for justifying the investment in FC-GT technology. It demonstrates to stakeholders, including research bodies and other funding sources the research potential, helping to attract more funding to the laboratory.

- Higher Efficiency Levels: FC-GT systems are known for their high efficiency in converting fuel to electricity, especially when waste heat from the gas turbine is used to improve the fuel cell's performance. Quantifying these efficiency gains highlights the potential for significant fuel savings and lower operating costs compared to conventional systems.
- Load Flexibility: Demonstrating how FC-GT systems can efficiently manage varying load demands better than fuel cell-only sources, possibly comparably to conventional sources, can further justify their adoption, especially in applications with fluctuating power needs.
- Reduced Emissions: One of the critical advantages of FC-GT hybrid systems is their potential to significantly reduce greenhouse gas emissions and pollutants. Quantifying the reduction in $CO_2$, $NO_x$, other emissions, and overall energy consumption compared to gas turbines and conventional pressurised PEMFC power sources underscores the environmental benefits and supports the case for cleaner energy solutions.

### 1.5.2 Objectives

To achieve the aims listed in Chapter 1.5.1; the following objectives were set out for the project:

1) **Literature Review on FC-GT Systems in Transport Applications:** Conduct a comprehensive review of existing literature on Fuel Cell-Gas Turbine (FC-GT) power sources within transport applications. This review will focus on identifying optimal configurations and applications for Solid Oxide Fuel Cell-Gas Turbine (SOFC-GT) and Turbocharged Proton Exchange Membrane Fuel Cell (PEMFC) systems. Additionally, it aims to pinpoint appropriate analytical modelling frameworks that have been previously applied in this field. The objective is to lay a foundational understanding that guides the development of new analytical models for FC-GT systems, ensuring they are aligned with current technological and operational benchmarks.

2) **Development of Analytical Modelling Methodologies:** Develop robust modelling methodologies for the analytical design and engineering of FC-GT systems. This objective entails the creation of a structured approach that facilitates the conceptual and preliminary design phases of FC-GT systems. The methodologies will be developed within the framework identified from the literature review, focusing on zero-dimensional (0D) and one-dimensional (1D) analytical models. These models should support the exploration of system configurations and performance under various operational conditions.

3) **Implementation of Accessible Models:** Implement the developed analytical models in a user-friendly manner, ensuring they are accessible to engineers and scientists

with fundamental knowledge of fuel cells and gas turbines. The objective is to provide a tool that does not require specialised programming or advanced mathematical modelling skills, thereby broadening the usability of the models across interdisciplinary teams. The implementation will prioritise flexibility, adaptability, and ease of use to facilitate widespread application in the research and development of FC-GT systems.

4) **Validation of Analytical Models:** Validate the analytical models against established datasets or higher-order models that have been previously validated. This objective aims to ensure the accuracy and reliability of the developed models by comparing their outputs with empirical data or results from more complex models. Validation is a critical step in confirming that the models can accurately represent the behaviour of FC-GT systems under various conditions.

5) **Deployment in Design Studies:** Deploy the validated models in example design studies to demonstrate their capabilities in system parameterisation, sizing, and performance analysis. This objective involves using the models to explore different FC-GT system designs, assessing how variations in design parameters impact system performance. The design studies will highlight the models' utility in practical engineering applications and their potential to inform decision-making in the development of FC-GT systems.

6) **Virtual Testing for Performance Analysis:** Utilise the models to perform virtual testing of FC-GT systems, examining the effects of system design parameters on overall performance. This objective seeks to simulate real-world operational scenarios to evaluate system efficiency, reliability, and environmental impact. Virtual testing enables the exploration of design optimisations and operational strategies that enhance the performance of FC-GT systems, contributing valuable insights to the field of fuel cell and gas turbine hybrid technologies.

Table 1.5 lists the following chapter of this thesis against the objectives that are covered in them.

**Table 1.5 Thesis chapters and corresponding objectives**

| Chapter No. | Chapter title | Objectives covered |
|---|---|---|
| 2 | Review of model-based FC-GT studies | Objective 1 |
| 3 | Methodology | Objectives 2 and 3 |
| 4 | SOFC-GT Steady State Modelling | Objectives 4 and 5 |
| 5 | SOFC-GT Dynamic Modelling | Objectives 4 and 6 |
| 6 | Simulation of PEMFC system | Objective 6 |

# 2 Review of FC-GT system studies

## *2.1 SOFC-GT systems for transport applications*

This section provides a review of literature on SOFC-GT system studies that provide insights on the configurations and modelling methodologies. The sub-sections present progress made at various levels and components of the hybrid system namely the solid oxide fuel cell, SOFC-GT configurations, and hydrogen storage.

Overall, 0D models for SOFCs have been developed to account for various factors affecting cell performance, including temperature, pressure, gas composition, current density, fuel utilisation, and cell geometry. These models provide valuable insights into the behaviour of SOFCs and can be used to optimise their design and operation.

### 2.1.2 Solid Oxide Fuel Cells

**Stack performance**

The most important goal of a good SOFC design in aircraft application is to maximise specific power and efficiency. Borer [41] studied various electrified propulsion concepts for aircraft and found that a SOFC-GT system should have at least 300 W/kg specific power and 60% overall efficiency to be adopted to aviation. The heaviest component of a SOFC-GT system barring fuel storage is the fuel cell itself. Therefore, to maximise specific power of the whole system, power density of the fuel cells should be maximised, and weight of the stack should be minimised.

Power density of an SOFC is usually expressed specific to active area of each cell, i.e., power/area ($W/cm^2$). To maximise power density and efficiency, polarisation opposite to cell voltage caused to ohmic resistance, concentration deficit of reacting species, and activation overpotential of electrolyte reaction should be minimised. Polarisation leads to decrease in cell voltage and energy loss in the form of heat. Theoretically, these losses can be reduced by reducing thickness of the electrolyte and electrodes, increasing ion and electron conductivity of electrodes and electrolyte, and increasing diffusivity of electrodes [42]. In practice, availability of materials with the required properties and lack of manufacturing processes to achieve the required thinness are major challenges. For a cell with Ni-YSZ anode support, power density was found to improve drastically by reducing the thickness of $Gd_2O_3$-doped $CeO_2$(GDC)/YSZ electrolyte and infiltrating the Lanthanum Strontium Cobalt Ferrite (LSCF)-GDC cathode with oxides of praseodymium ($PrO_x$). The experimental study, which used typecasting for anode manufacturing and sintering at lower temperatures for cathode, found power density to increase from 0.4 $W/cm^2$ to 0.95 $W/cm^2$ at 650°C and from 1.4 $W/cm^2$ to 2.38 $W/cm^2$ at 800°C through

$PrO_x$ infiltration and reducing electrolyte thickness from 8 µm to 2.5 µm [32].

Achieving high power densities at lower temperatures is important as high temperatures give rise to challenges in stack design and integration with gas turbines. The most significant cause of degradation in SOFC is high temperatures combined with uneven thermal gradients which lead to buckling of interconnects and contact separation between the various layers of the cell due to the difference in thermal expansion coefficient of the materials. The elastic modulus and yield strength of cell materials are lowered at high temperatures, and this can be detrimental to the stack especially when the support electrode material is affected. SOFC temperature also determines the Turbine Inlet Temperature (TIT) in a hybrid system which has a significant impact on gas turbine and consequently system performance. If TIT values wander outside the operating range of the turbine, the system will go into stall or surge and fail.

Optimum material choices and temperature gradient control strategies are, therefore, very important aspects of the cell design. For example, a cell with anode made of NiO-YSZ has been experimentally proven to suffer the least microstructural changes from thermal loading that cause weakening of the cell support than one with a Ni-YSZ anode [43].

System control should incorporate temperature sensors for the SOFC channels, interconnects, and PEN (positive-electrolyte-negative) structure. To control temperature gradients under transient operating conditions, a high order sliding observer that measures internal SOFC temperature along with compound controller for feedback and feedforward was conceptualised by Wu et al [44]. Temperature control is realised by controlling flow composition and conditions in the air and fuel channels of the SOFC stack so, the channel configuration and manifold designs should ensure even distribution of reacting species in both fuel and air streams across the cell [45]. Under transient conditions, the polarisation curve (V-I characteristic) and flow conditions for each corresponding point on the polarisation curve of the cell varies from that at steady state and these changes should be accounted for by the control system [46]. The alteration of flow conditions to keep species concentrations and temperatures at desired levels can be realised through compressor-turbine shaft speed control, valve control and the use of bypass and recirculated flows albeit through a complicated control system.

The main requirements for the modelling work identified from the literature review are as follows:

- The model should capture the effects of PEN structure material and dimensions on the electrochemical performance of the SOFC stack. This supports the decision to go for a physics-based approach rather than a data-driven modelling approach.
- The transient model of the SOFC stack must predict the effects of operating conditions on stack temperature and stream temperatures separately. This is because stack temperature is controlled by varying stream temperatures and flowrates so the PEN

structure and streams have to be modelled as separate domains to model heat transfer between them.

**Tubular and Planar SOFCs**

SOFCs can be classified into tubular and planar based on the arrangement of PEN structure, channels, and interconnects. Figure 2.1 [9], [24] shows diagram of the two designs.

As part of this project, a comparative analysis of tubular and planar configurations of Solid Oxide Fuel Cells (SOFC) was performed based on several performance and manufacturing properties that are important for transport applications. Each property was assigned a weightage, indicating its relative importance in the context of transport applications. The Tubular and Planar SOFC designs were then rated on a scale of 1 to 5 based on how good the properties of interest are for each design. The results of this comparative study are presented in Table 2.1.

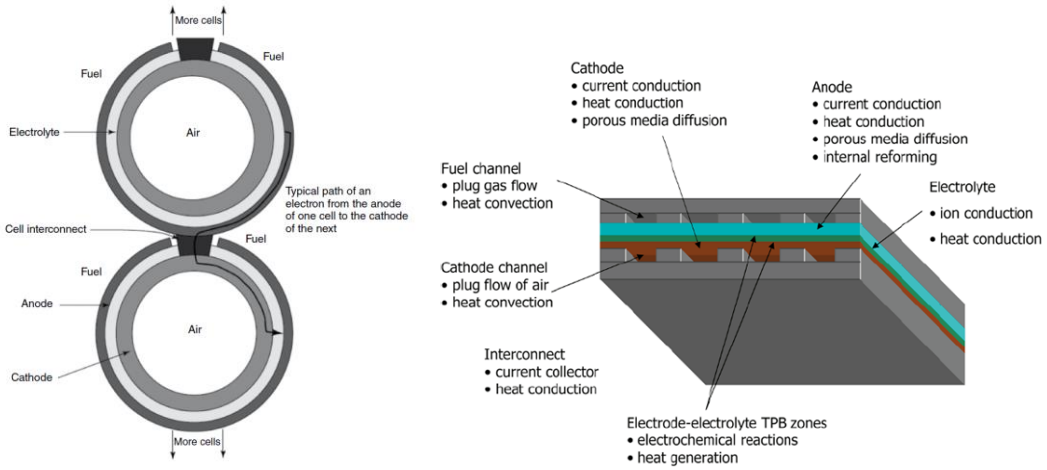


**Figure 2.1 Diagrams of Tubular (left) and Planar (right) SOFC [9], [24]**

**Table 2.1 Comparison matrix of tubular and planar SOFC for transport applications**

| Property | Weightage | Rating (higher is better) | |
|---|---|---|---|
| | | Tubular | Planar |
| Area-specific resistance | 3 | 3 | 5 |
| Cost of manufacturing | 2 | 5 | 3 |
| Volumetric power density | 3 | 2 | 4 |
| Gravimetric power density | 5 | 2 | 5 |
| Resistance to thermo-mechanical degradation | 4 | 3 | 4 |
| Total | | 47 | 74 |

Area-specific resistance, which affects the internal losses and efficiency of the fuel cell, holds a weightage of 3, reflecting its significant impact on performance. Both tubular and planar

SOFCs score differently, with planar SOFCs having a higher score 5 compared to tubular ones 3, suggesting that planar SOFCs have lower area-specific resistance.
The cost of manufacturing, weighted at 2, is more favourable for tubular SOFCs, as indicated by a higher score of 5 compared to 3 for planar SOFCs. This implies that tubular SOFCs are generally less expensive to manufacture.

Volumetric power density, with a weightage of 3, is rated higher for planar SOFCs 4 than for tubular SOFCs 2, suggesting that planar SOFCs are more compact for the same power output.

Gravimetric power density, deemed most critical with the highest weightage of 5, indicates the power output per unit weight of the fuel cell. Both tubular and planar SOFCs are rated equally (score of 5), suggesting similar performance in terms of weight efficiency.

Resistance to thermo-mechanical degradation, with a weightage of 4, is essential for the longevity and durability of the SOFCs. Tubular SOFCs scored 3, while planar SOFCs scored 4, indicating a slightly better resistance for the planar configuration.

The total scores for each SOFC type – 47 for tubular and 74 for planar – summarise the overall comparison. A higher total score for the planar SOFC suggests that, according to the weightage and ratings given, it is more suitable for transport applications based on the properties considered in this matrix.

### 2.1.3 Hybrid configurations

The aim of hybridising SOFCs with gas turbines is to have a system that has a combination of dynamic performance, specific power, efficiency and GHG emissions that is most desirable for a given application. For example, SOFC degradation under high loads and transient operation can be mitigated by hybridisation with gas-turbine in such a way that load changes are taken care of by the gas turbine while the fuel cell is maintained at steady operating conditions. On the other hand, the efficiency of a gas turbine cycle can be improved by replacing or supplementing combustion with heat addition by SOFC in the working cycle.

For aircraft application, the most important considerations while deciding on the configuration of the hybrid system are maximising specific power and efficiency to achieve the respective 300 W/kg and 60% targets [41]. Keeping this in mind, this section of the paper looks at various SOFC-GT configurations explored previously across various applications and aims to identify the most appropriate one for aircraft.

**SOFC integrated turbojet or turbofan**

In this configuration, a SOFC is integrated with a turbojet or turbofan engine cycle such that the

fuel cell acts as an electric power-producing burner in addition to the combustor. In such a set-up, the fuel cell provides power for on-board systems, removing or reducing the need for an Auxiliary Power Unit (APU).

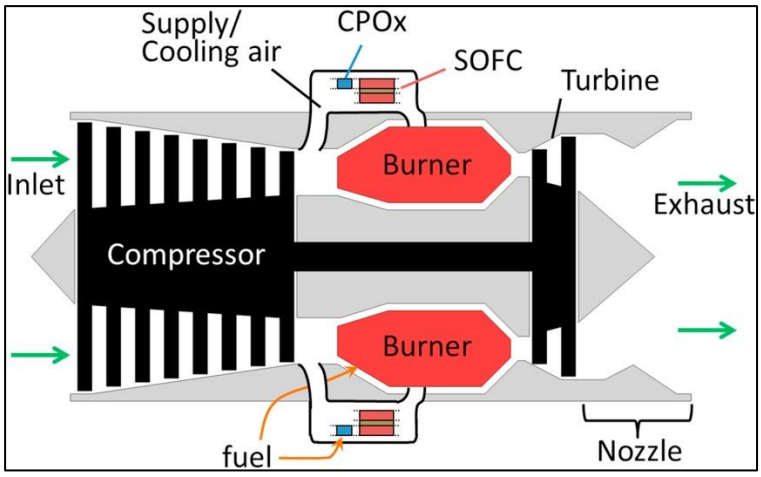


**Figure 2.2 SOFC integrated turbojet engine [47]**

Waters and Cadou [48] analytically studied such a concept with on-board reformer fuelled by jet fuel for three types of UAV engines: a turbojet, a low bypass turbofan, and a high-bypass turbofan. A simplified schematic of the concept is shown in Figure 2.2. Their results showed that such a system could provide fuel savings (up to 5% for the studied cases) and was capable of higher outputs of electric power (more than 500%) for on-board systems than a conventional gas turbine engine which drives a generator to power on-board electrics. However, a 13% decrease in specific power of the engine was observed even though efficiency was found to increase by 8% for the high-bypass turbofan. Ji et al [49] studied a similar turbojet engine concept but with an interstage burner separate from the combustor for SOFC exhaust gases between the high pressure and low-pressure stages of the turbine. This system was shown to gain up to 2.94% thermal efficiency and up to 24.07% specific thrust but with up to 8% lower specific impulse depending on the operating conditions and electric power fraction (which could be increased by up to 10 times).

However, both studies above did not account for the increase in drag and weight due to the engines becoming bigger by fuel cell addition. The gain in efficiency is not substantial enough to reach target values in either system as well. Something that future research and optimisation of this type of configuration can focus on is adopting hydrogen fuel which does away with the need for a reformer, making the engine smaller and lighter.

**SOFC-turbogenerator with electric propellers**

SOFC-turbogenerator is the most widely studied configuration of SOFC-GT systems. In fact, these systems were first developed for stationary power generation and combined heat and power applications and then considered for mobile applications with the rise of microturbines and progress in SOFC technology. The schematic of a typical SOFC-turbogenerator system is

shown in Figure 2.3.

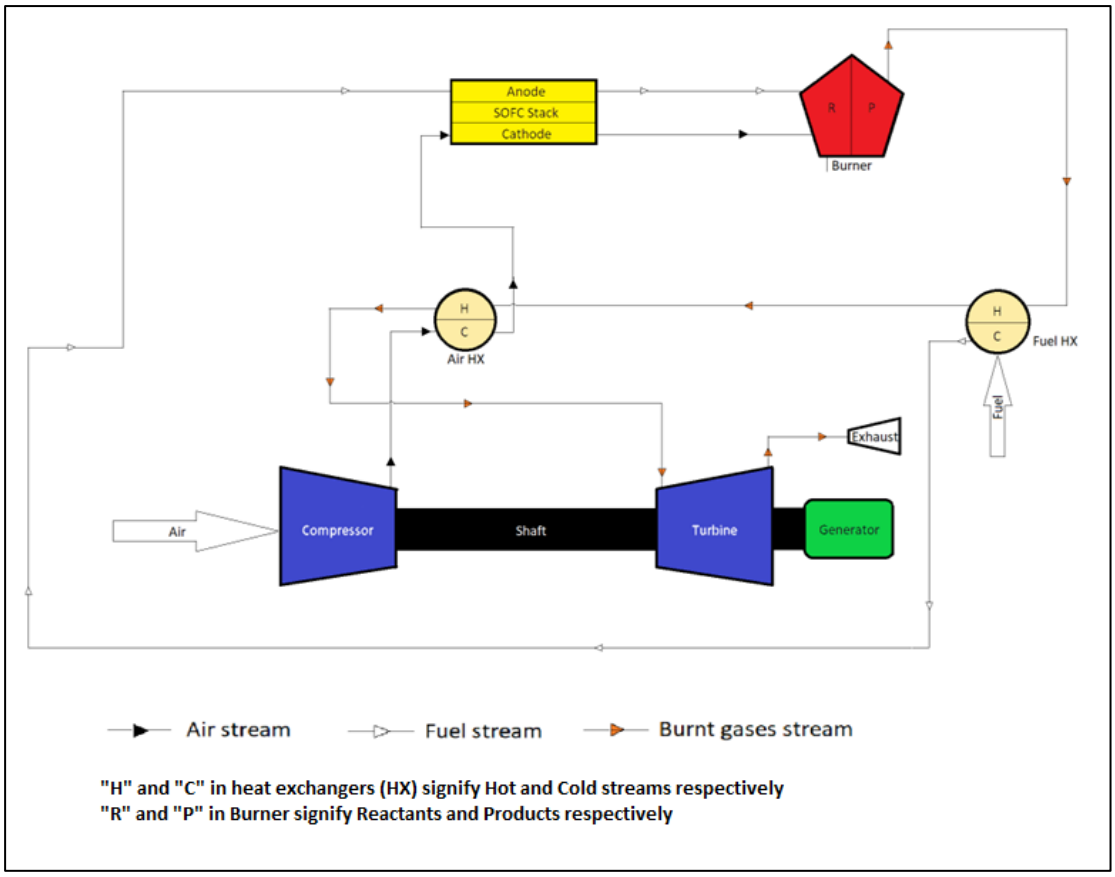


**Figure 2.3. Schematic of a typical SOFC-turbogenerator hybrid system**

The most basic configuration studied in Choudhary et al [50] exhibits 62% overall efficiency in thermodynamic analysis, which is 77% higher than that of a comparable Brayton cycle turbogenerator. For this configuration however, the gas turbine and fuel cell must have matching flow rates, and the specific heating of flow streams by fuel cell should match that of the combustor. This limits the operating envelope of both gas turbine and fuel cell.

**SOFC-turbogenerator range extender for road vehicles**

The paper "An Evaluation of Turbocharging and Supercharging Options for High-Efficiency Fuel Cell Electric Vehicles" [35] also delves into the potential of Solid Oxide Fuel Cells (SOFCs) as range extenders for electric vehicles (EVs), presenting a promising alternative to enhance EV driving range and efficiency. The study examines a scenario where a 24-kWh electric vehicle incorporates a 5 kW SOFC stack along with a gas turbine recovery system. This configuration significantly increases the vehicle's driving range by 252%, enabling it to exceed 600 kilometres with a single hydrogen tank of 6.2 kg. This increase in driving range underlines the SOFC's potential for transportation applications, especially as a range extender in EVs. The integration of SOFC technology not only contributes to extending the electric vehicle's range but also aligns with the broader goal of reducing carbon emissions and dependence on fossil fuels in the transportation sector. The findings suggest that SOFC-equipped EVs could represent a critical

step forward in achieving longer, more efficient driving capabilities, thereby enhancing the viability and appeal of electric vehicles in the quest for sustainable transportation solutions.

*Bypass flow:* Fuel cell bypass for both air and fuel streams can widen the hybrid system's operating range and dynamic response without adversely impacting fuel cell durability. Jia et al [51] suggested and proved the feasibility of an operating strategy for military ground vehicle SOFC-GT system where the fuel cell is maintained at nearly steady state conditions where it provides the baseline power requirement and the transient load changes are met by the gas turbine which has good dynamic response. This strategy will have to sacrifice on system efficiency at high load conditions, but is one that is suited to aircraft operation, especially long-duration missions, where most of the time is spent in cruise condition where load is nearly constant; and take-off and climb conditions require good dynamic response.
It is important to find the optimum power-split and consequently size-ratio between the fuel cell and the gas turbine. For a given power output, a hybrid system with a large turbine and fuel cell bypass flow will allow the fuel cell to operate at part-load conditions where rate of degradation is low but system efficiency will be low too because the gas turbine – which is less efficient than a SOFC – produces a larger portion of the work output, while one with a smaller gas turbine will give better efficiency but with limited dynamic range and possibly a higher rate of cell degradation [52].

*Off-gas recirculation:* Anode and cathode channel exhaust gas recirculation can increase system efficiency by achieving higher fuel utilisation rates in the SOFC with reduced degradation and improving pre-heating of air and fuel streams entering the fuel cell stack [53]. The NASA FUELEAP project investigated an SOFC-GT system for small passenger aircraft on their X-57 demonstrator. The system that uses de-sulphurised diesel fuel with on-board reforming showed 62% overall efficiency with SOFC exhaust recycling and the ability to carry more than 40% the payload as a comparable petrol-powered plane (Tecnam P2006T) on a 1000 km mission while consuming 43% less energy [54]. The main challenges that need to be addressed with this system are the development of blowers that can operate at more than 800°C to recycle SOFC exhaust gases and making the SOFC stack and fuel system lighter to increase payload capabilities [55]

Bypass flow and off-gas recirculation strategies require complicated control systems of valves, blowers and ejectors to ensure that temperatures, fuel and air distribution, fuel utilisation and stack current are kept at desired values under the various loads and atmospheric conditions encountered in aircraft application [56]. There is also the challenge of keeping system weight low even after addition of the extra components required to implement these operating strategies because while they improve efficiency and dynamic performance, it is equally important for the system to achieve its target value for power-to-weight ratio.

*Multi-stack configurations* were explored by P Aguiar et al [57] for UAVs that undertake week-long missions. The study showed that a three-stack configuration, where air flows in series through the stacks and fuel flows in parallel, is capable of 66.3% overall efficiency and 74% lower specific fuel consumption than a conventional turboprop engine. For the same power output, the required air flowrate was lowered by just over 70% and fuel flowrate by 18% by using three stacks instead of one. The reduced air-flow rate means smaller turbomachinery and other components can be used, but it also means that more heat exchangers, piping, and stack supports are required, and that the system becomes more complicated and heavier. Therefore, for a given performance target, there exists a point where efficiency gained by splitting the fuel cell into more stacks does not justify the increase in system weight and that point should be identified while designing such a system.

**Combination of SOFC-turbofan and SOFC-turbogenerator**

Aircraft concepts that make use of both configurations of SOFC-GT systems discussed above have been analysed in the past. Esteban Valencia et al [58] proposed a Turboelectric Distributed Propulsion system where 25% of the thrust is provided by an SOFC-integrated turbofan and 75% by distributed propulsors with superconducting motors powered by the SOFC with liquid hydrogen as fuel and coolant. Thermodynamic analysis at the design point (cruise conditions) showed a 70% lower thrust specific fuel consumption compared with a turbojet, however, parametric models for mass showed a 40% increase in total system mass [58]. Similarly, a Blended-Wing-Body (BWB) airframe for passenger flights powered by electric propulsors and SOFC-turbofans was conceived by K Okai et al [59]. Such systems demand a complete redesign of airframes to become reality.

The merits and challenges with the various configurations are summed up in Table 2.2 listing their merits and issues, focusing on power density and electrical efficiency.

**Table 2.2 Summary of SOFC-GT configurations**

| Configuration | | Merits | Issues |
|---|---|---|---|
| SOFC-GT generators [51], [52], [53], [55], [56], [57] | Hydrogen fuelled single stack with recuperative turbine | Overall efficiency greater than 65%; comparatively simple configuration | Poor dynamic performance; power density lower than 250 W/kg |
| | Hydrogen fuelled multiple stacks with recuperative turbine | Overall efficiency greater than 65%; lighter turbomachinery | Poor dynamic performance, power density lower than 200 W/kg |
| | Hydrocarbon fuelled single stack with gas recirculation and on-board reforming | Overall efficiency around 60%, power density of nearly 300 W/kg | $CO_2$ emissions; relatively complex configuration |
| | Hydrogen fuelled single stack with bypass flow | Dynamic performance comparable to microturbine-only systems, power density above 300 W/kg | Average efficiency lower than 60% |
| SOFC integrated turbojet/turbofan [48], [49], [58], [59] | Hydrogen fuelled SOFC-turbofan with electric propulsors | 70% reduction in thrust-specific fuel consumption compared to kerosene-fuelled turbofan | Dependent on the development of liquid $H_2$ storage, novel airframes, and superconducting electric machines. |
| | Reformer and SOFC integrated into turbofan | Higher electric power fractions and improved overall efficiency over traditional turbofan engines | Lower specific power and propulsive efficiency than traditional turbofan; increased drag |

Based on this summary, the "Hydrogen Fuelled Single Stack System with Bypass Flow" configuration offers a compelling compromise for transport applications. It provides a high power density (nearly 300 W/kg), which is critical for the weight-sensitive transport sector, while maintaining dynamic performance on par with conventional microturbine systems. Despite the average efficiency being slightly lower than some alternatives, the high power density and dynamic performance, crucial for transport applications, may well compensate for this. Moreover, the system's comparative simplicity could offer advantages in terms of reliability, maintenance, and cost over more complex configurations, making it a balanced choice for the transportation sector, where a mix of efficiency, performance, and practicality is essential.

Another observation is that SOFC-GT generator system for on-board electricity (auxiliary power) are more promising than propulsive power sources for passenger aircraft. The only applications where SOFC-GT systems are promising for propulsive power are in long-endurance, unmanned aircraft where mission profiles are relatively steady and multiple days long, with little to no payload requirements as the efficiency of power source is significantly more representative of good performance than power density [57], [60], [61].

## *2.2 Turbocharged PEMFC systems*

One of the primary benefits of turbocharged PEMFC systems is their ability to operate under a wide range of conditions, including high altitudes and low temperatures. In conventional pressured PEMFC systems, the air stream is pressurised by a compressor that is driven by an electric motor powered by the PEMFC stack itself. This “Turbine-less” system offers gains in stack efficiency, but some of that is negated by the parasitic power consumption of the motor. To tackle this, a turbine can be added to the system that is driven by the stack exhaust stream. The compressor and turbine together as one is called a “turbocharger” and is used to increase the air supply pressure to the fuel cell, which enhances the reaction rate and improves the cell's performance. Several studies have focused on improving the design and performance of turbocharged PEMFC systems and this literature review aims to provide an overview of them.

In their study, "An Evaluation of Turbocharging and Supercharging Options for High-Efficiency Fuel Cell Electric Vehicles," [35] Kerviel et al. delved into the enhancement of fuel cell vehicles (FCVs) through the implementation of advanced boosting systems. Concentrating on proton exchange membrane fuel cells (PEMFCs) that operated at approximately 80°C, this research investigated the efficacy of electric-assisted turbochargers (E-turbochargers) and electric compressors (superchargers), in both single and dual-stage configurations, as alternatives to conventional screw and scroll compressors. By employing a co-simulation approach integrating GT-SUITE and MATLAB/SIMULINK (Figure 2.4), the team assessed vehicle performance across the Worldwide Harmonised Light Vehicle Test Procedure (WLTP) driving cycle.

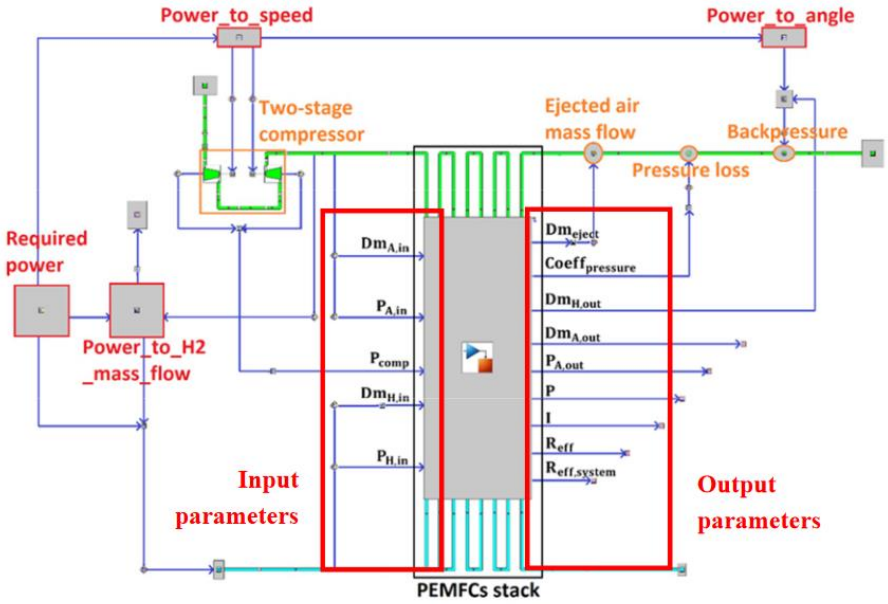


**Figure 2.4 Diagram of GT-Suite-MATLAB/Simulink co-simulation model [35]**

The findings revealed a marked improvement in vehicles equipped with E-turbochargers, exhibiting a 1.6% increase in electric system efficiency and a 3.7% extension in driving range, despite the associated increase in fuel cell stack size and weight required for the same output power. Notably, the integration of a turbine in the E-turbocharger setup underscored the advantage of energy recovery mechanisms within boosting systems, enabling better performance metrics for equivalent stack sizes when compared to vehicles using a single-stage compressor. The study also included the use of a 5 kW SOFC-GT system as a range extender. Although the efficiency of the turbocharged PEMFC system was found to be lower than that of the SOFC-GT system studied before, the 20% reduction in PEMFC stack size yielded an increase in gravimetric and volumetric power density that made it more suitable for light vehicle propulsion, while the SOFC-GT was better suited for range-extender duties.

Campanari et al [21] presented a comprehensive study on the feasibility and advantages of incorporating Polymer Electrolyte Membrane Fuel Cell (PEMFC) systems, particularly turbocharged configurations, into civil aircraft for onboard power production. The transition from conventional Auxiliary Power Units (APUs), which are primarily small gas turbine systems with limitations such as low efficiency and significant emissions, to PEMFC systems represents a paradigm shift towards achieving higher electrical efficiency and reduced emissions in aviation power systems. The turbocharged PEMFC system was studied by S. Campanari et al [21] as shown in Figure 2.5.

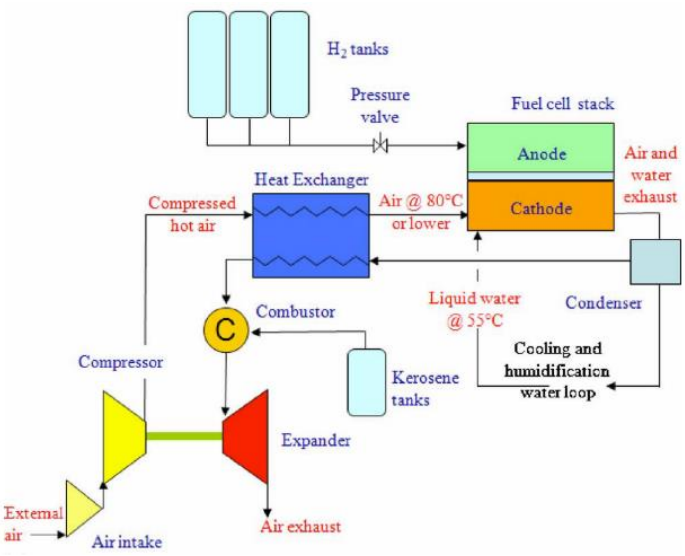


**Figure 2.5 Schematic of a turbocharged PEMFC system [21]**

The research explored various system configurations, including electrically driven compressors and turbocharger units, to optimise air compression for the PEM fuel cells under different operating conditions (ground operations, cruise conditions, and high-altitude low-speed flight) [21]. A key focus was on the pressurisation of the fuel cell system, which significantly influenced its performance and the physical integrity of the fuel cell. By employing a fuel cell simulation model, the study meticulously analysed the impacts of temperature, pressure, and system architecture on the cell voltage and efficiency [21]

Two prominent configurations were highlighted: a base case with an electrically driven compressor and an advanced case incorporating a turbocharger unit. The turbocharged PEMFC system, in particular, demonstrated superior performance by leveraging the expansion of exhaust gases for air compression, thus enhancing the system's overall efficiency. This configuration not only offered a path to higher electrical efficiency but also contributed to significant fuel savings and potential reductions in aircraft operational costs compared to traditional gas turbine APUs. A system efficiency of 48.7% at cruise was calculated with a 20% smaller PEMFC stack than that required for a PEMFC-only system with the same power output. Moreover, the environmental benefits of such systems, including the potential for zero NOx emissions, aligned with the growing emphasis on sustainable aviation practices.

In conclusion, turbocharged PEMFC systems have shown great potential in improving the efficiency and power density of fuel cell systems. The studies discussed in this review have proposed various designs and control strategies for turbocharged PEMFC systems, demonstrating their feasibility for transport and potential to provide a means to achieving higher efficiency, power density, and lower emissions.

## 2.3 Hydrogen storage

Comparing by lower heating values, liquid hydrogen carries 3 times more energy than conventional fuels for a given mass but has 12 times more specific volume. So, for the same amount of energy, liquid hydrogen occupies 4 times more space than conventional fuel despite only weighing one-thirds as much [62]. This means that in an aircraft powered by SOFC-GT, even with the increased efficiency – up to twice that of Brayton cycle gas turbine – lowering energy requirement, 2 to 2.5 times more fuel volume will need to be stored on-board for a given range. This requires a complete redesign of existing airframes [63]. However, liquefaction of hydrogen gas consumes more than 30% of its LHV and the SOFC-GT system must incorporate vaporisation of fuel thus increasing embodied energy and lowering efficiency of the system. Liquid $H_2$ is also volatile and requires cryogenic storage which is expensive and immature technology [64].

Compressed hydrogen gas at 70 MPa has 28 times the specific volume of jet fuel and hence requires approximately 4.5 times the volume of conventional fuel to match range. Weight fraction of 7% has been achieved in mass-production passenger cars as of 2017 and this figure, as well as specific volume and safety of storage are predicted to improve over succeeding years. For this reason, compressed gas is seen as the most promising storage method of hydrogen fuel in early stages of mainstream hydrogen-fuelled transportation [62].

Cryo-compressed systems combine the two methods discussed above to have compressed hydrogen gas stored at cryogenic temperatures. This method has volumetric and gravimetric storage capacities comparable to liquid storage but with reduced boil-off losses and lower storage pressures than compressed gas storage. Cryo-compressed $H_2$ is seen as a promising option for light and compact fuel storage after 2025 when the technology becomes mature for adoption [65].

Metal hydride tanks and chemical storage in alkaline earth metal hydrides have exhibited weight fractions comparable to compressed gas and $LH_2$ storage but, these methods have poor cyclability, reaction kinetics and suffer from chemical instability in their current form [64] which make them unsuitable for transient load applications like transport [66].

Compressed hydrogen gas emerges as the leading storage method for hydrogen fuel in transport applications when considering the trade-offs between energy density, volume, safety, and technological maturity. While liquid hydrogen offers a higher energy-mass ratio, its energy-intensive liquefaction process – reducing over 30% of its lower heating value – present notable challenges, especially for aviation where space and weight are at a premium. On the other hand, compressed hydrogen gas, while less energy-dense by volume compared to its liquid counterpart, offers a more practical solution given current technology. It avoids the complexities of cryogenic storage, has already achieved a 7% weight fraction in mass production vehicles,

and holds promise for further improvements. With advancements in materials and engineering expected to enhance its performance and safety profile, compressed hydrogen gas strikes a balance between efficiency, feasibility, and adaptability, making it a pragmatic choice for the near-term transition to hydrogen-powered transport.

# 3 Methodology

In this project, 0D models that represent the steady-state and transient behaviour of SOFC-GT systems and Turbocharged PEMFC systems were developed and their applications in preliminary stages of product design were demonstrated. This chapter presents the methodology followed: Section 3.1 describes the formulation of steady state and transient 0D models, specifically the equations and parameters used; Section 3.2 describes the execution of these models using the bond-graph approach; Section 3.3 describes the Monte-Carlo experiments performed on the steady state model; Section 3.4 describes how the transient models can be used in Model-in-the-Loop (MiL) simulations to predict performance across an operating cycle and perform model-based control.

## *3.1 0D modelling of systems*

The zero-dimensional, first principles-based approach was taken to modelling components of the fuel cell gas turbine systems in this project, where each component is represented by a group of equations and parameters that define the phenomena occurring within them. They are called “zero-dimensional (0D)” models because they assume thermodynamic states and properties within a given component remain uniform along spatial dimensions and often involve mass, energy, and momentum conservation equations. They include equations of state, constitutive relations, and simplified representations of mass and energy transfer mechanisms defined by the zeroth, first and second laws of thermodynamics, hence the name “First Principles”. This gives a simplified but computationally inexpensive representation of thermodynamic behaviour of complex systems, albeit at the expense of accuracy at the sub-component level. A well-parameterised 0D model should be accurate enough for predicting performance, sizing, and optimisation studies at the system-level with minimal increase in model complexity and hence computational cost [37], [40].

### 3.1.1 SOFC-GT steady state model

The SOFC-GT components are modelled by taking a first principles approach, i.e., applying conservation of mass and energy. The following assumptions were made while developing the model to find the right balance between accuracy and complexity. These assumptions were used in analytical models from previous studies that were described in the review in Chapter 2.1, and are made based on good engineering judgement and knowledge of the basics of thermodynamics, heat and mass transfer [67].

- The fuel cell, turbine, compressor, heat exchangers, and burner are modelled as individual lumped systems, i.e., each of them is a separate control volume. The thermodynamic states, mass flow and energy flow conditions in each control volume are variables that are

solved for by the mass and energy balance equations. The limitation from this assumption is that each control volume is represented by one set of variables, which means that it cannot predict unequal distribution of temperature, pressure, stresses, etc. on sub-components within these components. That would require models with spatial discretisation and higher order equations which comes with higher computational costs and time.

- The fuel cell stack is assumed to be single lumped collection of cells of unit area and user-specified PEN structure dimensions, that are stacked on top of each other and scaled up in area, but with homogenous distribution of temperature and current density. Therefore, the model cannot predict unequal distribution of reactants, pressure, temperature, and current densities across cells, but rather reports averaged values based on a uniform distribution. This assumption sacrifices absolute accuracy in predicting performance, especially under transient conditions [68], but is taken to keep computational costs and solve times low.
- Pressure losses and heat transfer in piping, manifolds and other connecting devices between the sub-systems are negligible. This assumption is made because the pressure drops from these components in system operating at elevated pressures are in the order of millibars and therefore have a negligible effect on system performance [26].
- Ideal gas behaviour is assumed for fuel and oxidant flow streams to simplify equations reduce computational load. This assumption was made as the study is concerned with fluid mixtures that do not contain more than three species whose behaviour does not deviate considerably from real gas behaviour under the conditions studied [69].
- Heat losses from the fuel cell stack to the environment is negligible. This assumption is made because in transport applications, the ideal FC-GT system is designed in such a way that as much of the heat dissipated from exothermic processes (e.g., fuel cell and combustion) are transferred to the endothermic processes (e.g., air and fuel heaters) [55], [61]. Although there are heat losses in a real system and it varies with design, the ideal condition was assumed for the study to give an idea of the maximum achievable efficiency.

The SOFC stack model is made up of three sub-models:

- Electrochemical model
- Mass balance model
- Energy balance model

**SOFC Electrochemical model [70]**

The relationship between the electrical performance (voltage and current) and reactant flow conditions is modelled by the electrochemical model.

It is a “grey-box” model as it is built on analytical equations with some empirical values which are listed alongside the equations in the following paragraphs. Figure 3.1 shows the relevant

variables and their interdependencies in the model.

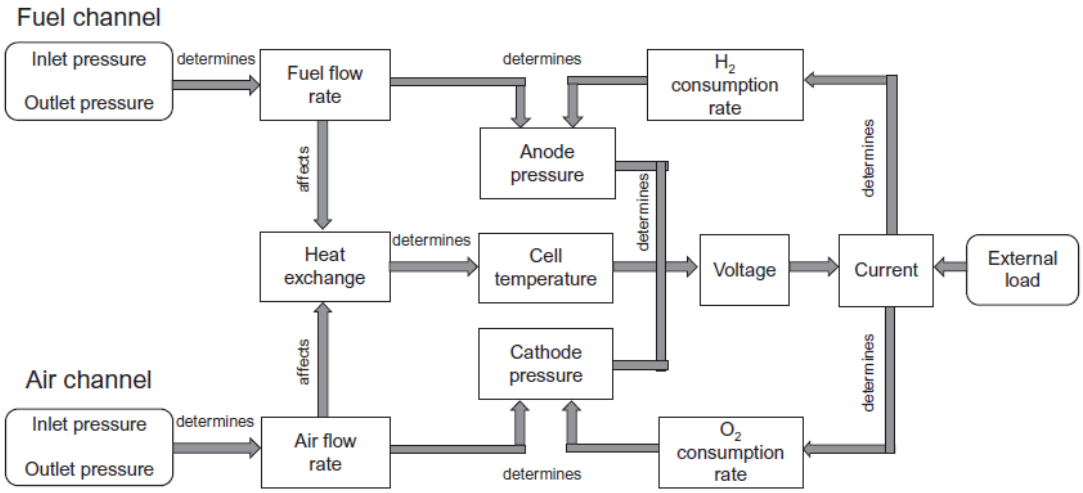


**Figure 3.1 P-diagram for SOFC electrochemical model [70]**

The hydrogen oxidation reaction that leads to voltage creation in an SOFC is given by Equation 3.1 [70].

**Equation 3.1**

$$\mathrm{H_2} + \frac{1}{2}\mathrm{O_2} \rightarrow \mathrm{H_2O}$$

Therefore, for every mole of hydrogen involved in the reaction, there are 2 moles of electrons and 0.5 moles of oxygen. These values are used in equations of the electrochemical model.

Open circuit voltage of an individual cell is given by the Nernst equation (Equation 1.1) rewritten as [70]:

**Equation 3.2**

$$V_{\text{nernst}} = 1.317 - 2.769 \times 10^{-4} \cdot T_{fc} + \frac{R \cdot T_{fc}}{2F} \ln\left(\frac{p_{\mathrm{H_2,\,anode}} \cdot p_{\mathrm{O_2,\,cathode}}^{1/2}}{p_{\mathrm{H_2O,\,anode}} \cdot p_{\mathrm{ref}}^{1/2}}\right)$$

Where,

- 1.317 = $\frac{\Delta H}{nF}$ , with enthalpy of reaction $\Delta H$ = 254 kJ/mol, and number of electrons transferred in reaction $n$ = 2.
- $2.769 \times 10^{-4} = \frac{\Delta S}{nF}$, with entropy of reaction $\Delta S$ = 53.4 J/(mol·K), and $n$ = 2.
- $T_{fc}$: Fuel cell operating temperature, in Kelvin.
- $R$: The universal gas constant (8.314 J/(mol·K)).
- $F$: Faraday's constant (approximately 96485 C/mol), which is the charge per mole of electrons.
- $p_{\mathrm{H_2,\,anode}}$ : Partial pressure of hydrogen at the anode.
- $p_{\mathrm{O_2,\,cathode}}$ : Partial pressure of oxygen at the cathode.

- $p_{H_2O,\ anode}$ : Partial pressure of water vapor at the anode.
- $p_{\mathrm{ref}}$: Reference pressure, which is 1 atm in this case.

*Activation losses:* The Butler Volmer equation is used to model activation losses in the fuel cell [70].

**Equation 3.3**

$$\eta_{\mathrm{act}} = \frac{RT_{fc}}{2aF}\ln\ I_0 - \frac{RT_{fc}}{2aF}\ln\ I$$

Where,

- $a$ : Charge transfer coefficient
- $I_0$ : Exchange current of the electrode-electrolyte pairing
- $I$ : Current drawn from the fuel cell

*Concentration losses***:** Polarisation losses arising due to the electrolyte-electrode boundary becoming starved of reactants, also known as concentration losses, is given by Equation 3.4 [70] that defines it as a function of cell temperature ($T_{fc}$) and limiting current ($I_{\mathrm{L}}$). $I_{\mathrm{L}}$ is a function of the cell geometry and materials and is the maximum current that can be drawn from a cell without completely starving the fuel cell of reactants in which case no voltage is produced by the cell.

**Equation 3.4**

$$\eta_{\mathrm{conc}} = \frac{RT_{fc}}{2F}\ln\left(1 - \frac{I}{I_{\mathrm{L}}}\right)$$

*Ohmic loss:* The third and most prominent polarisation loss in the fuel cell is the one due to ionic resistance in the electrolyte and electrodes. The formula for ohmic losses to fuel cell voltage is given by Equation 3.5 [70] where, $r_{T_{fc}}$ is the ohmic resistance of the cell at temperature $T_{fc}$.

**Equation 3.5**

$$\eta_{\mathrm{ohm}} = I.r_{T_{fc}}$$

Ohmic resistance $r_{T_{fc}}$ is a function of the cell temperature and defined by the following equation [70].

**Equation 3.6**

$$r(T_{\mathrm{fc}}) = r_0 \exp\left[\alpha\left(\frac{1}{T_{fc}} - \frac{1}{T_0}\right)\right]$$

where $\alpha$ is ohmic resistance coefficient, and $r_0$ is the resistance value at reference temperature $T_0$.

The SOFC stack voltage is given by Equation 3.7 [70] where $\mathrm{N_c}$ is the number of cells in the stack.

**Equation 3.7**

$$\mathrm{V_{fc}} = N_c.(V_{\mathrm{nernst}} - \eta_{\mathrm{act}} - \eta_{\mathrm{conc}} - \eta_{\mathrm{ohm}})$$

Current drawn from the SOFC is given by Equation 3.8 [70], where $\dot{n_{\mathrm{H_2}}}$ is the number of moles of hydrogen consumed by the fuel cell per unit time.

**Equation 3.8**

$$I = \dot{n}_{H_2} \cdot 2F$$

**SOFC Mass balance**

The mass balance model applies conservation of mass for all species interacting with the fuel cell stack and calculates the flowrates, mole fractions, and partial pressures for the given operating conditions.

In the SOFC, hydrogen reacts with oxygen to produce water vapour, i.e., $H_2$ and $O_2$ are consumed, and $H_2O$ is produced [9].

**Equation 3.9**

$$\mathrm{H_2(g)} + \frac{1}{2}\mathrm{O_2(g)} \rightarrow \mathrm{H_2O(g)}$$

The hydrogen oxidation reaction at the anode-electrolyte interface is [9]:

**Equation 3.10**

$$\mathrm{H_2(g)} + \mathrm{O^{2-}} =\!\rightarrow \mathrm{H_2O(g)} + 2\mathrm{e^-}$$

The oxygen reduction reaction at the cathode-electrolyte interface is [9]:

**Equation 3.11**

$$\mathrm{O_2(g)} + 4\mathrm{e^-} \rightarrow 2\mathrm{O^{2-}}$$

Two electrons are produced for every mole of $H_2$ consumed, so the mass balance of $H_2$ for a stack with $N_c$ number of cells is given by Equation 3.12 [9].

**Equation 3.12**

$$\dot{n}_{H_2} = \dot{n}_{H_2,in} - \dot{n}_{H_2,out} = \mathrm{N_c}\frac{I}{2F}$$

Where,

- $\dot{n}_{H_2}$: The number of moles of hydrogen consumed in the fuel cell stack.
- $\dot{n}_{H_2,in}$: The number of moles of hydrogen entering the fuel cell stack.
- $\dot{n}_{H_2,out}$: The number of moles of hydrogen exiting the fuel cell stack.
- $\mathrm{N_c}$: The number of cells in the fuel cell stack.

Four electrons are released per mole of $O_2$, so the molar consumption rate $\dot{n}_{O_2}$ for $O_2$ is given by Equation 3.13 [9]:

**Equation 3.13**

$$\dot{n}_{O_2} = \dot{n}_{O_2,in} - \dot{n}_{O_2,out} = \mathrm{N_c}\frac{I}{4F}$$

For every mole of hydrogen consumed, one mole of $H_2O$ produced, therefore, the molar flowrate $\dot{n}_{H_2O}$ for $H_2O$ is given by [9]:

**Equation 3.14**

$$\dot{n}_{H_2O} = \dot{n}_{H_2O,in} - \dot{n}_{H_2O,out} = -\mathrm{N_c}\frac{I}{2F}$$

The mass balance model also calculates partial pressures of reacting species in the air and fuel channels. Partial pressures are calculated from the molar concentrations of the species and pressure of incoming fluid streams by applying the ideal gas equation to relate pressure to molar flow rate.

**Equation 3.15**

$$P = \frac{\dot{n}RT}{V}$$

Where,

- $P$ is pressure.
- $\dot{n}$ is molar flowrate.
- $R$ is universal gas constant.
- $T$ is temperature.
- $V$ is volume

Therefore, the pressure of $O_2$, $H_2$, and $H_2O$ at inlet and outlet are given by [70]:

**Equation 3.16**

$$P_{O_2,in} = \frac{\dot{n}_{O_2,in}RT}{V}$$

**Equation 3.17**

$$P_{O_2,out} = \frac{\dot{n}_{O_2,out} RT}{V}$$

A linear change in pressure across the channels is assumed and therefore the partial pressure of each reactant used in the Nernst equation is the mean of inlet and outlet values. Hence, the partial pressures are given by the following equations:

**Equation 3.18**

$$P_{O_2} = \frac{0.5 \times (\dot{n}_{O_2,in} + \dot{n}_{O_2,out}) RT}{V}$$

**Equation 3.19**

$$P_{H_2} = \frac{0.5 \times (\dot{n}_{H_2,in} + \dot{n}_{H_2,out}) RT}{V}$$

**Equation 3.20**

$$P_{H_2O} = \frac{0.5 \times (\dot{n}_{H_2O,in} + \dot{n}_{H_2O,out}) RT}{V}$$

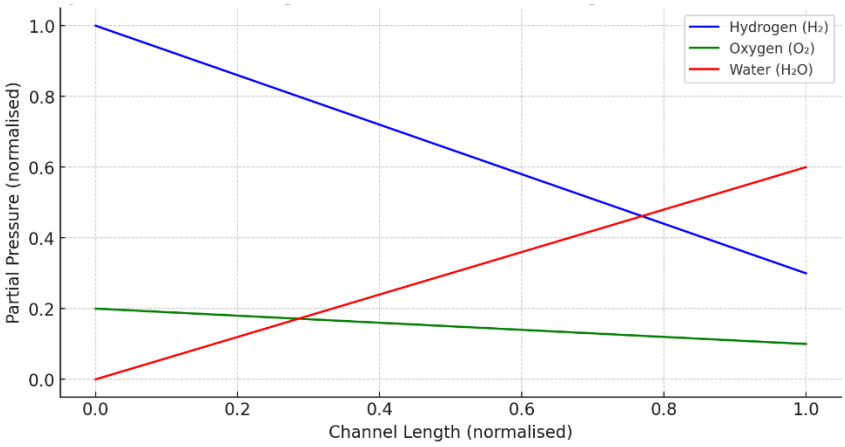


**Figure 3.2 Linear change in species partial pressures along fuel cell channel**

**SOFC Energy balance [23]**

Energy balance was applied across the SOFC inlet and outlet where the total of enthalpy of the inlet streams is equated to the sum of electric power, heat dissipated and enthalpy of outlet streams.

**Equation 3.21**

$$\dot{H_{\text{Fi}}} + \dot{H_{\text{Ai}}} = \dot{Q_{\text{FC}}} + P_{\text{el}} + \dot{H_{\text{Fo}}} + \dot{H_{\text{Ao}}}$$

Where,

- $\dot{H_{\text{Fi}}}$: Enthalpy flowrate of fuel at stack inlet
- $\dot{H_{\text{Ai}}}$: Enthalpy flowrate of air at stack inlet

- $\dot{Q_{FC}}$: Rate of net heat released from the stack
- $P_{el}$: Electric power produced by the stack
- $\dot{H_{Fo}}$: Enthalpy flowrate of fuel stream at stack outlet
- $\dot{H_{Ao}}$: Enthalpy flowrate of air stream at stack outlet

The enthalpy flowrate $\dot{H}$ of a fluid stream at temperature $T$ is given by the Equation 3.22.

**Equation 3.22**

$$\dot{H} = \dot{m} C_p (T - T_{ref})$$

Where,

- $\dot{H}$: Enthalpy flowrate
- $\dot{m}$: Mass flowrate of the stream
- $C_p$: Isobaric Specific Heat Capacity of the fluid
- $T_{ref}$: Reference temperature at which the value of $C_p$ is known.
- $T$: Temperature of fluid stream.

Electric power $P_{el}$ is the product of stack voltage $V_{fc}$ and electric current produced $I$.

**Equation 3.23**

$$P_{el} = V_{fc}.I$$

Heat dissipated/released by the stack $\dot{Q}_{fc}$ is due to the irreversibility losses. It is given by the product of total overpotential ($\eta_{act} + \eta_{conc} + \eta_{ohm}$) and current drawn $I$:

**Equation 3.24**

$$\dot{Q}_{fc} = N_c.(\eta_{act} + \eta_{conc} + \eta_{ohm}).I$$

**Compressor model [67]**

The compressor is modelled as an adiabatic compression process with isentropic efficiency ($\eta_c$) . Isentropic efficiency is defined as the ratio of difference between isentropic outlet temperature and inlet temperature ($T_{2sc} - T_{1c}$) to the difference between actual outlet temperature and inlet temperature ($T_{2c} - T_{1c}$).

**Equation 3.25**

$$\eta_c = \frac{T_{2sc} - T_{1c}}{T_{2c} - T_{1c}}$$

The following equation gives the relationship between isentropic outlet temperature($T_{2sc}$), inlet temperature ($T_{1c}$), pressure ratio $\left(\frac{p_2}{p_1}\right)$ and specific gas ratio ($\gamma$).

**Equation 3.26**

$$T_{2sc} = T_{1c}\left(\frac{p_2}{p_1}\right)^{\frac{\gamma-1}{\gamma}}$$

Power demand from the compressor ($\dot{W}_c$) is given by multiplying the actual temperature difference with $\dot{m}_a$ the mass flowrate of air and, $c_{pa}$ the isobaric specific heat capacity of air.

**Equation 3.27**

$$\dot{W}_c = \dot{m}_a\, c_{pa}(T_{2c} - T_{1c})$$

**Turbine model [67]**

The turbine model follows a similar approach to the compressor model, but the isentropic efficiency $\eta_t$ is given by the Equation 3.28.

**Equation 3.28**

$$\eta_t = \frac{T_{1t} - T_{2t}}{T_{1t} - T_{2st}}$$

Actual turbine outlet temperature $T_{2t}$ is given as function of $\eta_t$ , inlet temperature $T_{1t}$ and isentropic outlet temperature by $T_{2st}$ :

**Equation 3.29**

$$T_{2t} = T_{1t} + \eta_t T_{1t}\left\{1 - \left(\frac{p_2}{p_1}\right)^{\frac{\gamma-1}{\gamma}}\right\}$$

Power produced by the turbine ($\dot{W}_t$) is given by the Equation 3.30 where, $\dot{m}_g$ is the mass flowrate of gases flowing through the turbine and $c_{pg}$ is the specific heat capacity of the gases.

**Equation 3.30**

$$\dot{W}_t = \dot{m}_g\, c_{pg}(T_{1t} - T_{2t})$$

**Heat exchangers [67]**

The heat exchanger is defined using an effectiveness ($\varepsilon$) model. The heat transfer ($q$) between the streams is given by Equation 3.31 where, $c_{p,min}$ is minimum specific heat capacity out of the two streams, $T_{h,in}$ is inlet temperature of the hot stream, and $T_{c,in}$ is inlet temperature of the cold stream.

**Equation 3.31**

$$q = \varepsilon c_{p,min}(T_{h,in} - T_{c,in})$$

Outlet temperatures of the cold and hot streams, $T_{c,\,out}$ and $T_{h,\,out}$ respectively are given by

Equations 3.32 and 3.33. $\dot{m}_c$ and $\dot{m}_h$ are mass flow rates of cold and hot streams respectively while $c_{p,c}$and $c_{p,h}$ are specific heat capacities.

**Equation 3.32**

$$T_{c,\,\text{out}} = T_{c,\,\text{in}} + q/\dot{m}_c c_{p,c}$$

**Equation 3.33**

$$T_{h,\,\text{out}} = T_{h,\,\text{in}} - q/\dot{m}_h c_{p,h}$$

**Burner [67]**

The burner is modelled as an adiabatic heat addition process with a heat transfer efficiency of $\eta_b$ which is defined as the ratio of heat transferred to the fluid stream ($q_b$) to heat added to the system ($\dot{m}_f \times LHV$). $\dot{m}_f$ is the mass flow rate of fuel consumed and $LHV$ is its lower heating value.

**Equation 3.34**

$$q_b = \eta_b\,(\dot{m}_f \times LHV)$$

Outlet temperature of gases ($T_{g,out}$) leaving the burner is calculated from inlet temperature ($T_{g,in}$) by Equation 3.35

**Equation 3.35**

$$T_{g,out} = T_{g,in} + \frac{q_b}{\dot{m}_g\, c_{pg}}$$

## 3.1.2 SOFC-GT transient model

**SOFC Stack Model**

Like the steady state model, the dynamic model too can be divided into electrochemical, mass balance, and energy balance sub-models. The electrochemical sub-model is the same as that used in the steady state model and described in section 3.1.1. However, the dynamic SOFC model uses first order differential equations to capture the change of mass and energy flow in the stack with respect to time.

*SOFC Mass Balance [70]*

Under dynamic flow conditions, the changing flowrates of fuel and oxidant streams influence partial pressures of hydrogen, oxygen, and water vapour in the channels, which in turn influences the electrochemical performance of the fuel cell. This model is based on the law of conservation of momentum.

The rate of change of hydrogen partial pressure ($p_{H_2}$) through the fuel cell channel is given by Equation 3.36.

**Equation 3.36**

$$\frac{\mathrm{d}p_{\mathrm{H_2}}}{\mathrm{d}t} = \frac{RT_{\mathrm{e}}}{V_{\mathrm{an}}}\left(n_{\mathrm{H_2}}^{\dot{\mathrm{in}}} - n_{\mathrm{H_2}}^{\dot{\mathrm{r}}}\right)$$

Where, $n_{\mathrm{H_2}}^{\dot{\mathrm{in}}}$ is the inlet molar flowrate of hydrogen, $n_{\mathrm{H_2}}^{\dot{\mathrm{r}}} = 2K_{\mathrm{r}}I$ is the molar rate of hydrogen consumption, $K_r = \frac{\mathrm{N_c}}{4\mathrm{F}}$ , $I$ is stack current. The outlet molar flowrate of hydrogen is given by Equation 3.37 where $K_{\mathrm{H_2}}$ is the specific molar valve constant of $H_2$, which is an empirical coefficient that related molar flowrate of a species to its pressure at channel or valve orifice. The value of this constant is dependent on the geometry of the channel:

**Equation 3.37**

$$n_{\mathrm{H_2}}^{\dot{\mathrm{out}}} = K_{\mathrm{H_2}}p_{\mathrm{H_2}}$$

Similarly, the pressures of oxygen and water vapour are given by Equations 3.38 to 3.43. The rate of change of pressure of oxygen $\frac{\mathrm{d}p_{\mathrm{O_2}}}{\mathrm{d}t}$ is given by Equation 3.38.

**Equation 3.38**

$$\frac{\mathrm{d}p_{\mathrm{O_2}}}{\mathrm{d}t} = \frac{RT_{\mathrm{e}}}{V_{\mathrm{an}}}\left(n_{\mathrm{O_2}}^{\dot{\mathrm{in}}} - n_{\mathrm{O_2}}^{\dot{\mathrm{r}}}\right)$$

Molar rate of oxygen consumption $\boldsymbol{n}_{\mathrm{O_2}}^{\dot{\mathrm{r}}}$ is given by Equation 3.39.

**Equation 3.39**

$$n_{\mathrm{O_2}}^{\dot{\mathrm{r}}} = K_{\mathrm{r}}I$$

Molar flowrate of oxygen at the outlet of the fuel cell is given by:

**Equation 3.40**

$$n_{\mathrm{O_2}}^{\dot{\mathrm{out}}} = K_{\mathrm{O_2}}p_{\mathrm{O_2}}$$

The rate of change of pressure of oxygen $\frac{\mathrm{d}\boldsymbol{p}_{\mathrm{H_2O}}}{\mathrm{d}\boldsymbol{t}}$ is given by Equation 3.41.

**Equation 3.41**

$$\frac{\mathrm{d}p_{\mathrm{H_2O}}}{\mathrm{d}t} = \frac{RT_{\mathrm{e}}}{V_{\mathrm{an}}}\left(n_{\mathrm{H_2}O}^{\dot{\mathrm{in}}} + n_{\mathrm{H_2}O}^{\dot{\mathrm{r}}}\right)$$

Molar rate of $H_2O$ production $\boldsymbol{n}_{\mathrm{H_2}\boldsymbol{O}}^{\dot{\mathrm{r}}}$ is given by Equation 3.42, and outlet molar flowrate $\boldsymbol{n}_{\mathrm{H_2O}}^{\dot{\mathrm{out}}}$ by Equation 3.43.

**Equation 3.42**

$$n_{\mathrm{H_2O}}^{\dot{\mathrm{r}}} = 2K_{\mathrm{r}}I$$

**Equation 3.43**

$$n_{\mathrm{H_2O}}^{\dot{\mathrm{out}}} = K_{\mathrm{H_2}O} p_{\mathrm{H_2}O}$$

*SOFC Energy balance [70]*

The energy balance sub-model divides the fuel cell stack into four control volumes, namely the electrode-electrolyte assembly, interconnect, anode channel, and cathode channel. First law of thermodynamics is applied to each control volume and a variable bulk temperature is assigned to each of them. The rate of change of that temperature is expressed as a function of heat transfer and work done. Ideal gas law is applied to both fluid streams and heat loss to the environment is assumed to be negligible.

Energy balance around the PEN (temperature $T_{\mathrm{e}}$) assembly is given by Equation 3.44:

**Equation 3.44**

$$\rho_e A_c \Delta w_e \overline{C_{pe}} \frac{\mathrm{d}T_{\mathrm{e}}}{\mathrm{d}t} = \left(Q_{\mathrm{dF}}^{\mathrm{in}} - Q_{\mathrm{dF}}^{\mathrm{out}}\right) + \left(Q_{\mathrm{dA}}^{\mathrm{in}} - Q_{\mathrm{dA}}^{\mathrm{out}}\right) - \left(Q_{hFe} + Q_{rF} + Q_{hAe} + Q_{rA}\right) - Q^r - \dot{W}$$

Where, $\rho_e$, $A_c$, $\Delta w_e$, $\overline{C_{pe}}$, and $T_{\mathrm{e}}$ are the density, surface area, thickness, specific heat capacity, and temperature of the PEN structure respectively.

$Q_{\mathrm{dF}}$ and $Q_{\mathrm{dA}}$ are diffusive heat transfer rates at fuel side and air side respectively and given by Equations 3.45 to 3.48:

**Equation 3.45**

$$Q_{\mathrm{dF}}^{\mathrm{in}} = n_{\mathrm{H_2}}^{\dot{\mathrm{r}}} \int_{T_{\mathrm{ref}}}^{T_{\mathrm{F}}} C_{p,\mathrm{H_2}}(T)\mathrm{d}\,T = 2K_{\mathrm{r}} I C_{\mathrm{p,H_2}}(T_{\mathrm{F}} - T_{\mathrm{ref}})$$

**Equation 3.46**

$$Q_{\mathrm{dF}}^{\mathrm{out}} = n_{\mathrm{H_2O}}^{\dot{\mathrm{r}}} \int_{T_{\mathrm{ref}}}^{T_{\mathrm{F}}} C_{p,\mathrm{H_2O}}(T)\mathrm{d}\,T = 2K_{\mathrm{r}} I C_{p,\mathrm{H_2O}}(T_{\mathrm{F}} - T_{\mathrm{ref}})$$

**Equation 3.47**

$$Q_{\mathrm{dA}}^{\mathrm{in}} = n_{\mathrm{O_2}}^{\dot{\mathrm{r}}} \int_{T_{\mathrm{ref}}}^{T_{\mathrm{A}}} C_{p,\mathrm{O_2}}(T)\mathrm{d}\,T = K_{\mathrm{r}} I C_{p,\mathrm{O_2}}(T_{\mathrm{A}} - T_{\mathrm{ref}})$$

**Equation 3.48**

$$Q_{\mathrm{dA}}^{\mathrm{out}} = 0$$

Where, $T_{\mathrm{F}}$ and $T_{\mathrm{A}}$ are fuel and air channel temperatures respectively, and $T_{\mathrm{ref}}$ is reference temperature at which specific heats of hydrogen ($C_{p,\mathrm{H_2}}$), oxygen ($C_{p,\mathrm{O_2}}$), and water vapour ($C_{p,\mathrm{H_2O}}$) are recorded.

$Q_{h\mathrm{Fe}}$ and $Q_{h\mathrm{Ae}}$ are convective heat transfer rates given by Equations 3.49 and 3.50, respectively.

**Equation 3.49**

$$Q_{h\mathrm{Fe}} = h_{\mathrm{Fe}} A_c (T_{\mathrm{e}} - T_F)$$

**Equation 3.50**

$$Q_{h\mathrm{Ae}} = h_{\mathrm{Ae}} A_c (T_{\mathrm{e}} - T_A)$$

Where, $h_{\mathrm{Fe}}$ and $h_{\mathrm{Ae}}$ are convective heat transfer coefficients for anode side and cathode side respectively and $T_{\mathrm{e}}$ is the temperature of the PEN structure.

$Q_{\mathrm{rF}}$ and $Q_{\mathrm{rA}}$ are radiative heat transfer rates at anode side and cathode respectively and are given by Equations 3.51 and 3.52, respectively.

**Equation 3.51**

$$Q_{\mathrm{rF}} = \frac{\sigma A_{\mathrm{c}} (T_{\mathrm{e}}^4 - T_{\mathrm{i}}^4)}{1/\epsilon_{\mathrm{a}} + 1/\epsilon_{\mathrm{i}} - 1}$$

**Equation 3.52**

$$Q_{\mathrm{rA}} = \frac{\sigma A_{\mathrm{c}} (T_{\mathrm{e}}^4 - T_{\mathrm{i}}^4)}{1/\epsilon_{\mathrm{c}} + 1/\epsilon_{\mathrm{i}} - 1}$$

Where, $\sigma$ is the Stefan-Boltzmann constant, $A_{\mathrm{c}}$ is cell area, and $\epsilon_{\mathrm{a}}$, $\epsilon_{\mathrm{c}}$, and $\epsilon_{\mathrm{i}}$ are the emissivity of anode, cathode, and interconnect materials respectively.

Equation 3.53 gives the rate of heat generation $Q^{\mathrm{r}}$ where $\Delta\widehat{H}_{\mathrm{r}}^{\circ}$ is enthalpy released by chemical reaction per mole of hydrogen.

**Equation 3.53**

$$Q^{\mathrm{r}} = -n_{\mathrm{H_2}}^{\dot{\mathrm{r}}} \Delta\widehat{H}_{\mathrm{r}}^{\circ} = -2K_{\mathrm{r}} I \Delta\widehat{H}_{\mathrm{r}}^{\circ}$$

Equation 3.54 give the electrical power output $\dot{W}$ as a function of stack voltage $V_{\mathrm{s}}$ and current output $I$.

**Equation 3.54**

$$\dot{W} = V_{\mathrm{s}} I$$

Similarly, energy balance around the interconnects (temperature $T_{\mathrm{i}}$) is given by Equation 3.55:

**Equation 3.55**

$$\rho_{\mathrm{i}} A_{\mathrm{i}} \Delta w_{\mathrm{i}} \overline{C_{p\mathrm{i}}} \frac{\mathrm{d}T_{\mathrm{i}}}{\mathrm{d}t} = Q_{h\mathrm{Fi}} + Q_{\mathrm{rF}} + Q_{h\mathrm{Ai}} + Q_{\mathrm{rA}}$$

Where, $Q_{h\mathrm{Fi}}$ and $Q_{h\mathrm{Ai}}$ are convective heat transfer rates between the fuel stream and interconnect, and the air stream and interconnect respectively.

Energy balance around the anode and cathode channels are given by Equations 3.56 and 3.57:

**Equation 3.56**

$$\sum \frac{p_i V_{\text{channel}}\, C_{pi}^{\text{out}}}{RT_F} \frac{\mathrm{d}T_F}{\mathrm{d}t} = \left(Q_F^{\text{in}} - Q_F^{\text{out}}\right) + \left(Q_{dF}^{\text{out}} - Q_{dF}^{\text{in}}\right) + \left(Q_{h\text{Fe}} - Q_{h\text{Fi}}\right)$$

**Equation 3.57**

$$\sum \frac{p_i V_{\text{channel}}\, C_{pi}^{\text{out}}}{RT_A} \frac{\mathrm{d}T_A}{\mathrm{d}t} = \left(Q_A^{\text{in}} - Q_A^{\text{out}}\right) + \left(Q_{dA}^{\text{out}} - Q_{dA}^{\text{in}}\right) + \left(Q_{h\text{Ae}} - Q_{h\text{Ai}}\right)$$

**Compressor and Turbine models**

Empirical maps are used to estimate the performance of the gas turbine part of the hybrid system. By knowing the mass flow rates and efficiencies at various operating points, one can calculate the power output, fuel consumption, and the overall efficiency of the system. The maps can be used in dynamic simulations to understand how compressor and turbine respond to changes in load demand, thermodynamic states, and other operational variables. In practice, the values for pressure ratio, isentropic efficiency and mass flowrates obtained from the operating points on these maps are used along with the isentropic work and pressure-temperature equations for calculating gas turbine performance under transient conditions.

Figures 3.3 and 3.4 show the compressor and turbine maps respectively for the APU of an aircraft. This APU has a rated power of 60 kW which is consistent with the electrical power demand for an Embraer KC-390 transport aircraft and obtained from MATLAB documentation for Brayton Cycle APU modelling [71]. This aircraft was chosen as it is one where payload and range are the main performance metrics rather than power density and is hence a suitable candidate for SOFC-GT power.

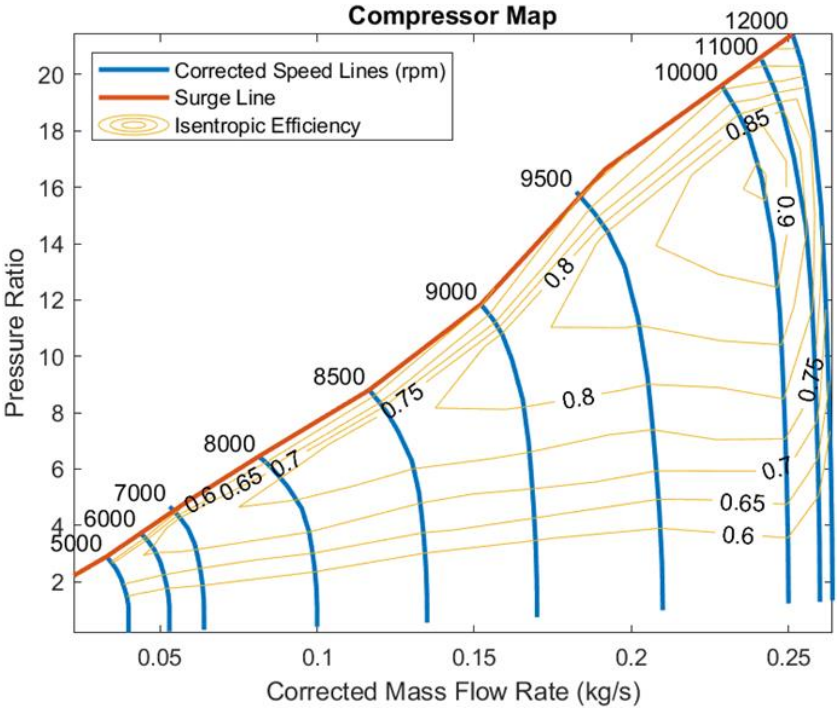


**Figure 3.3 Performance map used for compressor in the transient SOFC-GT model**

**Shaft speed lines:** The map shows performance curves for different speeds of the compressor (rpm), which represent the relationship between pressure ratio and mass flow rate for each speed.

**Surge Line:** The surge line indicates the lowest mass flow rates at which the compressor can operate without experiencing surge, which is a violent and unstable flow phenomenon.

**Efficiency Contours:** The isentropic efficiency contours indicate the efficiency of the compressor at various operating points. Isentropic efficiency is a measure of how close the process comes to the ideal reversible process.

**Operating Point:** By selecting a point on the map, you can determine the pressure ratio, mass flow rate, efficiency, and speed of the compressor. This is critical for matching the compressor performance to the specific requirements of the hybrid system.

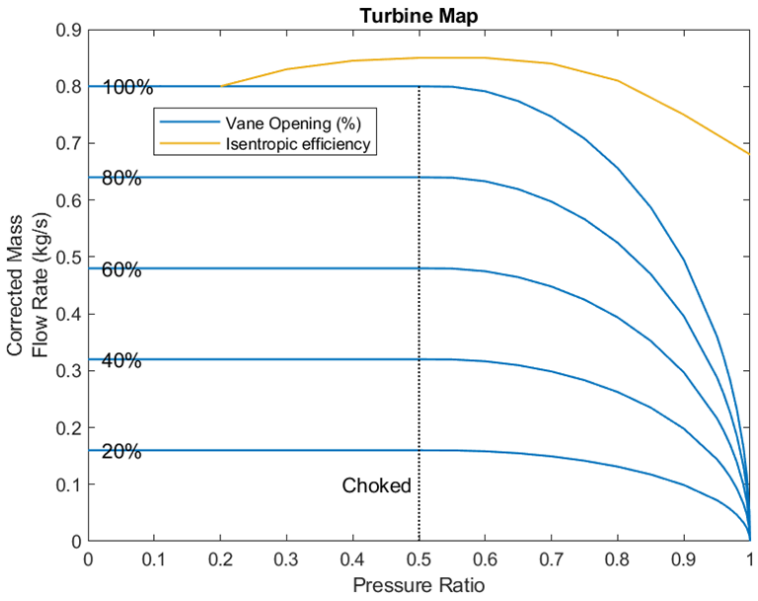


**Figure 3.4 Performance map used for turbine in the transient SOFC-GT model**

**Vane Opening Curves:** The turbine map includes curves for different vane openings, which indicate the flow capacity of the turbine at various pressure ratios.

**Isentropic Efficiency Contours:** Just like in the compressor map, isentropic efficiency contours show how efficiently the turbine can convert pressure into kinetic energy at different operating points.

**Choked Flow:** The map indicates the conditions under which the flow through the turbine becomes choked, meaning the mass flow rate does not increase with a decrease in downstream pressure.

**Operating Point:** By selecting a point on the turbine map, you can determine the mass flow rate, efficiency, and expansion ratio at which the turbine will operate.

### 3.1.3 Turbocharged PEMFC dynamic model

**PEMFC Stack model**

The PEMFC stack is modelled with a similar methodology to the SOFC stack, but the terms in the governing equations for the electrochemical reaction, charge, heat and mass and transfer are different due to difference in the mechanism of the energy conversion process.

*PEMFC Electrochemical model* [72]

The electrochemical model gives voltage, electrical resistance and polarisation characteristics of the fuel cell and comprises the following set of equations [13] [73]:

The OCV or Nernst Potential of a PEMFC cell is given by Equation 3.58

**Equation 3.58**

$$E_{Nernst} = \frac{\Delta G}{2F} + \frac{RT}{2F} log\left(\frac{p_{H_2} p_{O_2}^{0.5}}{p_{H_2O} p_{std}}\right)$$

- $\Delta G$: Change in Gibbs free energy for the reaction
- $F$: Faraday's constant, approximately 96485 C $mol^{-1}$, which represents the charge per mole of electrons.
- $R$: Universal gas constant, approximately 8.314 J $mol^{-1}K^{-1}$
- $T$: Absolute temperature in kelvin (K).
- $p_{H_2}$: Partial pressure of hydrogen gas.
- $p_{O_2}$: Partial pressure of oxygen gas.
- $p_{H_2O}$: Partial pressure of water vapor.
- $p_{std}$: Standard pressure, usually taken as 1atm or 101.325 kPa

Activation polarisation is given by the Tafel equation (Equation 3.59):

**Equation 3.59**

$$\eta_{\text{act}} = \frac{RT}{2\alpha F}\ log\left(\frac{i}{i_0}\right)$$

- $\eta_{\text{act}}$: Activation polarisation, related to the activation energy barrier for the electrochemical reaction.
- $i$: Current density (current per unit area).
- $i_0$: Exchange current density, which is the current density at which the rates of the forward and reverse reactions are equal at equilibrium.
- $\alpha$: Charge transfer coefficient, a dimensionless number that represents the symmetry factor of the energy barrier for the electrochemical reaction.

Concentration polarisation is given by a similar equation to SOFC:

**Equation 3.60**

$$\eta_{\text{conc}} = \frac{RT}{2F}\ln\left(1 - \frac{i}{i_{\text{L}}}\right)$$

- $\eta_{\text{conc}}$: Concentration polarisation, which arises due to the concentration gradients of reactants/products at the electrode/electrolyte interface.
- $i_{\text{L}}$: Limiting current density, which is the current density at which the rate of diffusion of the reactants to the electrode surface is equal to the rate of the electrochemical reaction.

Ohmic polarisation is given by the Equation 3.61.

**Equation 3.61**

$$\eta_{\text{ohm}} = I\left(\frac{t_{electrolyte}}{\sigma}\right)$$

Where, $t_{electrolyte}$ is thickness of the electrolyte, and $\sigma$ is ionic conductivity of the electrolyte. Ionic conductivity of the membrane is its ability to conduct ionic charge through it and is mathematically equal to the charge transfer rate per unit area (current density) per unit potential difference. $\sigma$ is a function of temperature, humidity, and partial pressures of the membrane and the reacting species over it. $\sigma$ is given by Equation 3.62 [73]

**Equation 3.62**

$$\sigma = \left(0.00514\frac{M_{\text{m,dry}}}{\rho_{\text{m,dry}}}C_{\text{wa}} - 0.00326\right)\exp\left(1268\left(\frac{1}{303} - \frac{1}{T}\right)\right) \times 10^2$$

Where, $M_{\text{m,dry}}$ is equivalent weight of a dry membrane in kg/mol

$\rho_{\text{m,dry}}$ density of dry membrane in kg/m$^3$

$C_{\text{wa}}$ concentration of water at anode in mol/m$^3$

$T$ is cell temperature in kelvin.

*PEMFC Mass balance model* [72]

The mass balance equations describe how the mass of each component (hydrogen, water, oxygen, nitrogen) within the fuel cell changes over time due to electrochemical reactions, phase changes, and flow of gases in and out of the fuel cell system. The equations are fundamental to understanding the operation and efficiency of a fuel cell and are used to predict the behaviour of the system under different operating conditions.

**Equation 3.63**

$$\frac{\mathrm{d}m_{\text{H}_2}}{\mathrm{d}t} = q_{A,\text{ in}}\frac{m_{\text{H}_2,\text{ in}}}{m_{\text{H}_2,\text{ in}} + m_{w,g,A,\text{ in}}} - \frac{I_{\text{stack}}N_{cell}}{2F}M_{\text{H}_2} - \left(q_{A,\text{ out}} + q_{purge}\right)\frac{m_{\text{H}_2}}{m_{\text{H}_2} + m_{w,g,A}}$$

**Equation 3.64**

$$\frac{\mathrm{d}m_{w,g,A}}{\mathrm{d}t} = q_{A,\,\mathrm{in}}\,\frac{m_{w,g,A,in}}{m_{\mathrm{H_2,\,in}} + m_{w,g,A,\,\mathrm{in}}} - \alpha \cdot \frac{I_{\mathrm{stack}}\,N_{cell}}{2F} M_{\mathrm{H_2}O} - \left(q_{A,\,\mathrm{out}} + q_{purge}\right)\frac{m_{w,g,A}}{m_{\mathrm{H_2}} + m_{w,g,A}}$$

**Equation 3.65**

$$\frac{\mathrm{d}m_{\mathrm{O_2}}}{\mathrm{d}t} = q_{C,\,\mathrm{in}}\,\frac{m_{\mathrm{O_2,\,in}}}{m_{\mathrm{O_2,\,in}} + m_{\mathrm{N_2,\,in}} + m_{w,g,C,\,\mathrm{in}}} - \frac{I_{\mathrm{stack}}\,N_{\mathrm{cell}}}{4F} M_{\mathrm{O_2}} - q_{C,\,\mathrm{out}}\,\frac{m_{\mathrm{O_2}}}{m_{\mathrm{O_2}} + m_{\mathrm{N_2}} + m_{w,g,C}}$$

**Equation 3.66**

$$\frac{\mathrm{d}m_{\mathrm{N_2}}}{\mathrm{d}t} = q_{C,\,\mathrm{in}}\,\frac{m_{\mathrm{N_2,\,in}}}{m_{\mathrm{O_2,\,in}} + m_{\mathrm{N_2,\,in}} + m_{w,g,C,\,\mathrm{in}}} - q_{C,\,\mathrm{out}}\,\frac{m_{\mathrm{N_2}}}{m_{\mathrm{O_2}} + m_{\mathrm{N_2}} + m_{w,g,C}}$$

**Equation 3.67**

$$\frac{\mathrm{d}m_{w,g,C}}{\mathrm{d}t} = q_{C,\,\mathrm{in}}\,\frac{m_{w,g,C,\,\mathrm{in}}}{m_{\mathrm{O_2,\,in}} + m_{\mathrm{N_2,\,in}} + m_{w,g,C,\,\mathrm{in}}} - (1+2\alpha)\frac{I_{\mathrm{stack}}\,N_{cell}}{2F} M_{\mathrm{H_2O}} - q_{C,\,\mathrm{out}}\,\frac{m_{w,g,C}}{m_{\mathrm{O_2}} + m_{\mathrm{N_2}} + m_{w,g,C}} - \frac{\mathrm{d}m_{w,g\to l}}{\mathrm{d}t}$$

**Equation 3.68**

$$\frac{\mathrm{d}m_{w,l,C}}{\mathrm{d}t} = \frac{\mathrm{d}m_{w,g\to l}}{\mathrm{d}t} - q_{C,\,\mathrm{out}}\,\frac{m_{w,l,C}}{m_{\mathrm{O_2}} + m_{\mathrm{N_2}} + m_{w,\mathrm{g},C}}$$

**Equation 3.69**

$$\alpha = \frac{q_{\mathrm{mem,\,H_2O,\,net}}}{q_{\mathrm{mem,}\,H^{+}\mathrm{net}}}$$

- $\frac{\mathrm{d}m_{\mathrm{H_2}}}{\mathrm{d}t}$: Rate of change of hydrogen mass in the fuel cell.
- $\frac{\mathrm{d}m_{w,g,A}}{\mathrm{d}t}$: Rate of change of water mass in the gas phase at the anode.
- $\frac{\mathrm{d}m_{\mathrm{O_2}}}{\mathrm{d}t}$: Rate of change of oxygen mass in the fuel cell.
- $\frac{\mathrm{d}m_{\mathrm{N_2}}}{\mathrm{d}t}$: Rate of change of nitrogen mass in the fuel cell.
- $\frac{\mathrm{d}m_{w,g,C}}{\mathrm{d}t}$: Rate of change of water mass in the gas phase at the cathode.
- $\frac{\mathrm{d}m_{w,l,C}}{\mathrm{d}t}$: Rate of change of water mass in the liquid phase at the cathode.

For each of these derivatives, the terms on the right side of the equation represent:

- $q_A$: Molar flow rate of the anode.
- $q_C$: Molar flow rate of the cathode.
- $m_{\mathrm{H_2,\,in}}$ : Molar mass of incoming hydrogen.
- $m_{w,g,A,in}$: Molar mass of water in the gas phase at the anode inlet.
- $m_{\mathrm{O_2,\,in}}$ : Molar mass of incoming oxygen.
- $m_{\mathrm{N_2,\,in}}$ : Molar mass of incoming nitrogen.
- $m_{w,g,C,in}$: Molar mass of water in the gas phase at the cathode inlet.
- $I_{\mathrm{stack}}$ : Current of the entire fuel cell stack.

- $N_{\text{cell}}$ : Number of cells in the stack.
- $M_{\text{H}_2}$: Molar mass of hydrogen.
- $M_{\text{O}_2}$: Molar mass of oxygen.
- $q_{purge}$: Flow rate of purge gas.
- $\alpha$: Ratio of net water generated to net hydrogen consumed.
- $M_{\text{H}_2O}$: Molar mass of water.
- $q_{A,\text{ out}}$ , $q_{C,\text{ out}}$ : Molar flow rate out of the anode and cathode, respectively.
- $\text{d}m_{w,g\rightarrow l}$: Rate of change of water mass transferring from gas to liquid phase.
- $q_{\text{mem, H}_2\text{O, net}}$ : Net water flux across the membrane.
- $q_{\text{mem, }H^+\text{net}}$ : Net proton flux across the membrane.

*PEMFC Energy balance* [13], [74]

Transfer of energy between the fluid streams and the solid parts of the PEMFC stack are modelled by the energy balance sub-model.

**Equation 3.70**

$$Q_{\text{latent}} = H_\gamma \cdot \frac{\text{d}}{\text{d}t}\left(\Delta m_{w,g\rightarrow l} - \Delta m_{w,l\rightarrow g}\right)$$

**Equation 3.71**

$$m_{\text{stack}}\, C_{p,\text{ stack}} \left(\frac{\text{d}T_{\text{stack}}}{\text{d}t}\right) = Q_{\text{theo}} - Q_{\text{elec}} - Q_{\text{conv}} - Q_{\text{loss}} - Q_{\text{latent}}$$

**Equation 3.72**

$$Q_{\text{theo}} = \dot{N}_{\text{H}_2,\text{ cons}} \cdot \Delta H_{\text{rxn}}$$

**Equation 3.73**

$$Q_{\text{elec}} = N_{\text{cell}} \cdot V_{\text{cell}} \cdot i_{\text{stack}}$$

**Equation 3.74**

$$Q_{\text{conv}} = \sum_{k\in\{\text{H}_2,\text{O}_2,\text{ N}_2,\text{H}_2\text{O}\}} q_{k,\text{ out}}\, C_{p,k}(T_{\text{out}} - T_{\text{stack}}) - \sum_{k\in\{\text{H}_2,\text{O}_2,\text{ N}_2,\text{H}_2\text{O}\}} q_{k,in} C_{p,k}(T_{\text{in}} - T_{\text{stack}})$$

**Equation 3.75**

$$Q_{\text{loss}} = h_{nc} A_{\text{stack}}\,(T_{\text{stack}} - T_{\text{amb}})$$

- $m_{\text{stack}}$ : Mass of the fuel cell stack.
- $C_{p,\text{ stack}}$ : Specific heat capacity of the stack at constant pressure.
- $\frac{\text{d}T_{\text{stack}}}{\text{d}t}$: Rate of change of the stack temperature with time.

- $Q_{\text{theo}}$ : Theoretical heat generated, which is the product of the hydrogen consumption rate ($\dot{N}_{\text{H}_2,\text{ cons}}$) and the heat of reaction ($\Delta H_{\text{rxn}}$).
- $Q_{\text{elec}}$ : Electrical energy produced, calculated as the number of cells ($N_{\text{cell}}$), the voltage of each cell ($V_{\text{cell}}$), and the current of the stack ($i_{\text{stack}}$).
- $Q_{\text{conv}}$ : Convective heat transfer, which includes the sum of the heat carried out by the exhaust gases minus the heat brought in by the incoming gases. $q_{k,\text{ out}}$ and $q_{k,in}$ are the molar flow rates of gas $k$ out of and into the stack, respectively, and $C_{p,k}$ is the specific heat capacity of gas $k$ at constant pressure.
- $T_{\text{out}}$ and $T_{\text{in}}$ : Temperatures of the gases flowing out of and into the stack, respectively.
- $T_{\text{stack}}$ : Temperature of the stack.
- $Q_{\text{loss}}$ : Heat losses from the stack to the surroundings, calculated with the heat transfer coefficient ($h_{nc}$), the surface area of the stack ($A_{\text{stack}}$, and the difference between the stack temperature ($T_{\text{stack}}$) and the ambient temperature ($T_{\text{amb}}$).
- $Q_{\text{latent}}$ : Latent heat associated with phase change of water in the fuel cell, calculated using the enthalpy of vaporisation ($H_{\gamma}$) and the rate of change of the mass of water in gas form ($\Delta m_{w,g\rightarrow l}$) and liquid form ($\Delta m_{w,l\rightarrow g}$).

**Humidifier model [74]**

The air and fuel streams entering a PEMFC stack have to be humidified to ensure ion conduction through the electrodes and membrane electrolyte. In the PEMFC system model, the humidifiers are modelled as moisture sources that add water vapour to the streams at constant temperature and pressure to reach a desired relative humidity at stack inlet.

The equation to find the change in the humidity ratio ($\Delta W$) required to adjust the relative humidity from an initial state to a final state at a constant temperature and pressure is given by Equation 3.76.

**Equation 3.76**

$$\Delta W = W_{\text{final}} - W_{\text{initial}}$$

where:

- $W_{\text{final}}$ is the humidity ratio at saturation (100% relative humidity) at the same temperature.
- $W_{\text{initial}}$ is the initial humidity ratio at the initial relative humidity (X%).

Both $W_{\text{final}}$ and $W_{\text{initial}}$ can be calculated using the equation 3.77.

**Equation 3.77**

$$W = \frac{r \cdot \phi \cdot P_{\text{w}}}{P - \phi \cdot P_{\text{w}}}$$

where:

- $W$ is the humidity ratio,

- $\phi$ is the relative humidity (as a decimal),
- $P_w$ is the saturation vapor pressure of water at the stream temperature,
- $P$ is the total pressure of the gas-water vapor mixture, and
- $r$ is the ratio of the gas constant of gas to the gas constant of water vapor.

The mass flow rate of water vapor ($\dot{m}_{vapor}$) to be added can be calculated from the mass of dry gas ($\dot{m}_{dry}$) using Equation 3.78.

**Equation 3.78**

$$\dot{m}_{vapor} = \Delta W \cdot \dot{m}_{dry}$$

Power consumed by the humidifier ($Q$) is given by Equation 3.79.

**Equation 3.79**

$$Q = \dot{m}_{vapour} \cdot h_{fg}$$

Where, $h_{fg}$ is the specific enthalpy of vaporisation of water, typically around 2260 kJ/kg at 100°C, but this value can vary slightly with temperature.

**Turbine and Compressor models**

Like the SOFC-GT model, turbine, and compressor models in the transient PEMFC system models are also modelled based on performance maps. The maps used in this model come from Chapter 12 of "Fuel Cell Systems Explained" by Dicks and Rand [9] and are sized for a PEMFC stack with maximum power output of 250 kW.

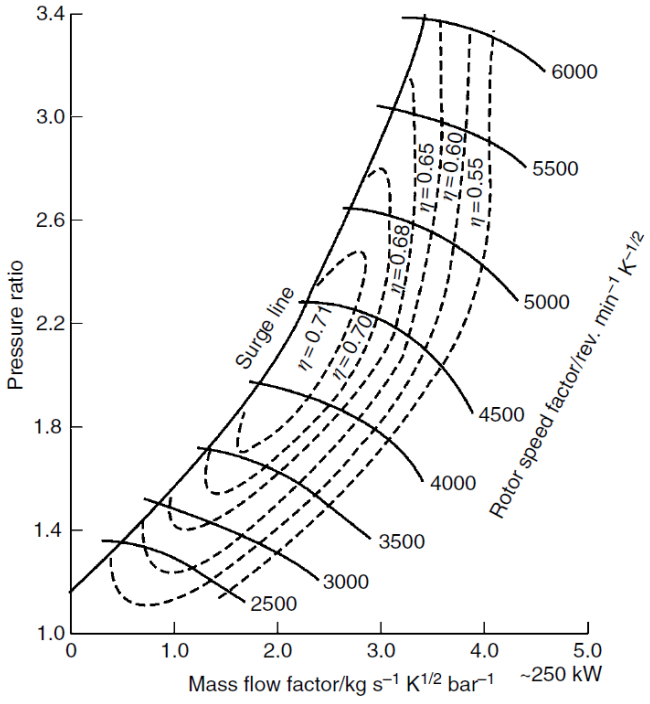


**Figure 3.5 Performance map used for compressor in transient PEMFC system model [9]**

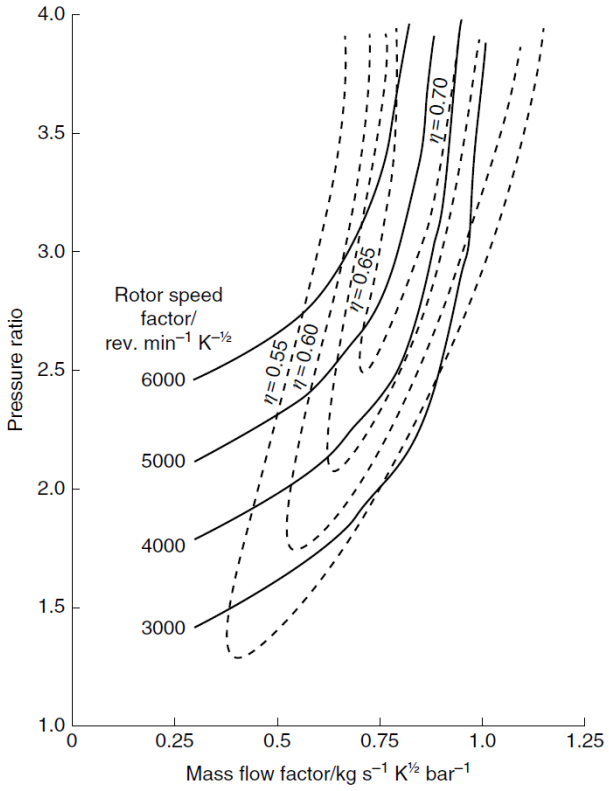


**Figure 3.6 Performance map used for turbine in the transient PEMFC system model [9]**

## *3.2 Bond-graph modelling*

Bond graph modelling is a graphical approach used for system-level modelling and analysis of dynamic systems, particularly in engineering and physics. It provides a unified representation of different energy domains (such as mechanical, electrical, hydraulic, and thermal) and their interactions within a single framework. Bond graphs are composed of components connected by bonds, where components represent physical elements like resistors, pipes, compressors, batteries, etc. The elements themselves are made up of equations that represent the physical phenomena that happen in those elements and the bonds between them carry the inputs and outputs to those equations [75], [76], [77]. Advantages of Bond Graph Modelling are:

**Unified Representation**: Bond graphs provide a unified and coherent way to represent complex systems that involve multiple energy domains. This makes it easier to understand the interactions and interdependencies between different components. Therefore, it is a very suitable modelling approach for this project where the primary users of the models will be researchers and engineers who do not have a lot of experience in model development but have a grasp of the physical phenomena and engineering knowledge required to set parameters and boundary conditions.

**Causality and Dynamics**: Bond graphs inherently capture the causal relationships between different components in a system. This enables the modelling of dynamic behaviour, allowing

for the analysis of system response over time to changing parameters and operating conditions.

**Modelling Flexibility:** Bond graphs can model a wide range of physical systems, from mechanical and electrical systems to chemical processes. This versatility makes them suitable for interdisciplinary applications.

**Physical Interpretation**: Bond graphs offer a clear physical interpretation of the modelled system, making it easier to relate the graphical representation to real-world phenomena.

**Hierarchical Representation**: Large and complex systems can be broken down into smaller subsystems represented by individual bond graphs. This hierarchical approach simplifies the analysis and design of intricate systems.

**Causal Loop Analysis**: Bond graphs naturally highlight causal loops within a system. This is crucial for identifying feedback mechanisms and potential stability issues.

**System Analysis and Design**: Bond graphs facilitate system analysis, such as examining energy flows, power dissipation, and overall system behaviour. They are also useful for design tasks like controller synthesis and optimisation.

**Modelling Dynamic Interactions**: Bond graphs excel at capturing interactions between components, helping to analyse how changes in one part of a system affect other parts.

**Education and Communication**: Bond graphs are used in academia and industry for teaching and communicating system dynamics. Their visual nature aids in explaining complex concepts to students, researchers, and stakeholders.

**Model-based Control**: Bond graphs can be used to develop and analyse control strategies for complex systems, enabling the design of effective control systems.

This approach is particularly advantageous for complex systems like fuel cells, where electrical, chemical, thermal, and mechanical energies interact. The bond-graph methodology, by abstracting these interactions into energy exchanges represented by bonds, enables a holistic analysis of system dynamics and performance that does not require the user of the models to be well-versed in programming languages. This versatility and efficiency of bond-graph modelling in capturing the interplay of various energy domains make it an excellent choice for developing 0D analytical models for systems engineering.

### 3.2.1 SOFC-GT Steady state model

A bond-graph modelling approach was used for the steady state SOFC-GT model as shown in Figure 3.7. The steady state model is implemented on MATLAB-Simulink using mathematical operator blocks and functions from the Simulink library. In Figure 3.7, the blocks represent the equations solved in them and the arrows represent the transfer of variables between them. Such diagrams, in system modelling, are called “p-diagrams”, where the “p” stands for “parameter”. Table 3.1 shows the equations that are modelled in each block of the bond-graph model shown in Figure 3.7.

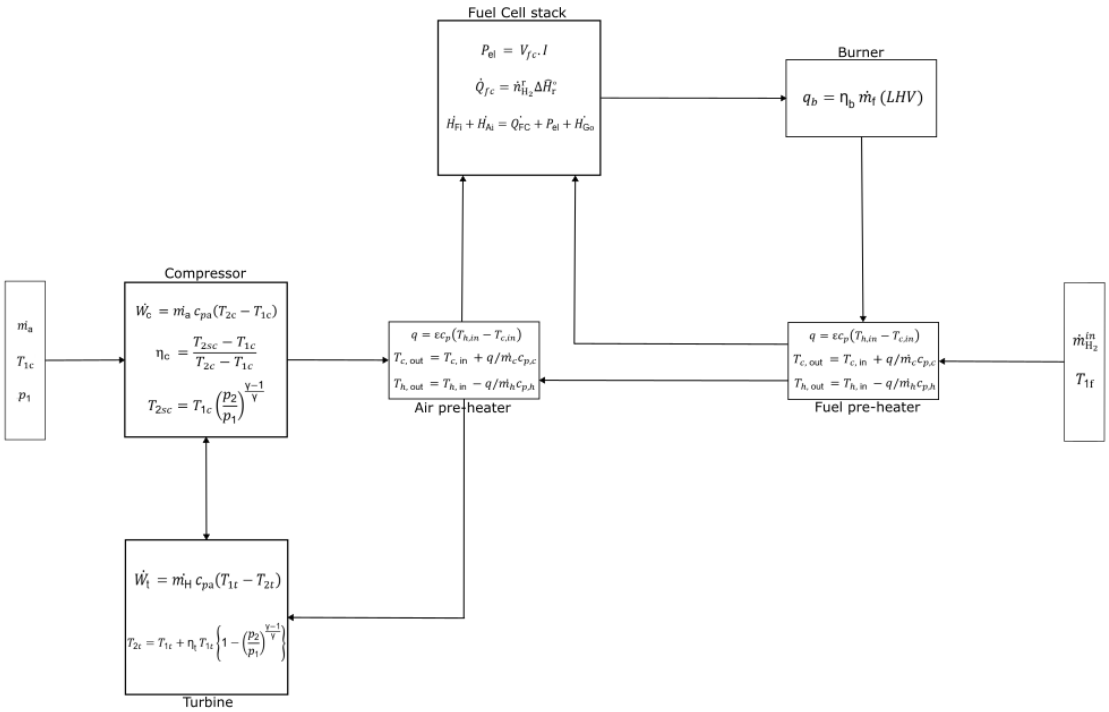


**Figure 3.7 P-diagram for SOFC-GT steady state model**

**Table 3.1 Equations modelled in p-diagram (figure 3.7)**

| Simulink block | Equations |
|---|---|
| Fuel Cell Stack | 3.2 to 3.24 |
| Compressor | 3.25 to 3.27 |
| Turbine | 3.28 to 3.30 |
| Air pre-heater | 3.31 to 3.33 |
| Fuel pre-heater | 3.31 to 3.33 |
| Burner | 3.34 and 3.35 |

The solution algorithm for this model can be represented by the flow-chart shown in Figure 3.8 and follows an iterative approach where variable values are varied until all equations in the

electrochemical, mass balance, and energy balance models are satisfied.

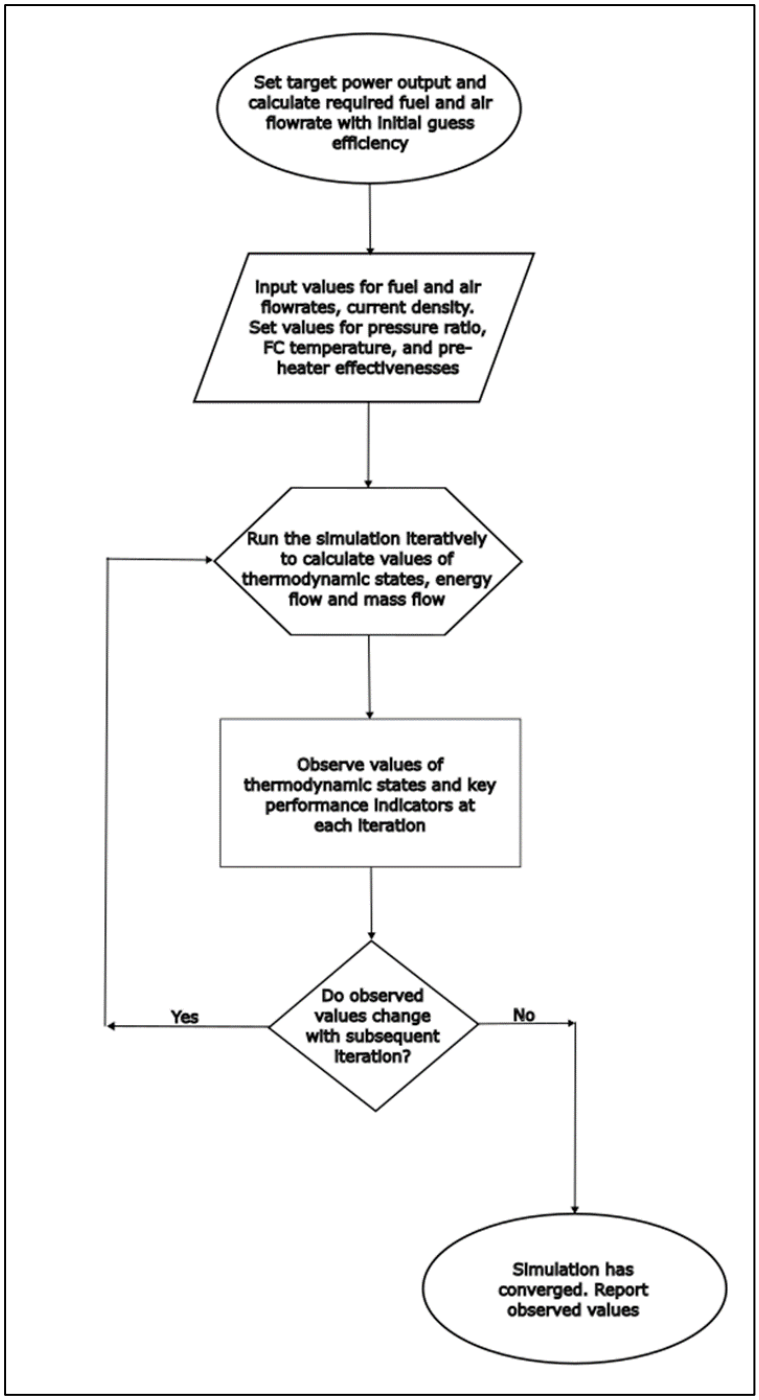


**Figure 3.8 Solution algorithm for SOFC-GT steady state model**

The algorithm depicted in the flowchart is designed to simulate the steady-state operation of the Solid Oxide Fuel Cell-Gas Turbine (SOFC-GT) system. It is structured as follows:

- Initialisation: The process begins by setting a target power output for the SOFC-GT system. An initial guess for the system efficiency is used to estimate the necessary fuel and air flow rates required to achieve the desired power output.

- Input Assignment: After initialisation, specific values for fuel and air flow rates are inputted, along with the current density. Operational parameters such as the pressure ratio, fuel cell temperature, and pre-heater effectiveness are also set at this stage. To prevent spurious solutions, it is important to provide initial values to enough input condition to constrain the system of equations and ensure there is a unique solution to them.

- Iterative Simulation: With these inputs, the simulation runs iteratively. Each iteration computes the thermodynamic states, as well as energy and mass flows within the system.

- Observation and Convergence Check: The outputs from each iteration, including the values of thermodynamic states and key performance indicators, are monitored. The simulation checks whether these observed values have changed from one iteration to the next. When there are multiple solutions to the system of equations, the solution that is most consistent with the trend observed in the variable values from initial solve to the following solves is chosen.

- Convergence Determination: If there is no significant change in observed values between successive iterations, it is determined that the simulation has converged.

- Reporting Results: Upon convergence, the algorithm concludes, and the steady-state values of the observed parameters are reported.

The iterative approach allows for refinement of the model until the output parameters stabilise, which indicates a reliable prediction of steady-state behaviour for the given input conditions.

### 3.2.2 MATLAB/Simscape

The steady state and transient models of the SOFC-GT and PEMFC systems are implemented on Matlab-Simscape. Simscape is part of the MATLAB product family and extends Simulink by providing a platform for modelling and simulating physical systems through a bond-graph approach. It allows users to create models of physical systems within the Simulink environment using physical connections, as opposed to the traditional block diagram approach. The main advantages of Simscape are as follows:

- Physical Networks: Unlike traditional Simulink models that use signals that contain only variables, Simscape uses physical connections that carry variables along with equations that define physical flow of energy and mass in mechanical, electrical, hydraulic, and thermal systems.

- Component Libraries: Simscape includes a comprehensive set of validated prebuilt components from various physical domains that can be dragged and dropped to build complex systems. These domains include mechanical translational and rotational, electrical, hydraulic, thermal, and more. Furthermore, the models were easy to modify and combine to fit the assumptions and complexities required for this project.

- Robust solvers: Simscape has pre-written solvers that were developed for solving systems of partial and ordinary differential equations and algebraic equations. The solvers also perform checks for consistency in initial condition values, bifurcation in iterative solutions, zero-crossings in solutions to equations, etc. which make them robust against spurious solutions and non-convergence.

- Equation-Based Modelling: Simscape allows creation of custom components using the Simscape language, which lets one define the mathematical equations directly. This feature facilitated the creation of a custom SOFC component based on the model defined in Section 3.1.2.

- Physical Units: Simscape automatically handles unit conversions between different components, which can significantly reduce the risk of unit-related errors models.

- Integration with MATLAB and Simulink: Simscape integrates seamlessly with MATLAB and Simulink, making it easy to incorporate Simscape models into traditional Simulink models for control design, use MATLAB code for post-processing simulation data, and utilise optimisation and other tools from MATLAB.

- Visualisation and Analysis: Simscape provides tools like the Simscape Results Explorer, which helps in visualising simulation data and analysing the transient and steady-state behaviour of systems.

For these reasons, Simscape is widely used in academia and industry for model-based design, as it enables the simulation of a system before building a prototype, thereby reducing costs and development time. This aligns well with the objectives of this project and therefore, makes it an apt tool for the dynamic simulations.

The solution algorithm in Simscape can be represented by the flowchart in Figure 3.9. It involves a structured sequence of stages, detailed below, to ensure accuracy and reliability of the simulation results.

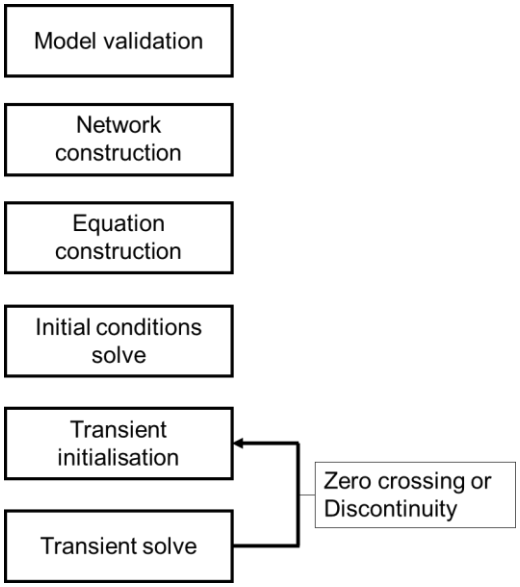


**Figure 3.9 Solution algorithm for transient models on Simscape**

Model Validation Phase: Initially, the Simscape solver confirms the model's configuration is correct and verifies the input parameters entered through the block dialog boxes and parameter scripts. This validation includes ensuring that all Simscape blocks are interconnected to form one or several physical networks. It is mandated that each distinct physical network is associated with precisely one Solver Configuration setting. Moreover, for models incorporating fluid dynamics, each unique circuit must have a corresponding block defining fluid properties for all connecting blocks. The attachment of more than one fluid block to a single loop result in an error. Additionally, compatibility between the units specified in the network links between blocks and the expected input type for the connected Simscape blocks is verified.

Network Construction Phase: Upon successful model validation, the Simscape solver constructs the physical network. This construction adheres to principles ensuring that directly connected Conserving ports share identical Across variable values (e.g., voltage, angular velocity), and Through variables (e.g., current, torque) are appropriately distributed among connected components.

Equation Construction Phase: With the network and block parameters defined, the solver formulates a system of equations. These equations categorise system variables as either dynamic, involving time derivatives and contributing to system dynamics, or algebraic, which do not involve time derivatives and are determined by conservation laws. The solver optimises this system by eliminating non-essential variables, with the remaining variables mapped to the Simulink state vector for simulation purposes.

Initial Conditions Computation Phase: The solver calculates initial conditions at the simulation

outset (time = 0), aiming to find variable values that satisfy all model equations. This phase allows for block-level variable initialisation, where users can prioritise and target initial values, influencing the computation of initial conditions. The solver prioritises satisfying high-priority targets specified in the parameterisation stage, with subsequent adjustments made to approximate low-priority targets as closely as possible.

Finding an Initial Steady State: If initiated from a steady state, the solver endeavours to find a steady-state solution under constant system inputs. This steady state is not guaranteed to reflect the anticipated conditions based on initial computations but is within acceptable tolerance levels.

Transient Initialisation Phase: Following the computation of initial conditions or after any significant event, the solver conducts transient initialisation. This phase aims to establish a consistent set of initial conditions for dynamic variables and algebraic equations, setting the stage for the transient solve phase.

Transient Solve Phase: In the final phase, the solver integrates the system of equations over time to determine variable values as functions of time. This transient solution process repeats, accommodating any system events or discontinuities until the simulation concludes.

This structured approach ensures a thorough and systematic simulation process, enhancing the reliability and accuracy of the Simscape simulations.

### 3.2.3 SOFC-GT transient model

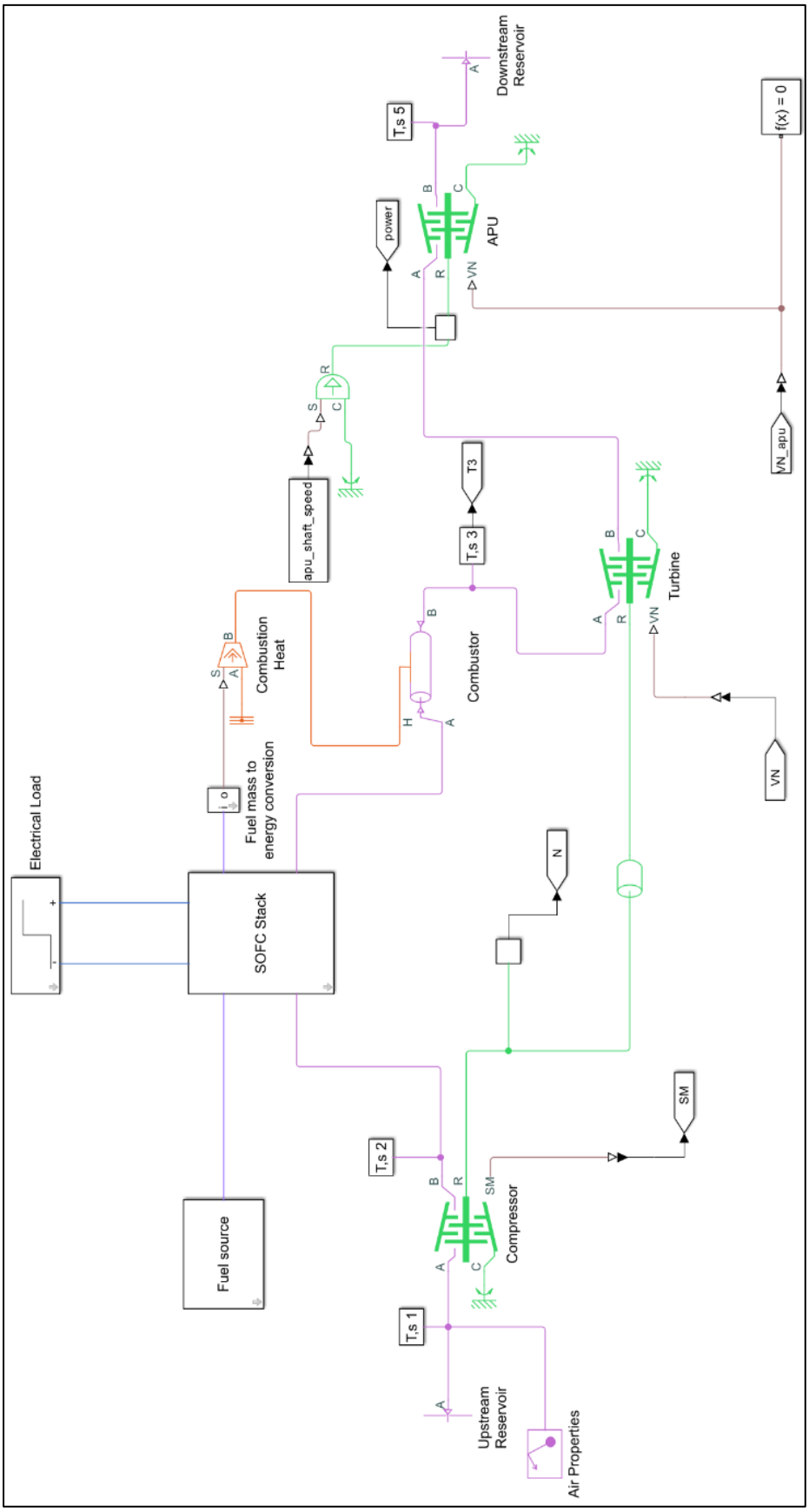


**Figure 3.10 Plant-level view of SOFC-GT Simscape model**

The transient SOFC-GT model was implemented on Matlab-Simscape and Figure 3.10 shows the plant-level view of it. It is adapted from the Brayton Cycle APU model and is the most-simplistic implementation of SOFC-GT configurations, where the fuel cell is placed between the compression and combustion processes. This configuration was chosen as the APU application where the addition of heat exchangers would make the power source too heavy for the military transport aircraft.

**Table 3.2 List of equations and maps modelled in SOFC-GT plant-level model (Figure 3.10)**

| Simscape block | Equations and maps |
|---|---|
| SOFC stack | Equations 3.2 to 3.8 and 3.36 to 3.57 |
| Compressor | Figure 3.3; Equations 3.25 to 3.27 |
| Turbine and APU | Figure 3.4; Equations 3.28 to 3.30 |
| Combustor | Equations 3.34 and 3.35 |

The SOFC stack subsystem is further divided into multiple Simscape components that contain the electrochemical, energy and mass balance models as shown in Figure 3.11 and Table 3.3.

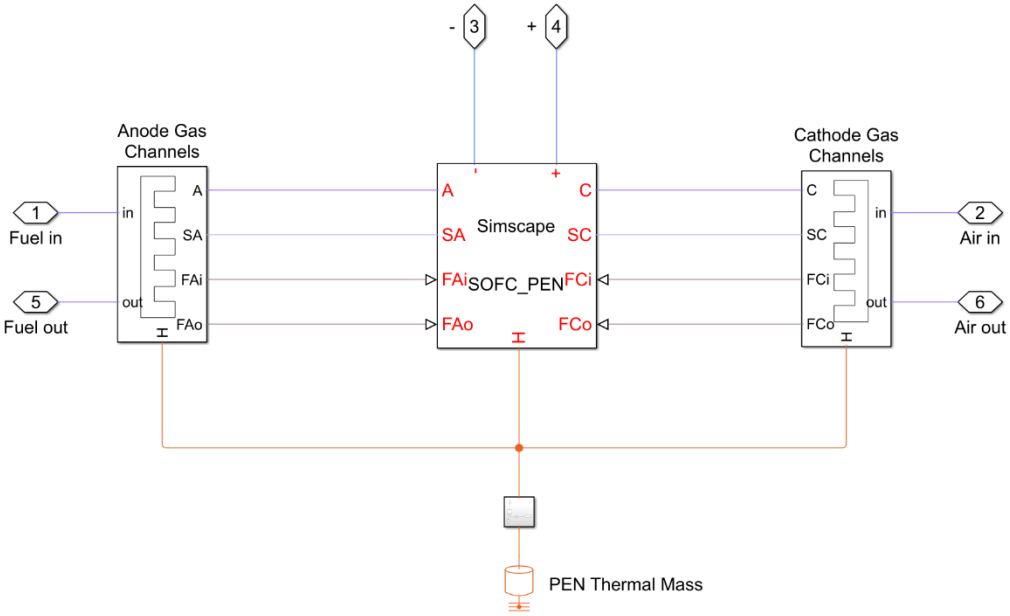


**Figure 3.11 Simscape model of SOFC stack**

**Table 3.3 Equations modelled in SOFC stack Simscape sub-system (Figure 3.11)**

| SOFC Stack sub-model | Equations |
|---|---|
| SOFC_PEN | 3.2 to 3.8; 3.53; 3.54 |
| Anode Gas Channels and Cathode Gas Channels | 3.36 to 3.43; 3.45 to 3.52; 3.56; 3.57 |
| PEN Thermal Mass | 3.44; 3.55 |

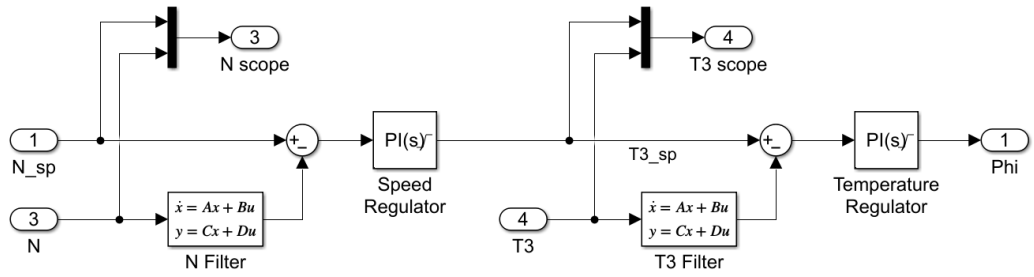


**Figure 3.12 PI Control configuration for GT speed control in SOFC-GT model**

Figure 3.12 shows the control strategy featuring two primary feedback control loops—one for the gas turbine shaft speed (N) and one for the turbine inlet temperature (T3). Both loops utilise Proportional-Integral (PI) controllers to regulate their respective process variables. Here's a breakdown of the diagram and how each part functions within the control strategy:

- **Set Points (N_sp and T3_sp):** These are the desired values for the gas turbine shaft speed and the turbine inlet temperature. These set points are what the control system is trying to achieve. N_sp is set as an input to the system model and T3_sp is the variable that is manipulated to control shaft speed N.
- **Feedback Loops:** There are two feedback loops. One is monitoring the shaft speed (N), and the other is monitoring the turbine inlet temperature (T3). The actual values of N and T3 are fed back into the system for comparison with the set points.
- **N and T3 Filters:** These filters are likely there to process the sensor signals for N and T3 to reduce noise or to condition the signal in some way (e.g., to smooth out fluctuations that might cause erratic control behaviour).
- **Differential Equations:** The blocks showing **$\dot{x} = Ax + Bu$** and **$y = Cx + Du$** represent state-space representations of the systems they are controlling. This is a mathematical model that describes the system dynamics where:
    - **$\dot{x}$** is the derivative of the state vector **x** over time, representing the system's state change.
    - **A** is the system matrix, describing the system dynamics.
    - **B** is the input matrix, how the input **u** (control effort) affects the system's state.
    - **C** is the output matrix, which maps the state vector to the output **y**.
    - **D** is the direct transmission matrix, which maps the input **u** directly to the output **y**.
- **PI Controllers:** There are two PI controllers in this strategy. A PI controller combines two modes of control: Proportional and Integral. The Proportional part depends on the current error (the difference between the set point and the actual value), and the Integral part depends on the sum of past errors. The PI controller for the shaft speed

will generate a control signal to try to keep the speed at N_sp, and the PI controller for the temperature will do the same for keeping the turbine inlet temperature at T3_sp.

- **Speed Regulator and Temperature Regulator:** These are the actual control mechanisms that affect the gas turbine. The speed regulator might control the fuel flow or some other aspect of the turbine to adjust the speed, while the temperature regulator might adjust cooling or heating elements or the mixture of the fuel and air to control the temperature.
- **Scopes (N scope and T3 scope):** These are outputs for monitoring purposes.

### 3.2.4 Turbocharged PEMFC model

The PEMFC system model was also implemented on Simscape and is shown in Figure 3.13. Table 3.4 lists out the equations and maps modelled in the customised Simscape blocks.

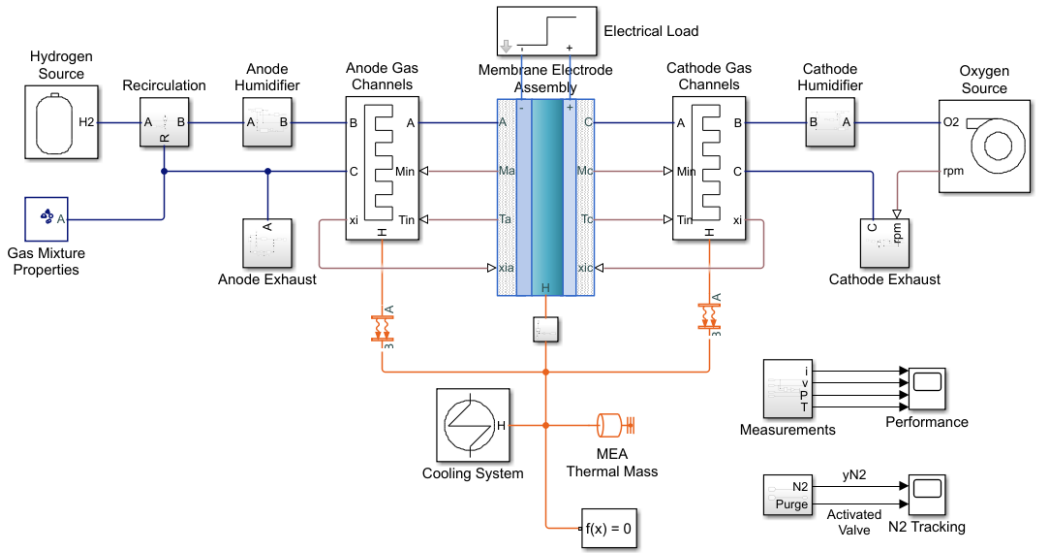


**Figure 3.13 Plant-level view of PEMFC system Simscape model**

**Table 3.4 List of equations and maps modelled in PEMFC plant-level model**

| Simscape block | Equations and maps |
|---|---|
| Membrane Electrode Assembly | Equations 3.58 to 3.62; 3.72; 3.73 |
| Anode and Cathode Gas Channels | Equations 3.63 to 3.70; 3.74; 3.75 |
| Anode and Cathode humidifiers | Equations 3.76 to 3.79 |
| MEA Thermal Mass | Equation 3.71 |
| Oxygen source | Figure 3.5; Equations 3.25 to 3.27 |
| Cathode Exhaust | Figure 3.6; Equations 3.28 to 3.30 |
| Anode and Cathode Humidifiers | Equation 3.61 |

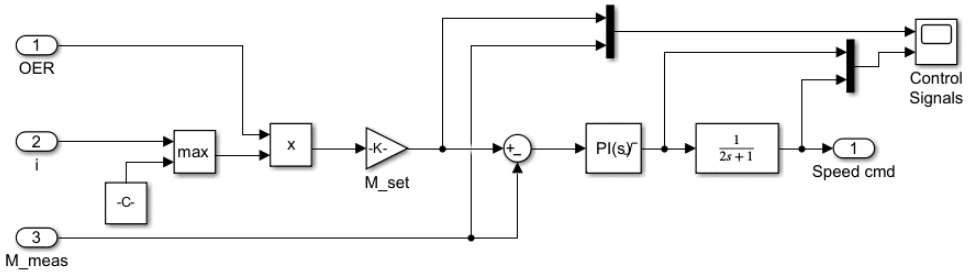


**Figure 3.14 PI Control configuration for compressor speed control in PEMFC model**

Figure 3.14 shows the compressor-turbine speed control system housed within the Oxygen Source. This sub-model controls the speed of the compressor and turbine to match the oxygen flow-rate required to meet power demand while maintaining a constant temperature in the fuel cell stack. A description of the figure is given below:

- **OER (Oxygen-Excess Ratio):** This input indicates the ratio of excess oxygen available for the reaction in the PEMFC, beyond what is needed for the stoichiometric reaction to maintain constant stack temperature.
- **Current (i):** The electrical current is crucial because it is indicative of the power output and efficiency of the PEMFC. It can impact the required mass flow rate of the compressor to supply the necessary oxygen.
- **M_meas (Measured Mass Flow Rate):** This is the actual measurement of the mass flow rate of the compressor. It provides real-time feedback for the control system to adjust the mass flow rate to the desired level.
- **M_set (Mass Flow Rate Set Point):** This is the target mass flow rate for the compressor, adjusted by the scaled current signal.
- **PI Controller:** The Proportional-Integral controller processes the difference between the actual mass flow rate (M_meas) and the set point (M_set) to produce a control signal that aims to minimise the error by altering the mass flow rate.
- **Transfer Function (1/(2s+1)):** This block represents a first-order lag that is used to model the response of the actuator controlling the mass flow or the dynamics of the mass flow system itself.
- **Speed Command (Speed cmd):** This output, labelled 'Speed cmd', is the control signal to control the speed of the compressor (signal “rpm” in Figure 3.13) to adjust the flow rate.
- **Control Signals:** These outputs are for monitoring system performance by the user.

## *3.3 Steady state models and Monte Carlo simulation*

The Monte Carlo simulation is a computational technique designed to approximate the outcomes of complex systems or processes by executing random sampling from input probability distributions. This method is particularly effective for addressing problems characterised by uncertainty or variability. The name "Monte Carlo simulation" is inspired by the Monte Carlo Casino, renowned for its association with randomness and games of chance. The workflow of a Monte Carlo simulation can be summarised as follows [78], [79], [80], [81], [82]:

- **Identification of Input Parameters and Their Distributions**: The first step involves recognising the input parameters critical to the system or process under study. Each of these parameters is then assigned a probability distribution (e.g., normal, uniform, exponential) to reflect its inherent uncertainty.
- **Random Sampling**: The next phase entails generating random values for each input parameter based on its assigned probability distribution. These values simulate potential scenarios or states of the system.
- **Model Evaluation**: The simulated random input values are utilised as inputs for the model or simulation. This step involves running the model or simulation to derive corresponding output values.
- **Statistical Analysis**: After multiple iterations of the model, the output values are aggregated for statistical analysis. This analysis aims to estimate the output distribution and extract meaningful statistics such as mean, variance, and confidence intervals.
- **Inference**: Utilising the statistical insights obtained, inferences about the system's behaviour are drawn. These might encompass estimating the probability of specific outcomes, evaluating risks, or making decisions based on the simulation outcomes.

Monte Carlo simulations find extensive application across various domains such as finance, engineering, physics, and more, aiding in problem-solving that involves uncertainty, variability, or complexity. This technique serves as a vital tool in decision-making and risk assessment processes.

Since the study of SOFC-GT system design involves sampling values and using combinations of those values for multiple parameters with differing probability distributions, the Monte Carlo method was used to ensure that all possible combinations were covered with enough resolution and uncertainties were minimised. It also ensured that sensible limits were used in the sampling of parameter values. This combines the deterministic nature of steady-state models with the stochastic approach of Monte Carlo simulation. This hybrid method is particularly beneficial for systems like SOFC-GT systems, where inputs exhibit variability or uncertainty, by evaluating a spectrum of scenarios to identify robust design solutions [83], [84], [85]. The range of values used for the parameters and the probability distributions used in their sampling are presented in Table 4.6 in Section 4.3.1 of this report.

The SOFC-GT steady state model was used to run Monte-Carlo simulations to study the effects of operating variables and design parameters in this project. The studies and their results are presented in more detail in Chapter 4.

## *3.4 Transient modelling and Model-in-the-Loop simulation*

Fuel cells and gas turbines are integral components of contemporary energy systems, offering high-efficiency power generation and reduced environmental footprint. However, their performance markedly depends on operational conditions, necessitating an in-depth understanding of system responses to varying loads. This project used Model-in-the-Loop (MiL) simulations as an approach for modelling and analysing these systems under diverse conditions. MiL simulation integrates computational models of physical systems into a simulation loop, facilitating real-time analysis of interactions between the system (often referred to as the "plant" model) and its control algorithms. This methodology allows for the iterative testing and refinement of control strategies and identifying optimum operating windows in a simulated environment prior to physical implementation, significantly reducing development costs and time.

**Applications and benefits [15], [37], [40], [86]:**
Control Strategy Development: By simulating transient states within MiL environments, engineers can evaluate and fine-tune control algorithms, ensuring their effectiveness and reliability under dynamic conditions. This iterative process accelerates the development of advanced control strategies that enhance system performance and stability.

Performance Assessment and optimisation: Transient modelling and MiL simulation provide a framework for assessing system performance under various operational conditions. This capability is essential for identifying and mitigating potential performance issues, optimising control parameters, and achieving desired performance metrics such as efficiency and fuel consumption.

Stability Analysis: The dynamic models used in transient system modelling offer insights into system stability during transitional states. MiL simulations further enable the testing of control strategies against stability boundaries, ensuring the development of control systems capable of maintaining stability across a range of operational scenarios.

By combining transient system modelling and Model-in-the-Loop simulation, the SOFC-GT and PEMFC system models described in Sections 3.1. and 3.2 were used to simulate the systems under varying load conditions to demonstrate the applications of these models. Chapter 5 details the SOFC-GT simulations in detail and the PEMFC simulations are detailed in Chapter 6.

# 4 SOFC-GT steady state modelling

This chapter describes the application of steady state models of a Solid Oxide Fuel Cell stack and the balance of plant fuelled by hydrogen. As mentioned in Section 1.4.2, the model was required to simulate steady state performance of such a system with little to or experimental data, as it is to be used in the earliest stages of product development where such data is not available. Chapter 3 described the equations and implementation of the steady state models and in this one, they are deployed in a couple of example applications to demonstrate how they can be used in design studies and analytical systems engineering at early stages of a project to answer important questions about operating parameters and component sizing.

The first section of this chapter presents the validation work that was done on the steady state model of the SOFC stack. That is then followed by two design study applications of the model:

- Identification of optimum current density for maximum electrical efficiency.
- Sensitivity study of system efficiency to design parameters.

## *4.1 Model validation*

The first step in experimentation using models is validation. Validation is an important process where the results of the model are checked for agreement with test data or results from higher-fidelity models to assess its accuracy. For the SOFC steady state model, this was done by performing two tests:

1) A sweep of current density values from zero to limiting current density for a given fuel flowrate to obtain a polarisation curve (V-I curve) to validate the electrochemical sub-model
2) Simulation of steady-state conditions set by the IEA benchmark [87] for SOFCs to validate the interaction of energy balance and mass balance models with the electrochemical model

### 4.1.1 Validation of electrochemical sub-model

The electrochemical model described in Section 3.2.1 is the main component of the stack model as it describes the fuel cell's principal feature of energy conversion from chemical to electrical.

To validate this model, the SOFC model was run at current density values between 0 A/cm$^2$ and 1.0 A/cm$^2$ for a constant fuel flowrate and constant temperature. The fuel flowrate was set such that the corresponding fuel utilisation ratio for 0 A/cm$^2$ to 1 A/cm$^2$ ranges from 0 to 1.0, i.e., from zero $H_2$ consumption in the first simulation setpoint to consuming all the $H_2$ passed through the cell at the final one, meaning no more current can be drawn from the cell beyond that point. Power density and cell voltage were plotted against current density to produce the polarisation curve and this curve was compared against experimental polarisation curves from

literature to determine the model's correlation to actual cell behaviour. Boundary conditions applied to the model for this validation study are presented in Table 4.1.

**Table 4.1 Parameter and input values used in validation study**

| **Cell parameters** | **Value** |
|---|---|
| Number of cells ($N_c$) | 1 |
| Electrochemical area ($A_c$) | 100 $cm^2$ |
| Limiting current density ($I_L$) | 1 $A/cm^2$ |
| Ohmic resistance $r_0$ at $T_0$ = 573 K | 0.126 Ω |
| Charge transfer coefficient ($a$) | 0.5 |
| Exchange current density ($I_0$) | 0.005 $A/cm^2$ |
| **Input parameters** | |
| Fuel consumption rate | 0 mg/s to 1 mg/s |
| System pressure | 1 bar |
| Current | 0 A to 100 A |
| Cell Temperature | 923 K |

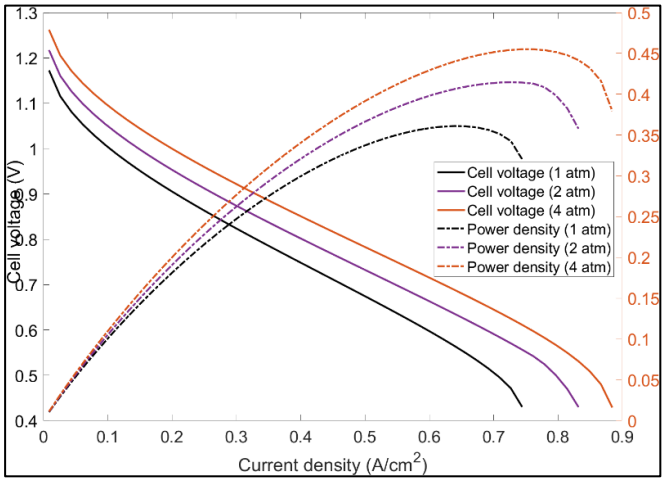


**Figure 4.1 Model-predicted polarisation curve**

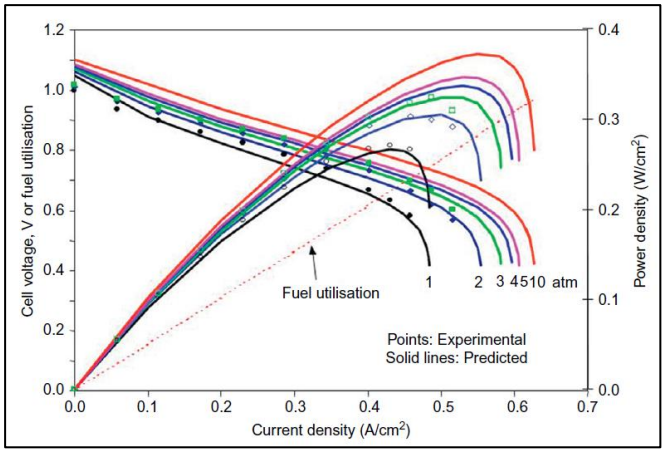


**Figure 4.2 Typical polarisation curves for SOFC [23]**

The model-generated Voltage – Current curve shown in Figure 4.1 can be split into three regions:

- Non-linear region 1, at low current density/fuel utilisation factor where activation loss is the predominant polarisation loss.
- Linear region, usually the operating window of current density/fuel utilisation factor where ohmic loss is the predominant polarisation loss.
- Non-linear region 2, at high current density/fuel utilisation factor where concentration loss is the predominant polarisation loss.

Slope of the polarisation curve (ΔV/I) gives the area-specific resistance (ASR) of a given cell. The model-calculated value for ASR in the ohmic region of the curve, i.e., the linear region in Figure 4.1 is 0.66 $\Omega cm^2$ at 1 atm, 0.62 $\Omega cm^2$ at 2 atm, and 0.59 $\Omega cm^2$ at 4 atm, which is consistent with values and the decreasing trend in ASR with increasing temperature reported in literature [9], [23]. Figure 4.1 also shows good correlation in shape to typical polarisation curves of SOFCs obtained from literature as seen in Figure 4.2 which shows polarisation curves for a typical SOFC operating at 923 K at various pressures, hence validating the electrochemical sub-model of the steady-state SOFC.

### 4.1.2 Validation of thermal sub-model

The International Energy Agency (IEA) conducted a "Programme of Advanced Fuel Cells" between 1993 and 1995 which involved the development of two benchmark cases for SOFC modelling. The first benchmark case was for a single cell fuelled with hydrogen and the second for methane. These benchmark cases were drawn up by leading researchers from five European countries and has been widely considered as a reliable reference for SOFC modelling ever since [87], [88], [89], [90].

To validate the thermal sub-model of the steady state SOFC model, it was run at the same boundary conditions as the IEA benchmark for SOFCs and its results compared to those of the IEA. Besides the reliance placed on this data by many researchers in the past, the fact that the IEA benchmark cases used a similar lumped approach to modelling fuel and air flow as well as the thermal mass of the cells makes it a suitable reference for validation of the flow and thermal sub-models used in this project [87].

**Table 4.2 Operating conditions for IEA Benchmark case [87], [90]**

| | |
|---|---|
| System pressure | 1 bar |
| Air and fuel inlet temperature | 1173 K |
| Air utilisation factor | 0.141 |
| Fuel utilisation factor | 0.85 |
| Current density | 0.3 A/cm$^2$ |
| Inlet fuel composition (mole fraction) | 0.10 $H_2O$; 0.90 $H_2$ |
| Inlet air composition (mole fraction) | 0.21 $O_2$; 0.79 $N_2$ |

The steady state model was run with the boundary conditions of the IEA benchmark case and the model-predicted values for cell temperature, voltage, fuel, and air temperatures. The boundary conditions are listed in Table 4.2 and the comparison of model-predicted results with the benchmark case is presented in Table 4.3.

**Table 4.3 Comparison of model-calculated results against reference values**

| | IEA Reference value [87] | Model-calculated value | Error |
|---|---|---|---|
| Cell temperature | 1293.3 K | 1268.1 K | 1.95 % |
| Vcell | 0.703 V | 0.706 V | -0.43 % |
| Fuel temperature | 1321 K | 1338 K | 17 K |
| Air temperature | 1322 K | 1335 K | 13 K |

As seen from Table 4.3, the SOFC model used in this study is within 2% accuracy of the reference data for Cell Temperature prediction and within 0.5%. The stream temperature predictions are within 20 K of the reference data.

## *4.2 Identification of ideal current density*

### 4.2.1 Introduction to analysis

Identifying an optimum current density range is crucial for the efficiency and durability of a SOFC-GT hybrid system. The SOFC-GT system combines the high-temperature operation of solid oxide fuel cells (SOFC) with a gas turbine, harnessing the electrical and thermal energy produced by the SOFC to drive the turbine, thereby increasing overall system efficiency. The importance of determining an optimum current density range lies in several key aspects:

Cell resistance/efficiency optimisation: The current density in an SOFC directly impacts the electrochemical efficiency of the system. At optimal current densities, indicated by the linear region of the polarisation curve, the resistance of the cell is lowest and hence overpotential losses are at their lowest. It is important to set the operating point of the system within this range in order to maximise efficiency of the fuel cell itself, and hence the system.

Thermal Management: SOFCs operate at high temperatures (typically 800°C to 1000°C). The current density affects the heat generation within the cell – the greater the current, the greater the heat generated from cell – which in turn impacts the thermal management of the system. Operating within an optimal current density range ensures that the system can maintain a stable operating temperature, which is crucial for the longevity and stability of the SOFC and the efficiency of the gas turbine.

Durability and Longevity: High current densities can lead to accelerated degradation of the SOFC components due to increased thermal stresses and the potential for chemical degradation mechanisms such as oxidation or volatilisation of cell materials. By identifying and operating within an optimum current density range, the degradation rate can be minimised, thereby extending the life of the SOFC and reducing maintenance and replacement costs [91].

Economic Considerations: The operational efficiency and durability of SOFC-GT systems have significant economic implications. By optimising the current density, the system can achieve higher electrical efficiency, reducing fuel consumption and operating costs. Furthermore, enhanced durability reduces the need for frequent replacements or repairs, lowering the total cost of ownership.

Environmental Impact: Efficient operation of SOFC-GT systems at an optimal current density contributes to reduced emissions of greenhouse gases and pollutants. By maximising the conversion of fuel to electricity, less fuel is wasted, leading to lower emissions of $CO_2$, $NO_x$, and other harmful substances.

In summary, higher current densities and temperatures are good for maximising theoretical

efficiency and energy conversion but the increased thermal stresses caused due to higher temperature differences across the stack channels and between the streams and cells, lead to increased degradation. This means that a balance has to be found between the two.

To identify the optimum current density, the system model was run at a range of current density values and the corresponding model outputs recorded: temperature difference between the cell and streams, cell voltage, and electrical efficiency of the system.

Parameters and inputs applied to the model are listed in Table 4.4.

**Table 4.4 Operating parameters of SOFC-GT model for current density study**

| Parameter | Value |
|---|---|
| Number of cells | 360 |
| Electrochemical area | 650 $cm^2$ |
| Limiting current density ($I_L$) | 1 $A/cm^2$ |
| Ohmic resistance $r_0$ at $T_0$ = 573 K | 0.126 Ω |
| Charge transfer coefficient ($a$) | 0.5 |
| Exchange current density ($I_0$) | 0.005 $A/cm^2$ |
| Current density | 0.1 $A/cm^2$ to 0.8 $A/cm^2$ |
| Air flow-rate | 0.50 kg/s |
| Fuel flow-rate | 0.003 kg/s |
| Pressure ratio | 3 |

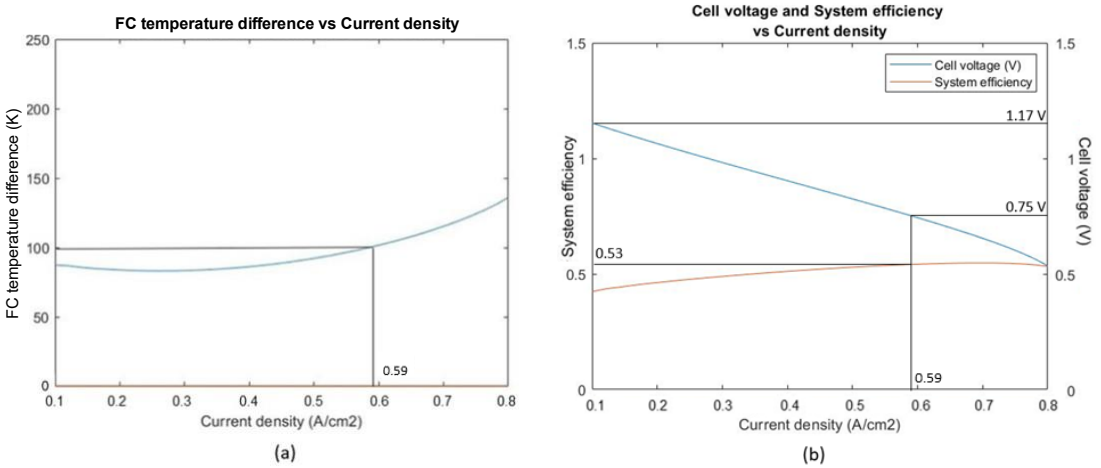


**Figure 4.3 Results from current density sweep**

Keeping all other parameters constant, current density of the fuel cell was varied from 0.1 to 0.8 $A/cm^2$, where the polarisation curve is in its linear region. As seen from Figure 4.3 (a), the temperature difference between cell temperature and the lower of the two stream temperatures rises above 100 K at current densities above 0.59 $A/cm^2$. When this temperature difference exceeds 100 K, thermal stresses in the stack exceed acceptable limits [28], [29], [30] and

therefore, points to non-optimum operation of the stack.

Therefore, the desired operating range for the fuel cell – where the fuel cell is in linear region of polarisation curve and temperature difference is within acceptable limits – was found to be between current density 0.1 A/cm$^2$ and 0.59 A/cm$^2$. As shown by Figure 4.3 (b), the corresponding cell voltage range is between 1.17 V and 0.75 V. Electrical efficiency of the system was found to peak at around 53% at 0.59 A/cm$^2$ and plateau at that value even at higher current densities. This can be attributed to the larger polarisation losses at higher current densities resulting in more energy wastage in the form of heat.

## *4.3 Monte-Carlo simulations*

### 4.3.1 Introduction to analyses

The literature review conducted as part of this study underscores the suitability of Solid Oxide Fuel Cell-Gas Turbine (SOFC-GT) systems for transport applications, particularly where gross system electrical efficiency emerges as the pivotal performance metric. In light of this finding, it becomes apparent that the primary objective in the system design process, especially when integrating an SOFC with a Brayton Cycle, should be the maximisation of efficiency. To elucidate the relationship between gross electrical efficiency and various system design parameters, a steady-state model was employed to carry out Monte Carlo simulations. The analysis focused on identifying how gross electrical efficiency correlates with selected design parameters, namely GT Pressure Ratio, Fuel Cell Temperature, and Heat Exchanger effectiveness. This methodological approach allows for a comprehensive understanding of the impact of these parameters on system performance, guiding towards more efficient SOFC-GT system designs.

Higher pressure ratio leads to increase in partial pressure of $O_2$ on the cathode side [9]. This increases the Nernst Potential ($E_n$) of the fuel cell according to the relationship Equation 4.1.

**Equation 4.1**

$$E_n \propto \ln\left(pO_2{}^{0.5}\right)$$

The higher the pressure, the lower the electrode overpotential which reduces polarisation losses and increases efficiency.
Higher pressure ratio also leads to higher thermal efficiency of the Brayton cycle as shown by Equation 4.2 for an ideal reversible Brayton cycle [92].

**Equation 4.2**

$$\eta_{th} = 1 - \frac{1}{PR^{\kappa-1/\kappa}}$$

Higher pressure ratio, however, comes with a penalty in power density of the system because the higher the design pressure ratio, the larger the size and mass of gas turbine components. Therefore, it is important to optimise the balance between pressure ratio and component mass while designing an SOFC-GT system.

Increase in fuel cell temperature ($T_{fc}$) increases ionic conductivity ($\sigma$) of the cell and reduces overpotential losses roughly according to Equation 4.3 [23]. This leads to a decrease in polarisation losses in the cell when current is drawn.

**Equation 4.3**

$$\sigma \propto e^{(-\frac{1}{T_{fc}})}$$

Higher $T_{fc}$ leads to a higher temperature and hence enthalpy of gases leaving the fuel cell and going into the turbine inlet. This increases the Carnot efficiency of the Brayton cycle [67] according to Equation 4.4.

**Equation 4.4**

$$\eta_{carnot} = 1 - \frac{T_{ambient}}{T_{turbine\ inlet}}$$

Pre-heater effectiveness: Effectiveness of a heat exchanger is defined as the ratio of actual heat energy transferred to maximum heat energy that can be transferred between the two fluid streams. All other variables being constant, the larger the heat transfer area, the greater the effectiveness of the heat exchanger. Therefore, increasing the pre-heaters' effectiveness will increase the mass of the system and lower power density. For this reason, pre-heater effectiveness values were also chosen for the sensitivity analysis.

The second design study done with the steady state system model was a sensitivity study of electrical efficiency to a set of design parameters. As explained in Section 3.5.3, the parameters chosen for the study are pressure ratio of gas turbine, operating temperature of the fuel cell, and effectiveness of the air and fuel pre-heater heat exchangers.

**Table 4.5 Operating parameters of SOFC-GT model for Monte-Carlo simulations**

| Specification | Value |
|---|---|
| Number of cells | 360 |
| Electrochemical area | 650 $cm^2$ |
| Limiting current density ($I_L$) | 1 $A/cm^2$ |
| Ohmic resistance $r_0$ at $T_0$ = 573 K | 0.126 Ω |
| Exchange current density ($I_0$) | 0.005 $A/cm^2$ |
| Charge transfer coefficient | 0.5 |
| Ohmic resistance coefficient | -2870 |
| Current density | 0.6 $A/cm^2$ |
| Air flow-rate | 0.50 kg/s |
| Fuel flow-rate | 0.003 kg/s |
| SOFC fuel utilisation | 0.50 |

The model was run with the boundary conditions listed in Table 4.5, at 100 datasets for the parameter values within the limits listed in Table 4.6. These limits were set based on good engineering sense and lessons learnt from the literature review. Ohmic resistance coefficient (α in Equation 3.6) is negative because the ohmic resistance of the SOFC electrolyte decreases with increasing temperature.

**Table 4.6 Parameter limits for Monte-Carlo simulations**

| Parameter | Lower limit | Higher limit | Probability distribution |
|---|---|---|---|
| GT pressure ratio | 2 | 7 | Uniform |
| Fuel cell temperature | 873 K | 1273 K | Exponential (decreasing) |
| Fuel pre-heater effectiveness | 0.10 | 0.85 | Normal |
| Air pre-heater effectiveness | 0.10 | 0.85 | Normal |

The pressure ratio values were uniformly distributed as turbomachinery with these rate pressure ratios are very common but the sample was capped at 7 because previous studies have shown that the efficiency gain with pressure becomes smaller and smaller with greater pressures and above 7 bar [11], [93], the cost associated with turbomachinery required to achieve those pressures outweigh the efficiency gain. Fuel cell temperature values are set between 873 K and 1273 K from the nominal operating temperatures of SOFCs reviewed in literature, with an exponential distribution as there are more SOFCs in market in the lower operating temperature range than the highest [16], [23]. The upper limit is set at 1273 K also because higher fuel cell temperatures increase turbine inlet temperature and gas turbine efficiency reduces with higher turbine inlet temperatures. Heat exchanger effectiveness values are set between 0.10 and 0.85 with a normal distribution based on a review of values used in previous literature and commercially available specification sheets which show a similar range

and more examples in the 0.4 to 0.6 range than the extremes [74].

### 4.3.2 Parameter sweeps

The model was then run by iterating each parameter from its minimum to maximum value in "sweeps" while keeping the other design parameters constant. Electrical efficiency for each sweep was recorded and plotted against the parameter. An equation was then fit to each curve. These equations define the relationship between the given parameter and electrical efficiency of the system within the limits defined in Table 4.6.

The criteria for considering a polynomial equation to be a "good fit" was a Root Mean Squared Error (RMSE) lower than 0.001 and a coefficient of determination (R-squared) greater than 0.99. The lowest order polynomial equation that meets these criteria was chosen for each parameter to minimise the complexity and computational effort of solving these equations as part of a wider parametric design study. Higher order equations also tend to overfit the equation to the range of values used in sample data, so the lower order equations were preferred.

*Pressure ratio sweep*

The pressure ratio sweep was done for values between 2 and 7 with stack temperature T at 973 K; and heat exchanger effectiveness at 0.65.

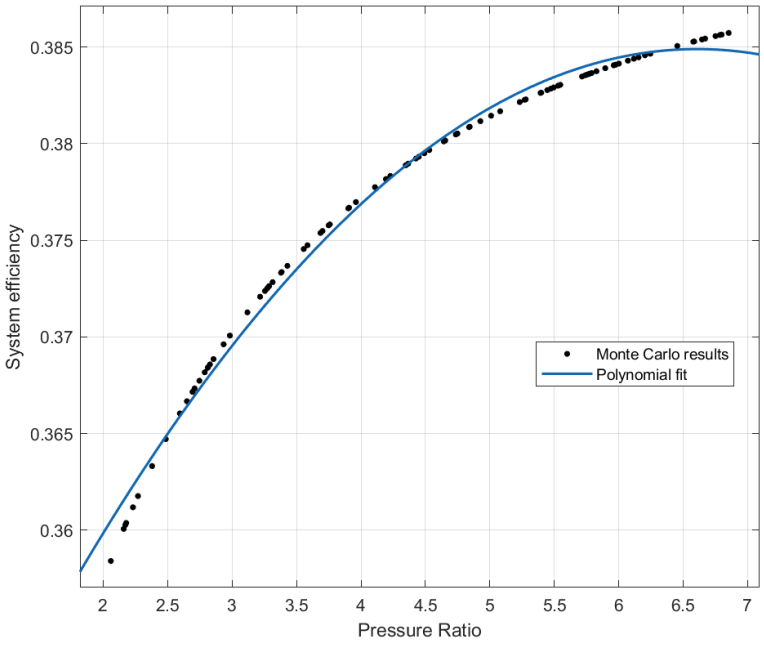


**Figure 4.4 Monte-Carlo scatter plot and fitted curve for Pressure Ratio**

Figure 4.4 shows the System electrical efficiency ($\eta$) vs Pressure Ratio ($\pi$) curve. Electrical efficiency increases from nearly 35.5% at $\pi$ = 2 to 38.5% at $\pi$ = 7. By fitting a second order polynomial equation to this curve, electrical efficiency ($\eta$) can be defined as a function of pressure ratio ($\pi$) by the Equation 4.5.

**Equation 4.5**

$$\eta(\pi) = p1 \cdot \pi^2 + p2 \cdot \pi + p3$$

Values of the coefficients p1, p2, and p3 depend on the operating window of the system. For a system operating at parameter values used in this specific experiment, the coefficients are:

- $p1 = -0.001179$ (with a 95% confidence interval between $-0.0012$ and $-0.0011$)
- $p2 = 0.01559$ (with a 95% confidence interval between 0.01497 and 0.01621)
- $p3 = 0.3334$ (with a 95% confidence interval between 0.3321 and 0.3347)

Substituting the given coefficients into the Equation 4.5, we get:

$$\eta(\pi) = -0.001179 \cdot \pi^2 + 0.01559 \cdot \pi + 0.3334$$

Goodness of fit for this equation in the range of pressure ratios between 2 and 7:

- Sum of Squares Error (SSE): 3.526e-05
- R-square: 0.9935
- Adjusted R-square: 0.9934
- Root Mean Squared Error (RMSE): 0.0006029

*Stack Temperature sweep*

The stack temperature sweep was done for values between 873 K and 1273 K with pressure ratio π at 4; and heat exchanger effectiveness at 0.65.

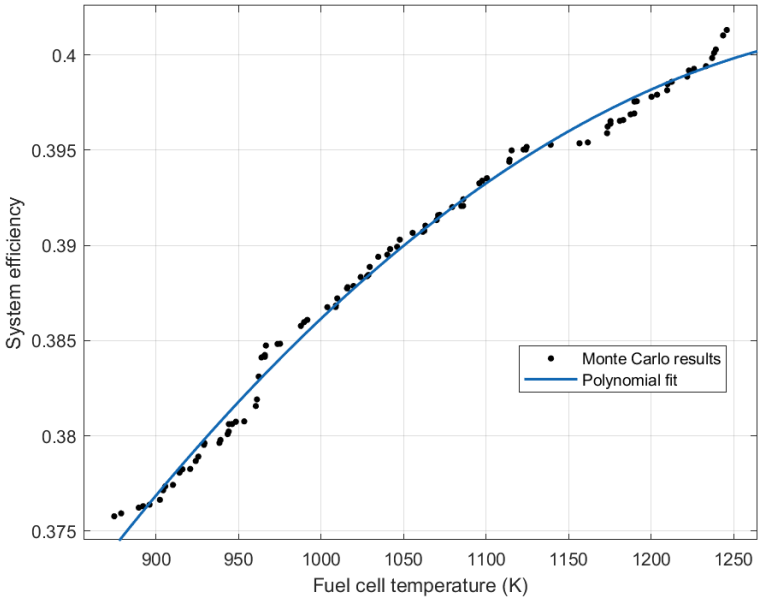


**Figure 4.5 Monte-Carlo scatter plot and fitted curve for Fuel Cell Stack temperature**

Figure 4.5 shows the System electrical efficiency ($\eta$) vs Stack temperature ($T$) curve. Electrical efficiency increases from nearly 37.5% at $T$ = 873 K to around 40% at $T$ = 1273 K. By fitting a second order polynomial equation to this curve, electrical efficiency ($\eta$) can be defined as a function of stack temperature (T) by Equation 4.6.

**Equation 4.6**

$$\eta(T) = p1 \cdot T^2 + p2 \cdot T + p3$$

For a system operating at parameter values used in this specific experiment, the coefficients are:

- $p1 = -1.092 \times 10^{-7}$ (with a $95\%$ confidence interval between $-1.219 \times 10^{-7}$ and $-9.644 \times 10^{-8}$ )
- $p2 = 0.0003003$ (with a $95\%$ confidence interval between 0.0002732 and 0.0003274)
- $p3 = 0.195$ (with a $95\%$ confidence interval between 0.1807 and 0.2093)

Equation 4.6 becomes:

$$\eta(T) = \left(-1.092 \times 10^{\{-7\}}\right)T^2 + (0.0003003)T + 0.195$$

Goodness of fit for this equation in the range of Stack temperatures between 873 K and 1273 K are as follows:

- SSE: 4.279e-05
- R-square: 0.9924
- Adjusted R-square: 0.9922
- RMSE: 0.0006642

There is an apparent mismatch between the model results and polynomial fit at the lower and higher extremes of the temperature range. However, the fit still meets the R-squared and RMSE criteria for being considered good and the temperature range covers the entire operating range of SOFCs. The differences between the model-predicted values and polynomial fit values of system efficiency are also less than 0.2% which is negligible.

*Heat exchanger effectiveness sweep*

The heat exchanger effectiveness (ε) sweep was done for values between 0.10 and 0.85 for both air and fuel pre-heaters with pressure ratio π at 4; and stack temperature at 973 K.

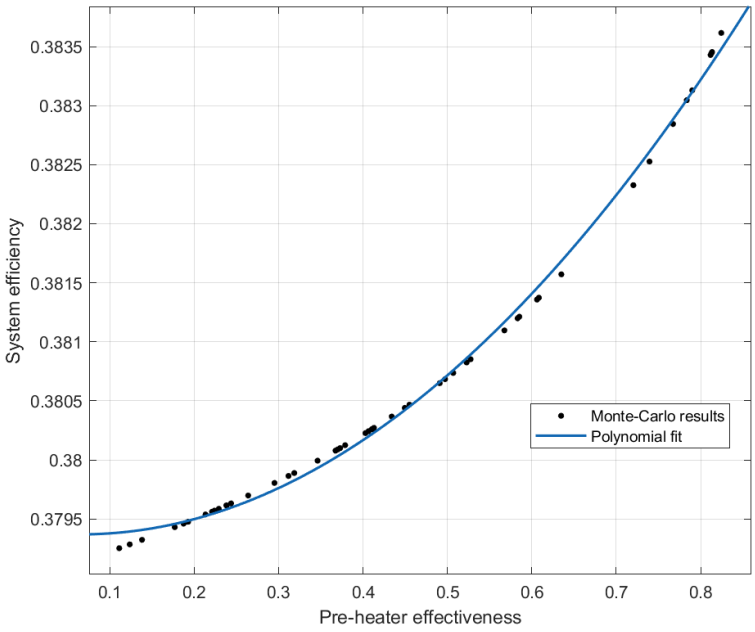


**Figure 4.6 Monte-Carlo scatter plot and fitted curve for Pre-heater effectiveness**

Figure 4.6 shows the System electrical efficiency ($\eta$) vs Heat exchanger effectiveness ($\varepsilon$) curve. Electrical efficiency increases from nearly 37.9% at $\varepsilon$ = 0.10 to around 38.4% at $\varepsilon$ = 0.85. By fitting a second order polynomial equation to this curve, electrical efficiency ($\eta$) can be defined as a function of pre-heater effectiveness ($\varepsilon$) by Equation 4.7:

**Equation 4.7**

$$\eta(\varepsilon) = p1 \cdot \varepsilon^2 + p2 \cdot \varepsilon + p3$$

For a system operating at parameter values used in this specific experiment, the coefficients with their $95\%$ confidence bounds are as follows:

- $p1$ is 0.007142 , with a confidence interval between 0.006693 and 0.00759 .
- $p2$ is -0.0009384 , with a confidence interval between -0.001377 and -0.0004999 .
- $p3$ is 0.3794 , with a confidence interval between 0.3793 and 0.3795 .

Substituting the provided coefficients into Equation 4.7, we get:

$$\eta(\varepsilon) = 0.007142 \cdot \varepsilon^2 - 0.0009384 \cdot \varepsilon + 0.3794$$

Goodness of fit:

- SSE: 2.045e-07
- R-square: 0.9975
- Adjusted R-square: 0.9974
- RMSE: 6.597e-05

To summarise, Equations 4.5 to 4.7 represent the relationship between SOFC-GT system

efficiency and the chosen design parameters of GT pressure ratio, Fuel Cell temperature, and Heat Exchanger effectiveness within the range of parameter values defined in Table 4.6 for the Fuel Cell size and operating parameters defined in Table 4.5. These equations can be used in further studies where the System Efficiency has to be weighed against another performance inidcator that is dependent on one or more of these parameters. For example, the mass and volume of a heat exchanger increases with its effectiveness. So, Equation 4.7 can be used in conjunction with a similar parametric model that relates Heat Exchanger effectiveness to system weight m to find the ideal balance between System Efficiency and Power Density of the SOFC-GT system.

For values outside this range, the model can be run with the newly added parameter values and the results can be added to the scatter plot. Following this, the values of coefficeints p1, p2 and p3 for Equations 4.5 to 4.7 can be tuned to match the added points on the plot.

### 4.3.3 Multiple-parameter sensitivity study

The second experiment with the steady state model was a multiple-parameter Monte Carlo simulation where the parameter data sets from Section 4.3.2 were mixed and applied to the model in random combinations. The consequence was 100 simulations that generated results that could be analysed to determine the correlation of system electrical efficiency to the selected design parameters of pressure ratio, stack temperature, and effectiveness of the pre-heaters.

The correlation of each parameter (X) to electrical efficiency (η) was calculated using Pearson's correlation and Spearman's Rank correlation.

Pearson's correlation quantifies the degree to which two variables are linearly related to each other. Correlation values range from -1 to +1, where -1 represents a perfect negative correlation, +1 represents a perfect positive correlation, and 0 represents no correlation. It is calculated by Equation 4.8.

**Equation 4.8**

$$r = \frac{\sum((X - \bar{X})(\eta - \bar{\eta}))}{\sqrt{\sum(X - \bar{X})^2 \sum(\eta - \bar{\eta})^2}}$$

Where:

- *r* is the Pearson correlation coefficient.
- X and η are the individual sample points for variables X and η, respectively.
- $\bar{X}$ and $\bar{\eta}$ are the means of the X and η variables, respectively.
- Σ denotes the sum over all observations.

Rank correlation, also known as Spearman's rank correlation coefficient, is a non-parametric

measure of the strength and direction of the monotonic relationship between two variables. It is used when the data is ordinal or when the relationship between variables is not linear. In this method, each datapoint in each variable set is assigned a rank based on its magnitude: higher the value, higher the rank. Then for each pair of observations of the dependent and independent variables, the difference in ranks is calculated and used to determine the Rank Correlation using Equation 4.9.

**Equation 4.9**

$$\rho = 1 - \frac{6\sum d_i^2}{n(n^2-1)}$$

Where:

- $\rho$ is the rank correlation coefficient.
- $d_i$ represents the difference in ranks between parameter X and η at observation i
- $n$ is the number of observations.

In both equations, the coefficients provide a measure of the strength and direction of the relationship between the variables, with values close to -1 or +1 indicating a strong relationship, and values close to 0 indicating a weak or no relationship.

The resulting Correlation and Rank Correlation coefficients are shown by tornado plot in Figure 4.7.

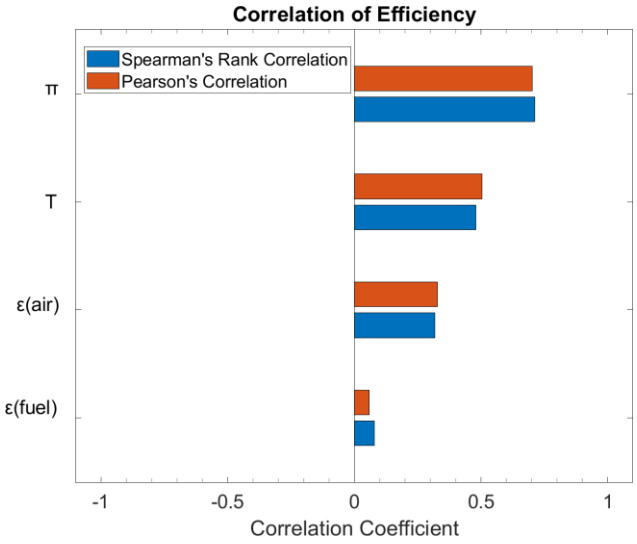


**Figure 4.7 Tornado plot from sensitivity study of efficiency to design parameters**

**Table 4.7 Correlation coefficients from sensitivity study**

| Parameter | Spearman's correlation | Pearson's correlation |
|---|---|---|
| Pressure ratio | 0.71 | 0.70 |
| Fuel Cell Temperature | 0.48 | 0.50 |
| Air pre-heater effectiveness | 0.32 | 0.33 |
| Fuel pre-heater effectiveness | 0.08 | 0.06 |

Results of the sensitivity study therefore show that for a SOFC-GT system operating with 50% fuel utilisation in the stack, the electrical efficiency is most sensitive to pressure ratio, followed by the fuel cell temperature. In the case of the heat exchangers, the air pre-heater appears to have a bigger impact. This is perhaps due to the air-flowrate being tens of times higher than that of the fuel and therefore having a bigger impact on turbine inlet temperature and burner inlet mixture temperatures.

## *4.4 Summary*

This chapter detailed the deployment of steady-state models for a SOFC-GT system. The models aimed to simulate the steady-state performance of the system with minimal experimental data, as required in the early stages of product development. Chapter 3 discussed the model equations and implementation, while this chapter demonstrated their application in design studies and analytical systems engineering to address operating parameters and component sizing.

### 4.4.1 Model Validation

The first section covered the validation of the SOFC steady-state model, essential for ensuring the model's accuracy through comparison with test data or higher-fidelity models.

**Electrochemical Sub-Model Validation:**

- The model was validated by sweeping current density values from 0 to 1.0 A/cm² at a constant fuel flow rate and temperature.
- The produced polarisation curve (V-I curve) was compared with experimental data, showing a good correlation and validating the electrochemical sub-model.
- The model-calculated area-specific resistance (ASR) in the linear region matched literature values, further confirming its accuracy.

**Thermal Sub-Model Validation:**

- The model was validated against the International Energy Agency (IEA) benchmark cases for SOFCs.
- The steady-state model predicted cell temperature, voltage, and stream temperatures, showing less than 2% error for cell temperature and within 20 K for stream temperatures, demonstrating good agreement with the benchmark data.

### 4.4.2 Design Studies

The chapter included two design study applications to illustrate the model's utility and generate insights into SOFC-GT performance.

**Identification of Optimum Current Density**

The system model was run across a range of current densities, revealing that optimal operation occurs between 0.1 and 0.59 A/cm². Within this range, the system maintains low overpotential losses, manageable thermal stresses, and high electrical efficiency, peaking at around 53%.

**Sensitivity Study Using Monte Carlo Simulations**:

This analysis focused on how system design parameters (GT Pressure Ratio, Fuel Cell Temperature, Heat Exchanger Effectiveness) impact electrical efficiency. Pressure ratio and stack temperature significantly influence efficiency, with higher values enhancing performance but also increasing component size and cost. Heat exchanger effectiveness also plays a role, albeit smaller, with air pre-heater effectiveness being more impactful due to higher air flow rates.

### 4.4.3 Conclusion

The chapter successfully validated the steady-state SOFC-GT model and demonstrated its application in optimising operating parameters and conducting sensitivity analyses. The findings provide valuable insights for the design and development of efficient SOFC-GT systems.

# 5 The SOFC-GT dynamic model

## *5.1 Validation of SOFC model*

Due to the absence of experimental data, the SOFC model was tested against reference data collected from literature to validate it. In the target application for this SOFC-GT system, the stack is maintained at steady state conditions as discussed in Section 2.1.2. The main perturbations or disturbances to the steady state come from fuel and air temperature changes when the gas turbine operating point changes. For example, when load demand increases, the gas turbine pressure ratio is increased to meet it. Greater pressure ratio leads to higher post compression air temperature and also higher fuel temperature due to the burner outlet stream temperature increasing and pre-heating the stack inlet stream to a higher temperature [88], [92], [94], [95], [96]. These changes can lead to a change in the cell temperature which affects ASR and consequently the power output. The current demand then has to be adjusted to meet the desired power output [68], [97], [98]. This behaviour is identical between planar and tubular SOFCs as it is a function of the thermal mass of the PEN structure and flow channels, which are treated as homogenous in a 0D model and therefore agnostic to the geometry. For these reasons, the reference datasets chosen for validation are from Chapter 8.4 of “Dynamic Modelling and Predictive Control in Solid Oxide Fuel Cells” [70] where a first-principles model is cross-validated against higher-order models. Cell temperature and voltage calculated by the model were compared against reference values at three conditions that occur during operation of an SOFC:

- Step change in current
- Step change in fuel temperature
- Step change in air temperature

**Response to current step:** Current density demand was stepped up from 0.3 A/cm$^2$ to 0.5 A/cm$^2$. Reference data [70] and the model-calculated values for cell temperature and cell voltage response to this step change were plotted in Figures 5.1 (a) and (c) respectively and their corresponding errors in (b) and (d). As shown by the figures, cell temperature error is within 1% of the reference data, while voltage error is within 3%. At the step itself, voltage error seems to exceed 5% in Figure 5.1 (d) but this is only at one time step of the solver (0.001 s) and can be ignored.

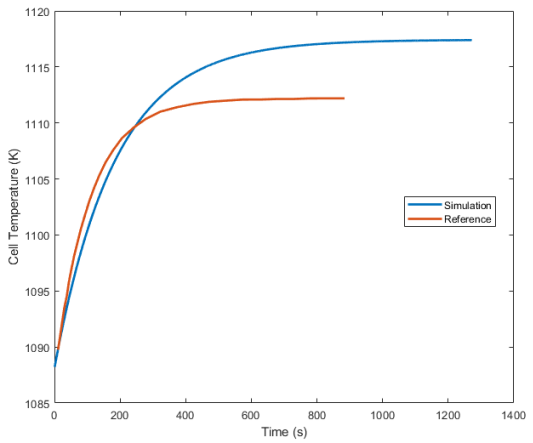


**(a) Model-predicted and reference cell temperature response to step change in current**

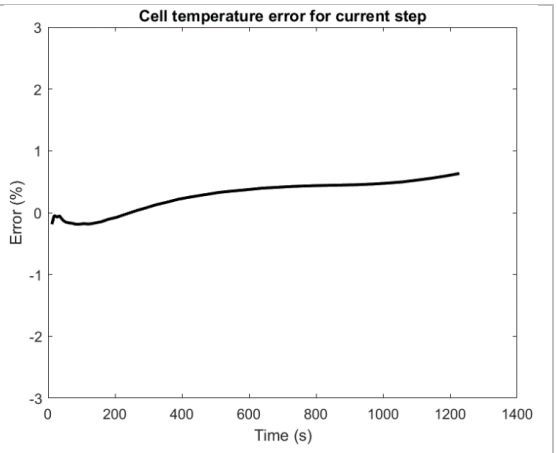


**(b) Error of model prediction for cell temperature response to step change in current**

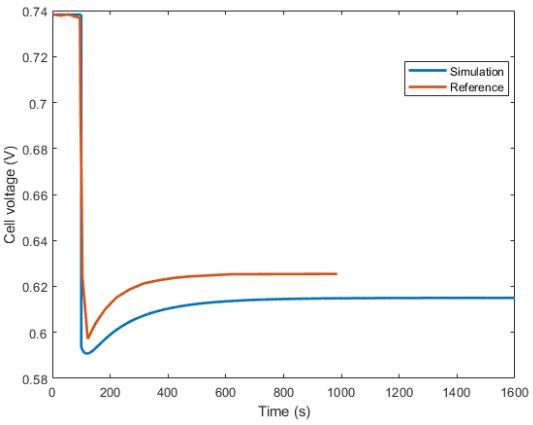


**(c) Model-predicted and reference cell voltage response to step change in current**

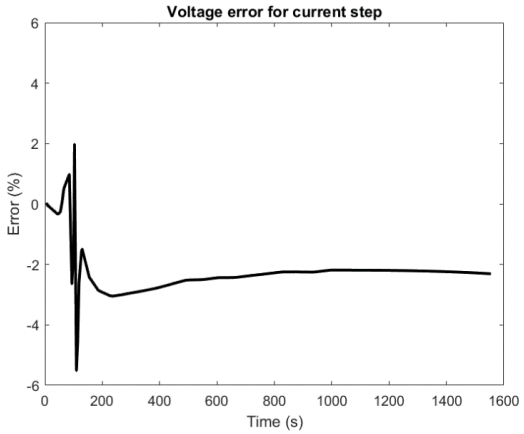


**(d) Error of model prediction for cell voltage response to step change in current**

**Figure 5.1 Validation of SOFC dynamic model for step change in drawn current**

**Response to step change in inlet fuel temperature:** Temperature of the inlet fuel flow was stepped up from 823 K to 873 K. Reference data [70] and the model-calculated values for cell temperature and cell voltage response to this step change were plotted in Figures 5.2 (a) and (c) respectively and their corresponding errors in (b) and (d). As shown by the figures, cell temperature error is within 1% of the reference data, and voltage error is under 2.5%.

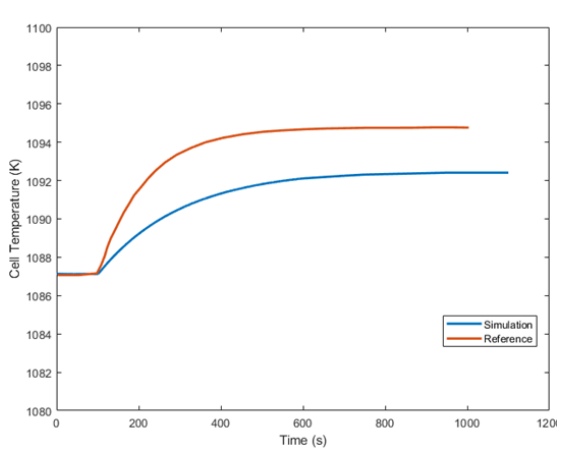


**(a) Model-predicted and reference cell temperature response to step change in inlet fuel temperature**

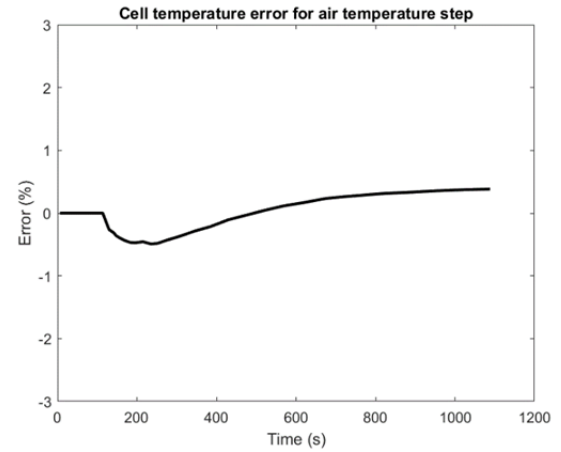


**(b) Error of model prediction for cell temperature response to step change in inlet fuel temperature**

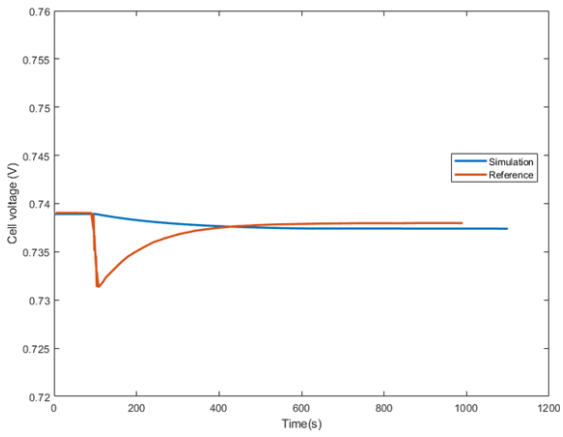


**(c) Model-predicted and reference cell voltage response to step change in inlet fuel temperature**

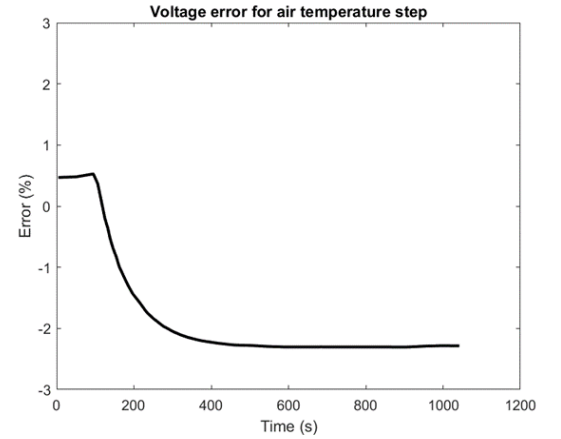


**(d) Error of model prediction for cell voltage response to step change in inlet fuel temperature**

**Figure 5.2 Validation of SOFC dynamic model for step change in inlet fuel temperature**

**Response to step change in inlet air temperature:** Temperature of the inlet fuel flow was stepped up from 1104 K to 1154 K. Reference data [70] and the model-calculated values for cell temperature and cell voltage response to this step change were plotted in Figures 5.3 (a) and (c) respectively and their corresponding errors in (b) and (d). As shown by the figures, cell temperature error is within 0.5% of the reference data, and voltage error is under 1%.

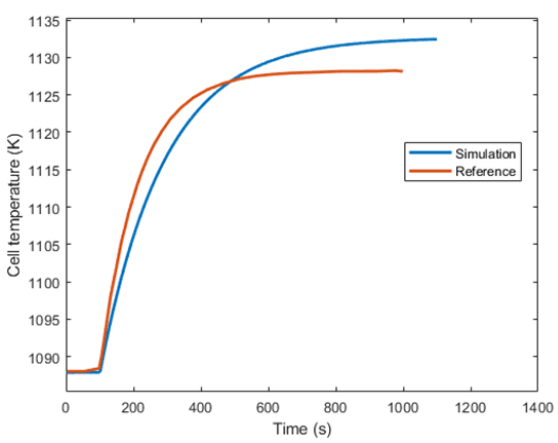


**(a) Model-predicted and reference cell temperature response to step change in inlet air temperature**

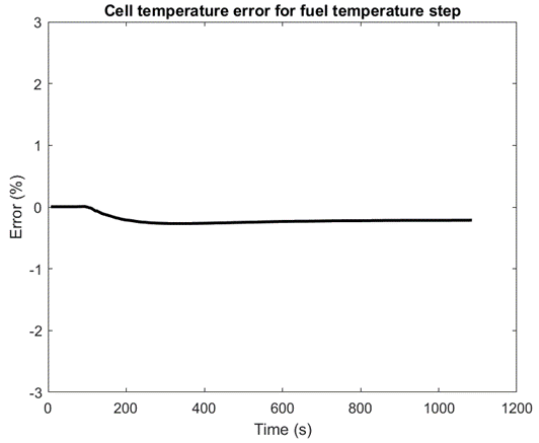


**(b) Error of model prediction for cell temperature response to step change in inlet air temperature**

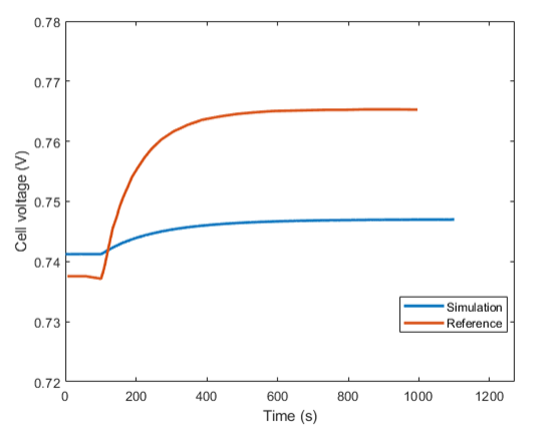


**(c) Model-predicted and reference cell voltage response to step change in inlet air temperature**

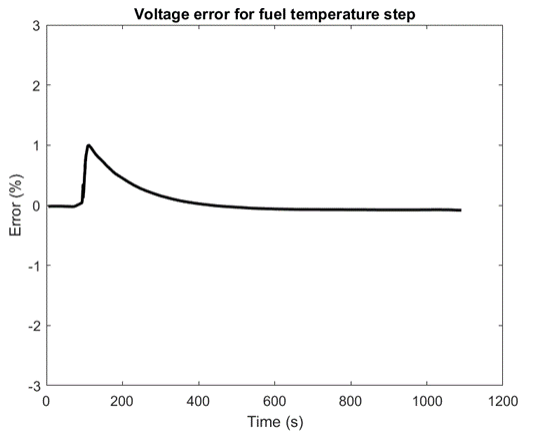


**(d) Error of model prediction for cell voltage response to step change in inlet air temperature**

**Figure 5.3 Validation of SOFC dynamic model for step change in inlet air temperature**

## 5.2 Analysis description

The control strategy is significant in enhancing the load-following performance and efficiency of a Solid Oxide Fuel Cell-Gas Turbine (SOFC-GT) system. As highlighted in the literature review chapter, dynamic operating conditions pose a risk of accelerating the degradation of the cells, underscoring the necessity for a control system that ensures the stack's operating conditions remain within safe limits. Adopting a model-based approach for developing this control strategy is crucial for extending the stack's lifespan. Furthermore, in applications like transport Auxiliary Power Units (APUs) that require dynamic load-following, it's essential to examine the system's load-following capability and optimise the design to reduce discrepancies between load demand and power output at any point in a load cycle. Utilising dynamic models enables the simultaneous simulation of various system designs, allowing for a comparison of electrical efficiency under load-following along with other critical performance and health indicators. This experiment explored the impact of incorporating a SOFC stack into a Brayton Cycle by simulating a Brayton Cycle Gas Turbine generator and a SOFC-GT system with turbine shaft speed-based control, focusing on the system's electrical efficiency across its operating range. To demonstrate how the SOFC-GT dynamic model can be used for this, a load sweep on the SOFC-GT system model was conducted to assess its load-following behaviour, temperature profiles, and electrical efficiency under transient load conditions.

The SOFC model from Chapter 5 was integrated into a dynamic Brayton Cycle system model. The system can be represented by the schematic diagram presented in Figure 5.4.

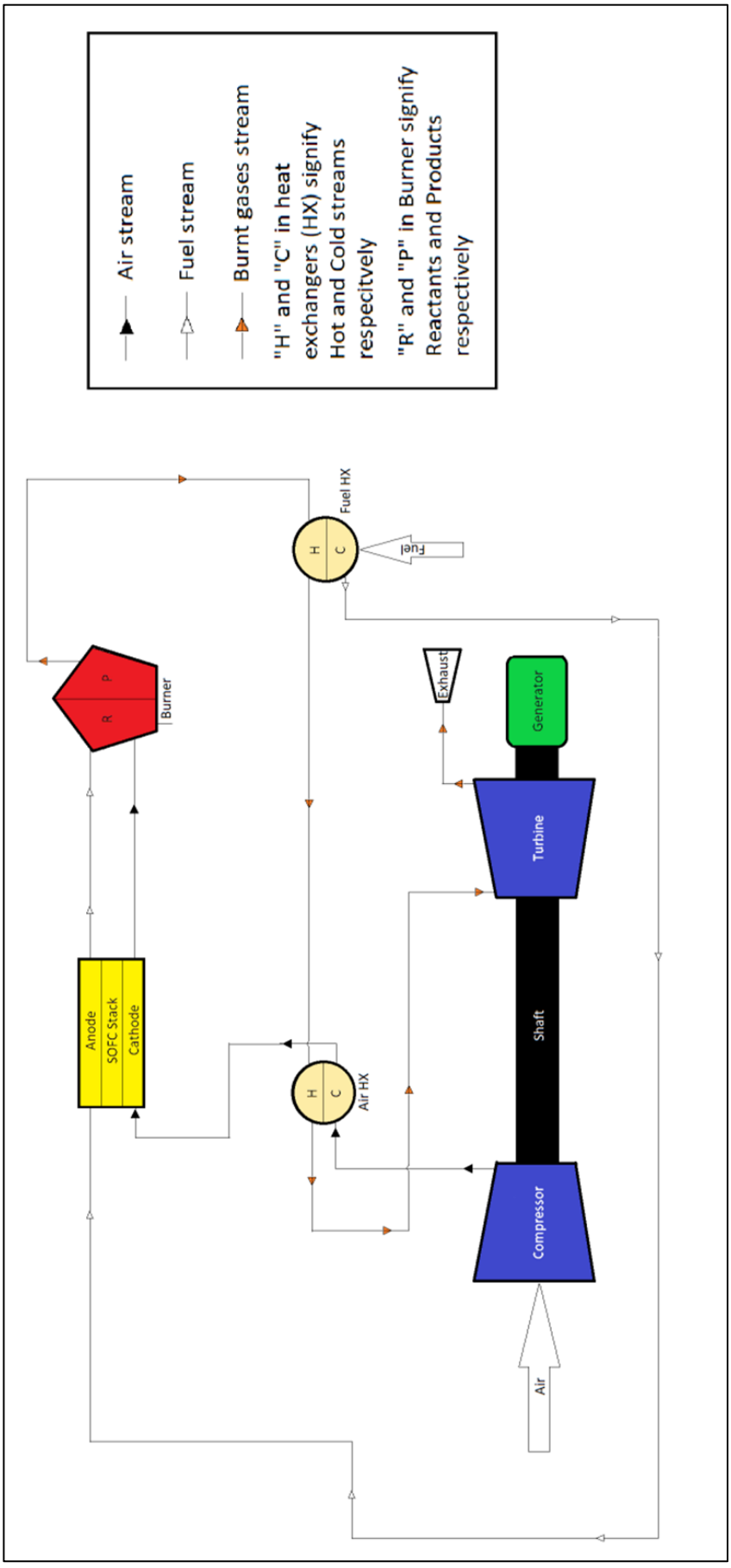


**Figure 5.4 SOFC-GT system schematic**

The Brayton Cycle model used in this simulation was developed by Mathworks and implemented on the Matlab-Simscape platform which follows the bond-graph modelling approach described in Section 3.1.2 and 3.2.2 [99]. The SOFC stack model which was also implemented as a bond-graph model on MATLAB Simulink, was combined with the baseline Brayton Cycle model to create a model of the SOFC-GT hybrid system.

A multiple step load test was simulated on the Brayton Cycle and SOFC-GT models. Power output control of the APU is carried out by adjusting the amount of energy carried by the fluid being expanded through the turbine. For the gas turbine, this comes from the combustion of fuel in the burner, while for the SOFC-GT system, the heat dissipated from the fuel cell is also added [92], [100], [101]. However, it is very difficult to measure the energy carried by the fluid due to inaccuracies in temperature sensors (thermocouples) and changes in species concentrations in the SOFC and burner off-gas. Therefore, for control design, it is required to choose another parameter that has a direct correlation to this energy and the power output of the system [10], [94], [102], [103]. For the APU in this study, that parameter is speed of the turbine and compressor shaft. This speed-based control approach is a proven control method for gas turbine power systems [104], [105], [106]. Shaft speed being a function of the energy added to the system, can be used as the parameter by which the control system decides whether to increase or decrease the fuel added to the system to meet the power demand at a given instant.

The Brayton Cycle GT used in this study has a shaft speed range between 4000 rpm and 12000 rpm that corresponds to baseline and peak power output respectively. The dynamic model of that system is subjected to a multiple load-step test by increasing the shaft speed set-point from 4000 rpm to 12000 rpm in step increments of 1000 rpm at every 100 s interval. The shaft speed profile is shown in Figure 5.5.

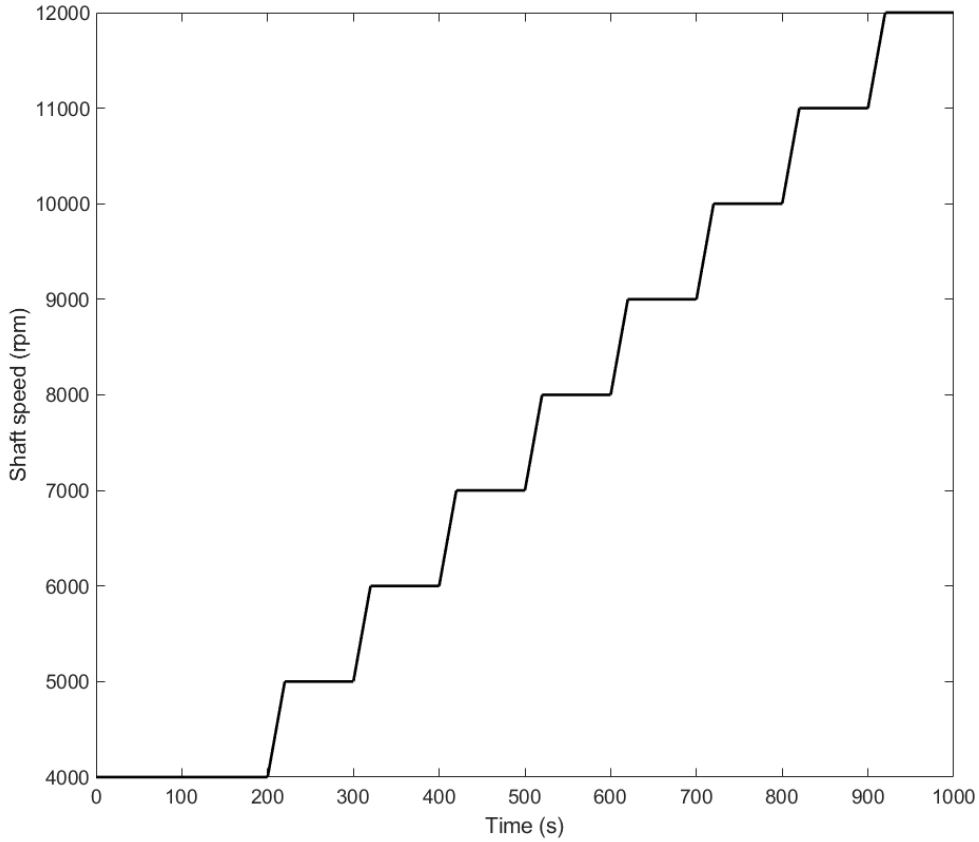


**Figure 5.5 Multiple step speed profile for simulated test**

## 5.3 Brayton Cycle turbine simulation

To get a reference against which to compare the SOFC-GT system results, power output and efficiency of the GT-only Brayton Cycle system for the shaft-speed profile shown in Figure 5.5 is plotted and shown in Figure 5.6.

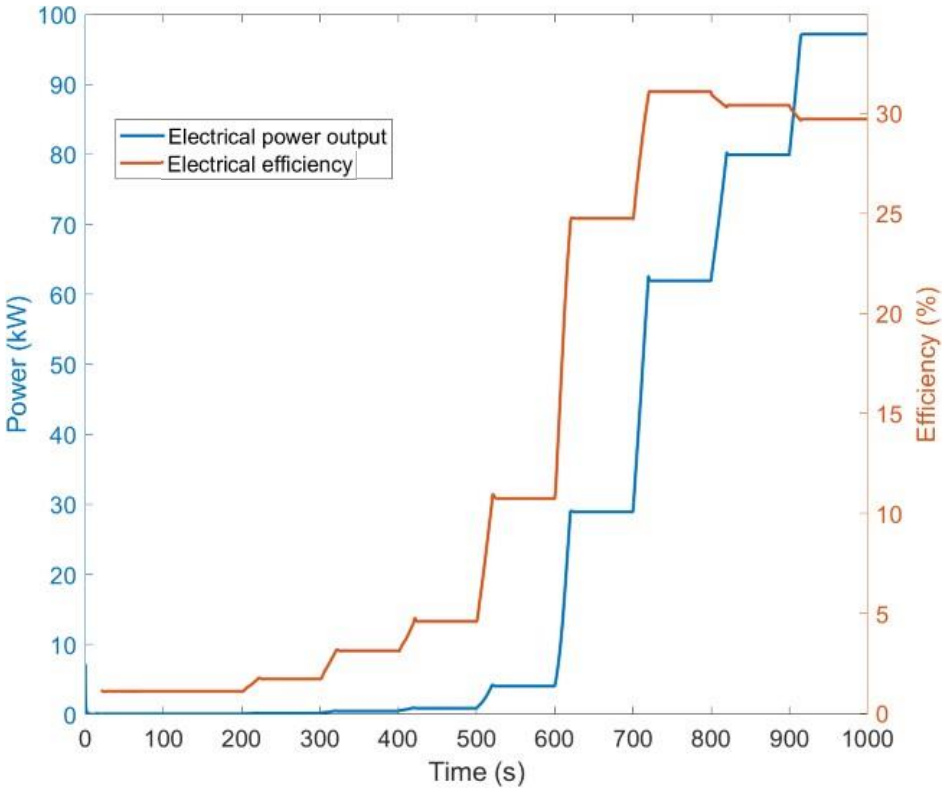


**Figure 5.6 Brayton Cycle Gas Turbine Power output and Electrical efficiency against time during simulation**

It can be seen from Figure 5.6 that peak efficiency of the GT-only system is 31% at a power output of 62 kW. Electrical efficiency increases with power output up to 62 kW and then decreases as power output is increased further. This is because pressure ratio increases with shaft speed and as the pressure ratio of the cycle increases, the theoretical efficiency of the Brayton cycle also increases according to Equation 5.1.

**Equation 5.1**

$$\eta_{th} = 1 - \frac{1}{PR^{\kappa-1/\kappa}}$$

However, beyond a certain shaft speed in practical cases, the work required to drive the compressor increases to a greater degree than the increase in theoretical efficiency. Due to this, more and more of the power produced by the turbine is required to drive the compressor than the electric generator, resulting in decreasing electrical efficiency [107], [108], [109]. The effect of increasing compressor load can be observed in the decrease in the size of electrical

power output steps to 20 kW and 17 kW between 800 s and 1000 s compared to 30 kW and 26 kW between 600 s and 800 s.

## *5.4 SOFC-GT hybrid system simulation*

The shaft speed profile from Section 6.1 was applied as input to the GT control system in the SOFC-GT dynamic model. The fuel flow-rate to the SOFC is kept constant at 1 g/s because the operating strategy followed is one where the SOFC provides the baseline power demand while load increases above that level are covered by the gas turbine [51]. Specifications of the SOFC stack are given in Table 5.1.

**Table 5.1 Specifications and boundary conditions of simulated SOFC stack [70]**

| **Specification** | **Value** |
|---|---|
| Number of cells ($N_c$) | 384 |
| Active area ($A_c$) | 350 $cm^2$ |
| Heat of reaction ($\Delta\widehat{H_r^\circ}$) | 241.8 kJ/mol |
| Charge transfer coefficient ($a$) | 0.5 |
| Ohmic resistance $r_0$ at $T_0$ = 573 K | 0.126 Ω |
| Ohmic resistance coefficient (α) | -2870 |
| Specific molar valve constant of $H_2$ ($K_{H_2}$) | 0.843 atm.mol/s |
| Specific molar valve constant of $O_2$ ($K_{O_2}$) | 2.52 atm.mol/s |
| Specific molar valve constant of $H_2O$ ($K_{H_2O}$) | 0.281 atm.mol/s |
| PEN structure density ($\rho_e$) | 6.6 $g/cm^3$ |
| Interconnect density ($\rho_i$) | 6.11 $g/cm^3$ |
| Thickness of PEN structure ($\Delta w_e$) | 0.25 mm |
| Thickness of interconnect ($\Delta w_i$) | 1.5 mm |
| Specific heat capacity of PEN structure | 400 J $kg^{-1}K^{-1}$ |
| Emissivity ($\epsilon_a, \epsilon_c, \epsilon_i$) | 0.9 |
| Convective heat transfer coefficient ($h_{Fe}, h_{Fi}, h_{Ae}, h_{Ai}$) | 50 W $m^{-2}$ $K^{-1}$ |
| Fuel flowrate | 0.001 kg/s |
| SOFC fuel utilisation | 0.50 |

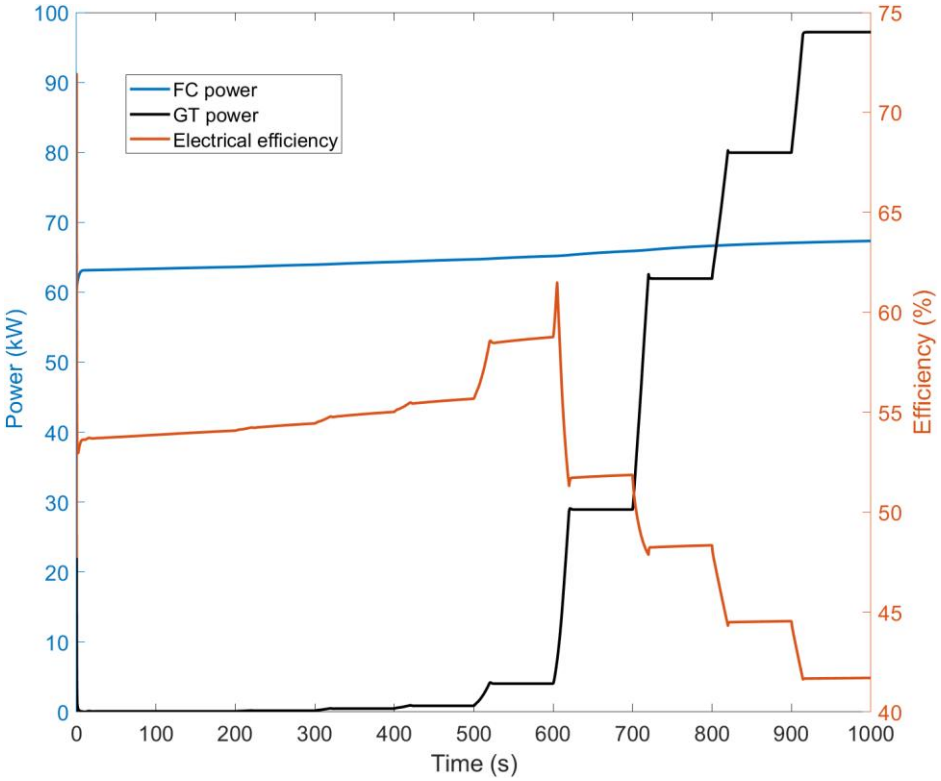


**Figure 5.7 Power outputs and electrical efficiency of SOFC-GT system against time during simulation**

**Electrical efficiency** increases with shaft speed and reaches a peak value of 63%, after which it decreases. This is mainly due to two factors: 1) the voltage and hence efficiency of the fuel cell increases with air pressure according to the Nernst equation and 2) theoretical efficiency or Carnot efficiency of the Brayton cycle increases with pressure ratio.
The decrease in electrical efficiency after the peak can also be attributed to two factors:

- After a certain point in power demand, the energy released by combusting unutilised fuel from the SOFC in the burner and expanding through the turbine becomes insufficient to meet the power demand. Therefore, fuel must be added directly to the Brayton Cycle (called “top-up fuel”) burner to generate the additional heat energy required to meet the power demand. Since the efficiency of combustion and expansion in the turbine is lower than that of the SOFC, the efficiency of the overall system is lowered as more and more top-up fuel is added.
- Efficiency of the Brayton cycle reduces after a certain shaft speed because the energy required to drive the compressor increases disproportionately to the power produced by the turbine, thus reducing the ratio of useful work done by the turbine to total work done.

**SOFC power output**: Fuel flow and current draw are kept constant but, the power output increases due to increasing air pressure and the associated voltage gain. SOFC power output at lowest is 56.2 kW and highest is 67.3 kW all at 85% fuel utilisation and an inlet fuel flow of 1

g/s, corresponding to 53.6 g/kWh at the highest specific fuel consumption and 44.7 g/kWh at lowest specific fuel consumption at the stack: a 16.6% reduction. This is because the SOFC Nernst potential is directly proportional to the square of partial pressure of oxygen.

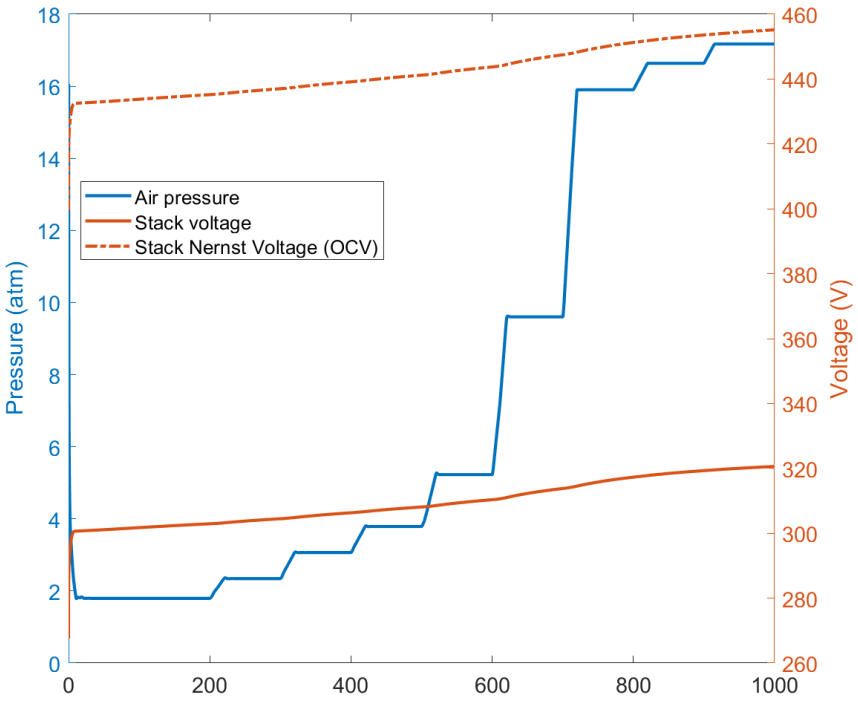


**Figure 5.8 SOFC voltage and Air channel pressure against time during simulation**

Figure 5.8 shows the increase in SOFC voltage along with air pressure against time during the simulation. Cell voltage increases from 0.75 V to 0.84 corresponding to 290 V to 321 V at stack level at constant current. Nernst voltage changed from 1.05 V at cell (404 V stack) to 1.19 V at cell (456 V stack). This means a 10 % increase in stack voltage and a 13% increase in OCV leading to a net increase in the efficiency of the cell as power output increases while fuel consumption (represented by current drawn) remains constant.

Figure 5.9 shows the variation of air pressure at the SOFC inlet during the simulation and the corresponding values of SOFC power and GT power. The increase in air pressure with successive speed loads increases gradually and then starts decreasing after the point of peak GT efficiency noted in Figure 5.7 due to irreversibility losses in the compressor. SOFC power output increases due to the influence of oxygen partial pressure on Nernst potential, and GT power increases as more and more energy is carried by the air expanding through the turbine.

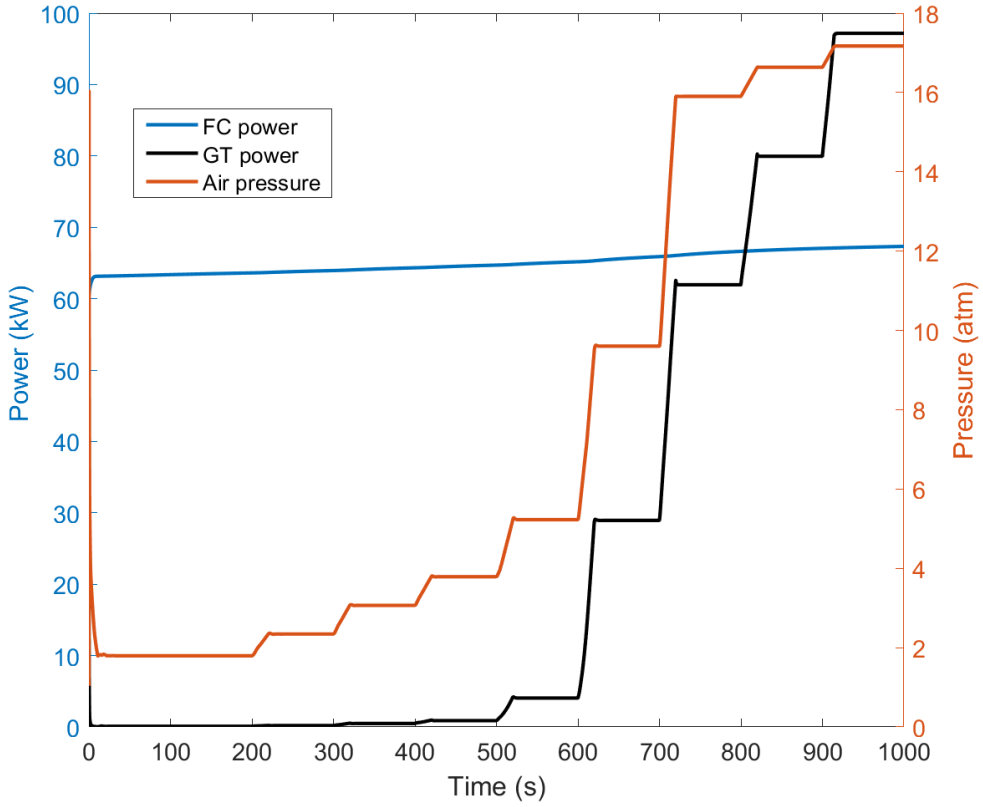


**Figure 5.9 Variation of SOFC and GT power outputs with air pressure during the simulation**

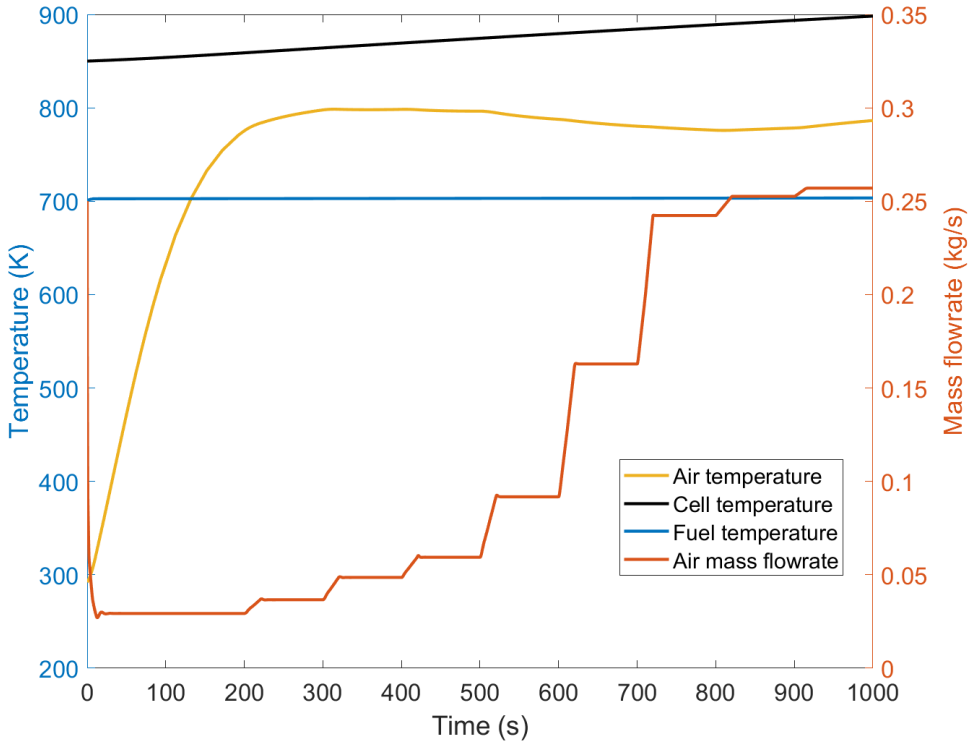


**Figure 5.10 Variation of SOFC temperatures with Air flowrate during simulation**

Figure 5.10 shows the variation of temperatures in the SOFC stack, air and fuel channels during

the simulation plotted along with mass flow rate of air going into the system. Air channel temperature increases with time and reaches a peak value of 788 K at 300s. However, as air flowrate increases, air channel temperature decreases due to excess heat being carried away through convection by the air stream. However, step increases in air flow become smaller after 800 s and hence air channel temperature starts creeping up again as the higher compression pressures increases temperature of incoming air.

This ability of the model to capture SOFC temperature variation with air flow rate is important for model-based control design applications as thermal control in SOFC systems is carried out by altering the flowrate of air going through the stack. When temperatures go over the design value, air flow is increased to carry away excess heat being dissipated from the electrode-electrolyte assembly, and when temperature drops below the design value, air flow is decreased [95], [102], [110], [111].

## *5.5 Summary*

### 5.5.1 Validation of SOFC Model

Due to the lack of experimental data, the SOFC model was validated using reference data from literature. The validation focused on the SOFC-GT system's response to changes in fuel and air temperature, which occur when the gas turbine's operating point shifts. This validation process used data from "Dynamic Modelling and Predictive Control in Solid Oxide Fuel Cells" [70] and included three specific conditions: step changes in current, fuel temperature, and air temperature. The results showed cell temperature and voltage errors within acceptable limits, confirming the model's accuracy.

**Response to Current Step:**

- Current density increased from 0.3 A/cm² to 0.5 A/cm².
- The model's cell temperature error was within 1%, and voltage error within 3%, validating the model's dynamic response.

**Response to Step Change in Fuel Temperature:**

- Inlet fuel temperature increased from 823 K to 873 K.
- The model's cell temperature error was within 1%, and voltage error under 2.5%, indicating good correlation with reference data.

**Response to Step Change in Air Temperature:**

- Inlet air temperature increased from 1104 K to 1154 K.
- The model's cell temperature error was within 0.5%, and voltage error under 1%, further validating the model's accuracy.

### 5.5.2 SOFC-GT system simulation

The SOFC model was integrated into a dynamic Brayton Cycle system model using Matlab-Simscape. A multiple step load test was conducted to compare the performance of the Brayton Cycle and SOFC-GT systems under transient load conditions. The SOFC model used a constant fuel flow rate, with the gas turbine covering load increases above the baseline power provided by the SOFC. Electrical efficiency increased with shaft speed, peaking at 63%, but decreased at higher speeds due to the need for additional fuel and increasing compressor load.

Key findings from the study can be distilled into the following points:

- The SOFC power output increased due to rising air pressure and associated voltage gains, reaching a maximum of 67.3 kW at 85% fuel utilisation.
- The increase in SOFC voltage and efficiency was directly proportional to the partial pressure of oxygen.
- The model accurately captured the SOFC temperature variations, critical for model-based control design to manage thermal conditions in the system.
- The efficiency of the SOFC-GT system peaked at 63% and was influenced by the balance between the energy provided by the SOFC and the gas turbine, with the GT-only Brayton Cycle only achieving a peak efficiency of 31%.

### 5.5.3 Conclusion

The chapter validated the SOFC dynamic model and demonstrated its integration into a Brayton Cycle system for dynamic performance analysis. The findings highlight the importance of a robust control strategy to optimise efficiency of the SOFC-GT system and quantified the improvement in electrical efficiency of SOFC-GT over a GT-only system.

# 6 Simulation of PEMFC system

Simulated driving cycles are important in the realm of automotive powertrain development, serving multiple pivotal roles. These simulations present a controlled framework for the scrutiny and evaluation of various dimensions of a vehicle's powertrain, encompassing fuel efficiency, emissions, and overarching performance. The utility of simulated driving cycles extends notably to the assessment of fuel efficiency, enabling engineers to gauge a vehicle's fuel consumption metrics, such as litres per 100 km (l/100 km) or grammes per kilowatt-hour (g/kWh) case under a spectrum of driving conditions. By mirroring real-world driving scenarios, these cycles facilitate precise fuel efficiency measurements [112], [113], [114].

In this context, the FTP75 driving cycle was selected as the simulation framework for evaluating two specific systems: the compressed air Proton Exchange Membrane Fuel Cell (PEMFC) and the turbocharged PEMFC [115], [116]. The choice of the FTP75 cycle was predicated on its comprehensive representation of urban driving conditions, making it an ideal candidate for this analysis. The focus of the study was to compare the outcomes from these simulations to ascertain the potential fuel savings achievable by integrating a recuperative turbine with a standard compressed air PEMFC system. This initial study aims to highlight the fuel-saving benefits of adopting such a recuperative approach, underscoring the significance of simulated driving cycles in enhancing the efficiency and environmental performance of automotive powertrains.

A pressurised PEMFC system with a recuperative turbine was modelled and compared against a pressurised system without a recuperative turbine to study the improvement in system efficiency with the addition of the turbine. This chapter details the PEMFC system simulation and presents the results from it.

## *6.1 PEMFC Model Validation*

The PEMFC model used in this study is an implementation of the first principles model detailed in Chapter 3.1.3 on MATLAB Simscape. As expressed in Chapter 3.1.3, the equations were accredited to “PEM Fuel Cell Modeling and Simulation Using MATLAB” by Colleen Spiegel [13]. Extensive validation of this model implemented on MATLAB is covered in Chapter 14 of Spiegel’s work. A separate validation study was not performed as part of this project as Simscape is a sub-module of MATLAB and therefore, the model is considered to be already validated.

## 6.2 Analysis description

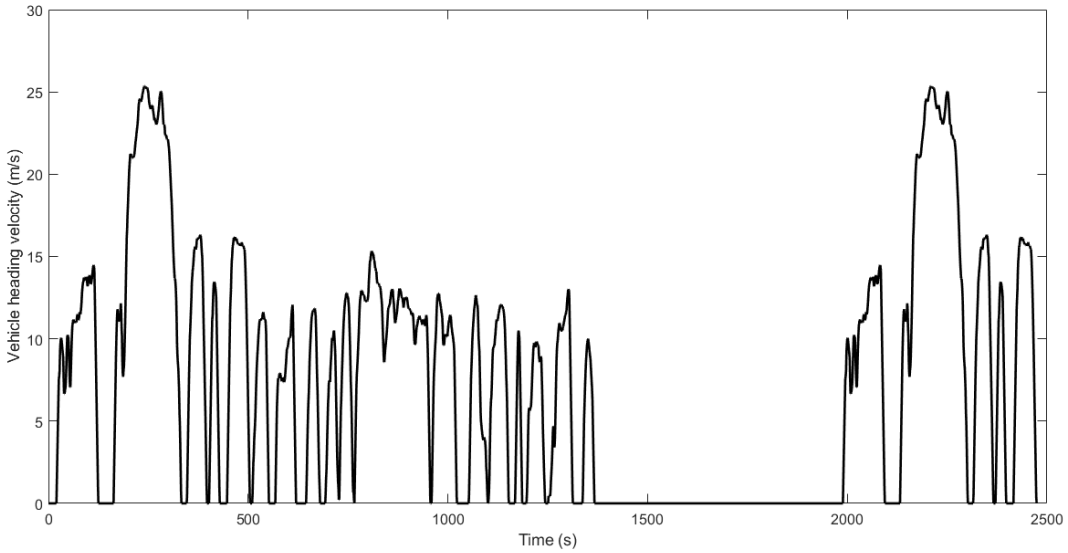


**Figure 6.1 Velocity-time plot of the Federal Test Procedure 75 drive cycle [115]**

The FTP75 driving cycle follows the vehicle speed profile (heading velocity vs time) shown in Figure 6.1.

The heading velocity $v_x$ can be used to calculate the power required to drive a vehicle to the velocity profile in Figure 6.1. using Equation 6.1 where $F_{total}$ is the sum of forces given by Equations 6.2 to 6.4 [117].

**Equation 6.1**

$$Power = F_{total} \times v_x$$

There are three forces that act on a vehicle. The first force acting on a vehicle is that required to move its mass and is called inertia force. It is given by Equation 6.2.

**Equation 6.2**

$$F_{inertia} = m_{vehicle} \cdot a_x = m_{vehicle} \cdot \frac{dv_x}{dt}$$

Where,

- $F_{inertia}$: Inertial force, the force required to change the velocity of the vehicle due to its mass.
- $m_{vehicle}$ : Mass of the vehicle.
- $a_x$: Acceleration of the vehicle in the longitudinal (x) direction.
- $\frac{dv_x}{dt}$: The derivative of the longitudinal velocity with respect to time, which is equivalent to the longitudinal acceleration $a_x$.

The second force is that required to overcome aerodynamic drag. This is given by Equation 6.3.

**Equation 6.3**

$$F_{drag} = \frac{1}{2}.\rho.C_d.A_{fr}.{v_x}^2$$

- $F_{drag}$: Aerodynamic drag force, the force exerted by air resistance opposing the vehicle's motion.
- $\rho$: Mass density of air, which is taken as 1.293 kg/m$^3$
- $C_d$: Drag coefficient, a dimensionless number that characterises the drag of an object in a fluid environment.
- $A_{fr}$: Frontal area, the projected area of the vehicle perpendicular to the direction of motion.

The third force is the one that is required to overcome friction between the vehicle's tyres and the road surface and is given by Equation 6.4.

**Equation 6.4**

$$F_{friction} = \mu_R.m_{vehicle}.g$$

- $F_{friction}$: Friction force, the force exerted by the surface (road) that opposes the sliding or rolling of the vehicle's tyres.
- $\mu_R$: Coefficient of rolling friction, a dimensionless number that represents the amount of friction between the tyres and the road surface.
- $g$: Acceleration due to gravity, which is approximately 9.81 m/s$^2$ on Earth

Based on typical specifications of a small commercial vehicle, the parameter values listed in Table 6.1 were used to calculate the force profile and consequently the power profile corresponding to FTP 75 for that vehicle.

**Table 6.1 Vehicle parameters used in power demand calculation**

| **Parameter** | **Value** |
|---|---|
| Vehicle mass $m_{vehicle}$ | 2500 kg |
| Frontal area $A_{fr}$ | 2 m$^2$ |
| Drag coefficient $C_d$ | 0.36 |
| Friction coefficient $\mu_R$ | 0.02 |

The power profile was then applied to the PEMFC system models described in Section 3.2.3.

The stack model was parameterised with the values shown in Table 6.2. These values were used in Equations 3.59 to 3.62 of the PEMFC model.

**Table 6.2 PEMFC stack parameters**

| Parameter | Value |
|---|---|
| Active Area ($A_{\text{stack}}$) | 280 cm$^2$ |
| Electrolyte membrane thickness ($t_{electrolyte}$) | 0.125 mm |
| Number of cells ($N_{\text{cell}}$) | 400 |
| Gibbs free energy of reaction ($\Delta G$) | 237 kJ/mol |
| Limiting current density ($i_{\text{L}}$) | 1.4 A/cm$^2$ |
| Exchange current density ($i_0$) | 0.0001 A/cm$^2$ |
| Density of dry membrane ($\rho_{\text{m,dry}}$) | 2000 kg/m$^3$ |
| Equivalen weight of dry membrane ($M_{\text{m,dry}}$) | 1.1 kg/mol |
| Density of solid parts of stack (($\rho_{stack}$) | 1800 kg/m$^3$ |
| Fuel utilisation factor | 0.80 |
| Excess oxygen ratio | 2.5 |

## *6.3 Results and discussion*

The power profile calculated as described in 6.1 is applied to both PEMFC systems. Figure 6.2 is shows the power profile applied in both cases: the compressed air PEMFC system (without recuperative turbine) and the turbocharged system (with recuperative turbine).

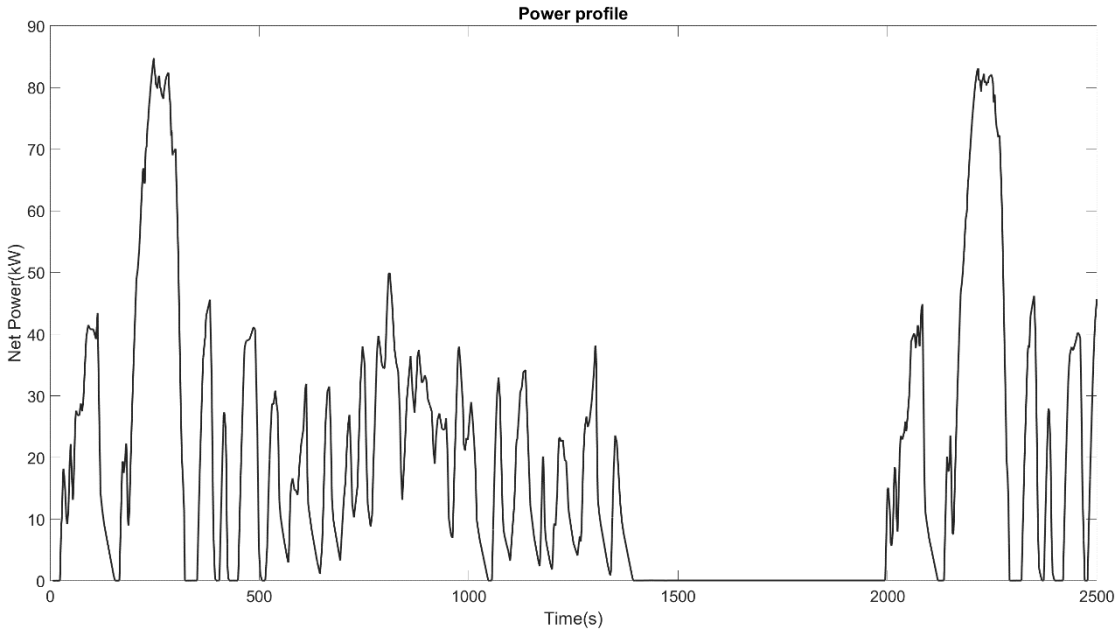


**Figure 6.2 Power demand for FTP 75 drive cycle with vehicle defined in Table 6.1**

As the stacks in the models are run at various curent densities, the corresponding voltage

values were also recorded and the polarisation curve was plotted. This is presented in Figure 6.3.

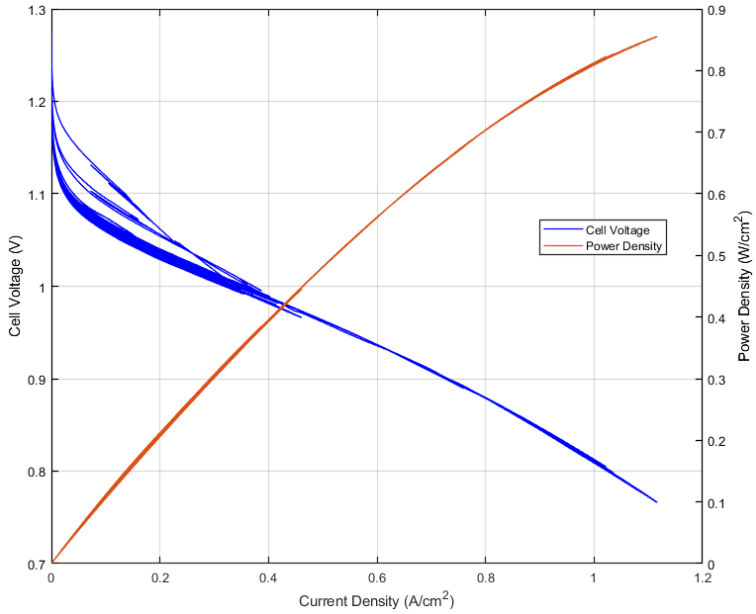


**Figure 6.3 Transient polarisation curves for PEMFC stack**

Figure 6.3 has multiple curves because it is a plot of cell voltage and current density at every time step in the transient simulation. The reason for having multiple voltage values at a given current density is that the stack temperature and electrolyte humidity change during the simulation as the PEMFC follows the load cycle, resulting in different stack resistance values at different time steps. This is especially apparent at lower current densities where the electrochemical reaction rate is slower and therefore temperature and humidity do not reach equilibrium conditions within the time in which current is ramped up [73].

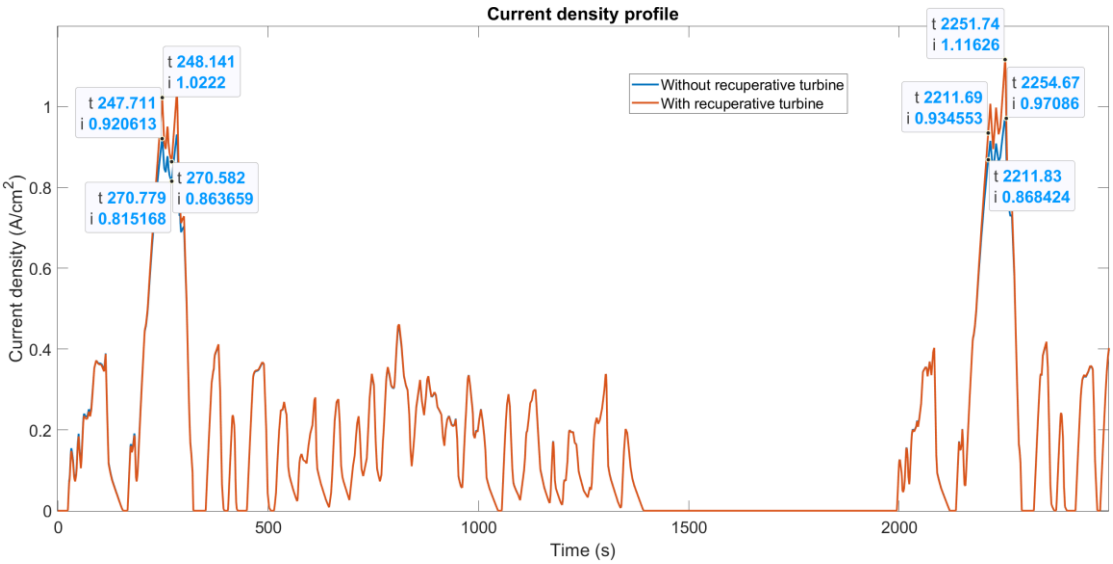


**Figure 6.4 Current density vs time curves for turbocharged and turbine-less PEMFC systems**

Current drawn from the stack ($I$) is a measure of the fuel consumption rate ($\dot{n_{H_2}}$) as they are proportional to each other as defined by the equation:

$$I = \dot{n_{H_2}} \cdot 2F$$

The current density profile of both systems in are shown in Figure 6.4. It is important to note that the current density of the turbocharged system is noticably lower than that of the turbine-less system when the demand exceeds 0.7 A/cm$^2$ corresponding to around 65 kW power demand at the system level. Four data-tips are placed on each curve and they are presented in Table 6.3.

**Table 6.3 Current density comparison of turbocharged and turbine-less PEMFC systems**

| Time | Current density in turbo-charged system | Current density in turbine-less system | Difference | Fuel saving % |
|---|---|---|---|---|
| 248 s | 0.92 A/cm$^2$ | 1.02 A/cm$^2$ | 0.1 A/cm$^2$ | 9.8% |
| 271 s | 0.81 A/cm$^2$ | 0.86 A/cm$^2$ | 0.05 A/cm$^2$ | 5.8% |
| 2222 s | 0.87 A/cm$^2$ | 0.93 A/cm$^2$ | 0.06 A/cm$^2$ | 6.4% |
| 2252 s | 0.97 A/cm$^2$ | 1.12 A/cm$^2$ | 0.15 A/cm$^2$ | 13.4% |

It can be deduced from this data that at peak power demand, the turbocharged system gives a reduction of upto 13.4%. It is lower at power demands below the peak, e.g., 5.8% at the 271 s mark which corresponds to 80% of peak power demand. Therefore, the model shows that the addition of the turbine can offer considerable fuel savings at high power demand.

As a better measure of how this affects the effiiency of the system, the specific fuel consumption, i.e., mass of fuel consumed per unit energy generated, was recorded across the drive cycle and plotted in Figure 6.5.

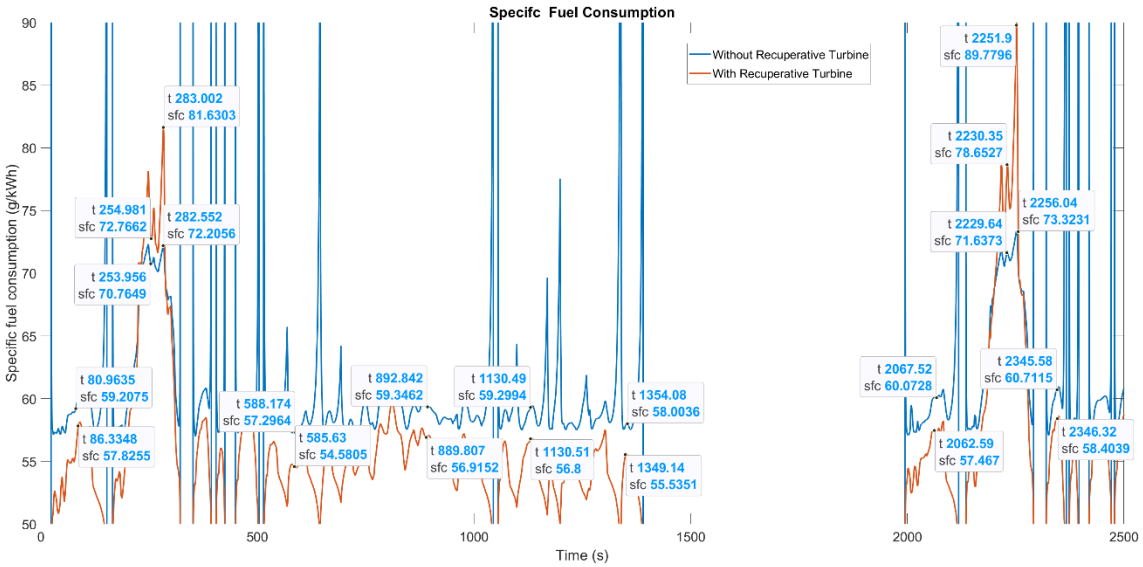


**Figure 6.5 Specific fuel consumption vs time curves for turbocharged and turbine-less PEMFC systems**

The sharp peaks observed in Figure 6.5 are caused by a combination of the sharp gradients in the input power profile and the system of equations solved by the model being stiff, i.e., when some variables solved by the equations change at a different rate to others. The solver deals with this stiffness by taking smaller time steps until convergence is attained, but it also leads to some inaccurate outputs that are represented by the sharp peaks.
To ensure that only accurate results were used in the study, only solutions at stable, larger timesteps were taken and they are noted by datatips in Figure 6.5.

Table 6.4 presents the average readings for specific fuel consumption from Figure 6.5 comparing the two systems.

**Table 6.4 Specific fuel consumption comparison of turbocharged and turbine-less PEMFC systems**

| Data-point no. | Power demand (kW) | SFC of turbo-charged system (g/kWh) | SFC of turbine-less system (g/kWh) | Difference (g/kWh) | SFC reduction by turbine |
|---|---|---|---|---|---|
| 1 | 40.5 | 59.2 | 57.8 | 1.4 | 2.4 % |
| 2 | 80.6 | 72.8 | 70.8 | 2.0 | 2.7 % |
| 3 | 80.7 | 81.6 | 72.2 | 9.4 | 11.5 % |
| 4 | 15.4 | 57.3 | 54.6 | 2.7 | 4.7 % |
| 5 | 33.3 | 59.3 | 56.9 | 2.4 | 4.0 % |
| 6 | 25.8 | 59.3 | 56.8 | 2.5 | 4.2 % |
| 7 | 22.9 | 58.0 | 55.5 | 2.5 | 4.3 % |
| 8 | 40.1 | 60.1 | 57.5 | 2.6 | 4.3 % |
| 9 | 80.8 | 78.6 | 71.6 | 7.0 | 8.9 % |
| 10 | 82.7 | 89.8 | 73.3 | 16.5 | 18.4 % |
| 11 | 45.2 | 60.7 | 58.4 | 2.3 | 3.8 % |
| | | | | | |
| Average | 46.6 kW | 67.0 g/kWh | 62.3 g/kWh | 4.7 g/kWh | 6.3 % |

Across the drive-cycle, the addition of the recuperative turbine achieves a 6.3% saving in specific fuel consumption. A trend can be observed from Table 6.4 that specific fuel consumption increases with power demand. SFC reduction by the addition of the turbine also seems to be higher at higher power demands. However, when comparing Figures 6.5 and 6.4 side-by-side, it can also be seen that SFC reduction in turbocharged system is even greater when the power gradient w.r.t time is sharp. This is especially apparent when comparing datapoints 1 and 8 where the power demand is nearly 40 kW but SFC reduction are 2.4 % and 4.3 % respectively. The conclusion one can draw from this is that a turbocharged PEMFC system has more efficient load-following performance than a pressurised PEMFC system

without a recuperative turbine.

## *6.4 Summary*

This chapter detailed a simulation-based study of the fuel-saving potential of a Turbocharged PEMFC system compared to a pressurised PEMFC system.

The FTP75 driving cycle's velocity-time profile (Figure 6.1) was used to calculate the power required to drive a vehicle. The total force acting on the vehicle includes inertia force, aerodynamic drag, and friction force, calculated using Equations 6.2 to 6.4. These forces were used to derive the power profile, which was then applied to the PEMFC system models.

Typical specifications of a small commercial vehicle were used to calculate the force and power profiles, with parameters listed in Table 6.1. The PEMFC stack was parameterised with values shown in Table 6.2.

### 6.4.1 Simulation results

The power profile derived from the FTP75 drive cycle was applied to both the compressed air PEMFC system and the turbocharged system.

Current density profiles for the two systems were compared and it was notably lower in the turbocharged system when demand exceeds 0.7 A/cm² (around 65 kW power demand). At peak power demand, the turbocharged system achieved up to 13.4% fuel savings, with lower savings at lower power demands, such as 5.8% at 80% of peak power.

The specific fuel consumption (SFC) was recorded across the drive cycle and plotted in Figure 6.5. Across the drive cycle, the turbocharged system achieved an average 6.3% reduction in specific fuel consumption. The data indicates that SFC increased with power demand, and the addition of the turbine offered greater SFC reduction at higher power demands. Comparing Figures 6.5 and 6.4, it is evident that the turbocharged system demonstrates better load-following performance, particularly when power demand increases sharply.

### 6.4.2 Conclusion

The simulation results showed that integrating a recuperative turbine into a PEMFC system offers considerable fuel savings and enhances overall efficiency, particularly under high power demands. The FTP75 driving cycle effectively highlights the benefits of such a system, making it a valuable tool in the development of more efficient automotive powertrains.

# 7 Conclusions and future work

## *7.1 Completion of project aims*

This project has presented a study on the development and use of analytical models of fuel cell gas turbine (FC-GT) hybrid systems for transport applications, focusing on Proton Exchange Membrane Fuel Cells (PEMFC) and Solid Oxide Fuel Cells (SOFC) as the main types of fuel cells. Through diligent research, design, and simulation, the project has achieved the aims set out in Chapter 1.5.1, contributing valuable insights into the potential of FC-GT systems in decarbonising the energy and transport sectors and forming a base on which prototyping and experimental studies of such models can begin. The following paragraphs summarise how the requirements of each aim has been met:

**1) Enable future research and development of FC-GT:** A literature review of FC-GT systems in transport applications was carried out and presented in Chapter 2. This provides information about future research on what configurations of SOFC-GT and PEMFC systems to consider, as well as the control and operating strategies to be followed. For auxiliary power in transport applications, SOFC-GT systems emerged as a promising option, whereas turbo-charged PEMFC systems were deemed more suitable for propulsive power in road transport.

The analytical models developed in this study can be used by researchers to perform design studies, concept definitions and sizing of test-rigs and prototypes for future research. Furthermore, through model-based analyses, the study also identified optimal operating windows of current density and pressure ratios as well as system parameters such as fuel cell temperature and heat exchanger effectiveness for FC-GT systems where the system efficiency is highest, without sacrificing reliability and load following ability which forms a knowledge base to build further up on.

**2) Development of analytical system models:** The major contribution of this study is the development of 0D analytical models that are built on first principles. These models are flexible in terms of the parameter space they can simulate due to the physics-based approach rather than a data-driven approach. This approach also means that they can be used by research labs where no historical data on fuel cells exist.

The implementation of these models in MATLAB/SIMULINK and Simscape makes them accessible and usable for to a wide range of researchers due to the popularity of the MATLAB programming language and tools in both academia and industry. The bond-graph approach presents the models in a graphical layout that mimics Process-Flow Diagrams and presents the users with an interface that can be interacted with easily to change parameters and set up simulations.

**3) Identify the most significant system design and operating parameters:** Chapters 4,5, and 6 deployed the analytical models in design studies and simulations to demonstrate their capabilities and generate insights into FC-GT system performance.

The results from parameter sweeps and multiple-parameter sensitivity studies in Chapter 4 showed the significant impact of pressure ratio, fuel cell temperature, and heat exchanger effectiveness on the system's electrical efficiency. The pressure ratio was identified as the most influential parameter, followed by fuel cell temperature and air pre-heater effectiveness. These findings are essential for guiding the design of more efficient SOFC-GT systems, with implications for economic, environmental, and operational performance.

In Chapter 5, The SOFC model was integrated into a dynamic Brayton Cycle system model, and a multiple step load test was conducted to simulate real-world operational conditions. SOFC power output increased with changes in air pressure, illustrating it's influence on cell performance. Specific fuel consumption of the SOFC stack was decreased by 16.6% by raising the operating pressure from 0.2 MPa to 1.7 MPa in step increases. An analysis of model outputs in Chapter 6 showed that turbocharging a pressurised PEMFC system makes it more efficient under sudden load changes.

**4) Quantify improvements in performance over conventional power sources:** The dynamic modelling and simulation of the SOFC-GT system underscored the potential of integrating fuel cells with gas turbines for improved efficiency and load-following capabilities. The model-based studies highlighted the potential for gross electrical efficiencies greater than 60%, indicating a significant step towards achieving the decarbonisation of the transport sector. Chapter 5 shows that the peak efficiency of a Brayton Cycle Gas Turbine APU under transient load can be increased from 31% to 63%. Comparison of turbocharged vs turbine-less PEMFC systems in Chapter 6 showed that for an identical power profile, the turbocharged systems offers a peak fuel saving of 13.4% and 6.3% on average.

## *7.2 Future work*

To build on the foundations laid by this project, future research may focus on several key areas:

1) **Model-based analyses of more specific transport applications:** This project covered dynamic load simulation of an SOFC-GT Auxiliary Power Unit compared to a Gas Turbine option, and an automotive drive cycle simulation of a turbocharged PEMFC system compared against a pressurised PEMFC system. To expand on this

work, these models can be used to quantify fuel savings and emissions reduction of FC-GT system over conventional sources in other applications. SOFC-GT systems are more suited to applications where efficiency and fuel flexibility take precedence over power density, while Turbocharged PEMFCs are more suited for applications that require high power density. A few examples based on the suitability of SOFC-GT and Turbocharged PEMFC systems for various transport applications are listed below.

- Drive cycle simulation of SOFC-GT propulsion system for rail transport in remote terrains can be compared against diesel engines,
- Load profile simulation of SOFC-GT propulsion system for long-endurance UAVs,
- Drive cycle simulation of Turbocharged PEMFC system for long-haul truck applications,
- Load profile simulation of Turbocharged PEMFC system for passenger aircraft propulsion,
- Load profile simulation of SOFC-GT system for maritime shipping propulsion.

2) **Hardware in the Loop simulations for Control design**: The dynamic models that were developed in this study can be used for Hardware in the Loop (HiL) simulations to test and optimise real control systems for FC-GT systems. HiL simulations involve integrating physical hardware components with the models implemented on MATLAB SIMULINK. This approach allows for the testing and development of control systems under simulated conditions without the need for a full-scale physical implementation. In an HiL setup, the hardware component (e.g., a controller) receives inputs from a simulated environment running on a computer. It processes these inputs as if they were coming from an actual system and then outputs control signals. These control signals are fed back into the simulation, influencing the subsequent state of the virtual environment.

3) **Pilot/Prototype Projects and Real-World Testing**: The models can be used to design, size, and assemble scaled-down pilot/prototype systems of the APU and propulsion systems studied in this project. These prototypes can use control systems developed using the MiL and HiL simulations at first and then be tested to generate data and understanding. The data coming out of these systems can be used to further validate and improve the accuracy of the models (acting as “Digital Twins”) and move further on in the research and development path towards fully realised FC-GT systems.

4) **Techno-economic Analysis**: Conducting comprehensive economic analyses to assess the cost-effectiveness and market viability of FC-GT hybrid systems, identifying potential barriers to adoption and strategies to overcome them. The analytical models developed and used in this study track the energy inputs and outputs to the systems.

These inputs and outputs can be used with cost models to determine the cost implications of fuel consumption, efficiency, electric power consumption, etc. In the energy sector, this is called Levelised Cost of Electricity analysis.

5) **Parametric mass and volume models**: The model-based studies in this project have focused on the energy and efficiency analysis of FC-GT systems. The mass and volume requirements of power sources in the transport sector are very important and this project covered a literature review to identify the right system configurations that meet the mass and volume specific power density constraints. However, a future study may develop and incorporate parametric models that predict how mass and volume of the systems scale according to design parameters such as pressure ratio, heat exchanger effectiveness, fuel cell active area, etc. to include power density to the list of model outputs.

In conclusion, this report has laid a solid foundation for the future exploration and development of FC-GT hybrid systems in transport applications. By continuing to build on this research, there is a clear path towards achieving cleaner, more efficient, and sustainable transport solutions that align with global efforts to combat climate change.

# BIBLIOGRAPHY


[1] J. G. J. Olivier, 'TRENDS IN GLOBAL CO2 AND TOTAL GREENHOUSE GAS EMISSIONS'.

[2] C. Mitchell and P. Connor, 'Renewable energy policy in the UK 1990–2003', *Energy Policy*, vol. 32, no. 17, pp. 1935–1947, Nov. 2004, doi: 10.1016/j.enpol.2004.03.016.

[3] J. Rogelj *et al.*, 'Paris Agreement climate proposals need a boost to keep warming well below 2 °C', *Nature*, vol. 534, no. 7609, pp. 631–639, Jun. 2016, doi: 10.1038/nature18307.

[4] C.-F. Schleussner *et al.*, 'Science and policy characteristics of the Paris Agreement temperature goal', *Nat. Clim. Change*, vol. 6, no. 9, pp. 827–835, Sep. 2016, doi: 10.1038/nclimate3096.

[5] 'Net Zero by 2050 - A Roadmap for the Global Energy Sector', p. 224.

[6] N. K. Borer *et al.*, 'Overcoming the Adoption Barrier to Electric Flight', in *54th AIAA Aerospace Sciences Meeting*, San Diego, California, USA: American Institute of Aeronautics and Astronautics, Jan. 2016. doi: 10.2514/6.2016-1022.

[7] J. A. Sanguesa, V. Torres-Sanz, P. Garrido, F. J. Martinez, and J. M. Marquez-Barja, 'A Review on Electric Vehicles: Technologies and Challenges', *Smart Cities*, vol. 4, no. 1, pp. 372–404, Mar. 2021, doi: 10.3390/smartcities4010022.

[8] L. Van Biert, M. Godjevac, K. Visser, and P. V. Aravind, 'A review of fuel cell systems for maritime applications', *J. Power Sources*, vol. 327, pp. 345–364, Sep. 2016, doi: 10.1016/j.jpowsour.2016.07.007.

[9] A. Dicks and D. A. J. Rand, *Fuel cell systems explained*, Third edition. Hoboken, NJ, USA: Wiley, 2018.

[10] M. A. Azizi and J. Brouwer, 'Progress in solid oxide fuel cell-gas turbine hybrid power systems: System design and analysis, transient operation, controls and optimization', *Appl. Energy*, vol. 215, pp. 237–289, Apr. 2018, doi: 10.1016/j.apenergy.2018.01.098.

[11] S. Baudoin, I. Vechiu, H. Camblong, J.-M. Vinassa, and L. Barelli, 'Sizing and control of a Solid Oxide Fuel Cell/Gas microTurbine hybrid power system using a unique inverter for rural microgrid integration', *Appl. Energy*, vol. 176, pp. 272–281, Aug. 2016, doi: 10.1016/j.apenergy.2016.05.066.

[12] T. Choudhary and M. K. Sahu, 'Energy and Exergy Analysis of Solid Oxide Fuel Cell Integrated with Gas Turbine Cycle—"A Hybrid Cycle"', in *Renewable Energy and its Innovative Technologies*, J. Chattopadhyay, R. Singh, and O. Prakash, Eds., Singapore: Springer Singapore, 2019, pp. 139–153. doi: 10.1007/978-981-13-2116-0_12.

[13] C. Spiegel, *PEM fuel cell modeling and simulation using Matlab*. Amsterdam :Boston: Academic Press/Elsevier, 2008.

[14] J. Milewski, K. Świrski, M. Santarelli, and P. Leone, *Advanced Methods of Solid Oxide Fuel Cell Modeling*. in Green Energy and Technology. London: Springer London, 2011. doi: 10.1007/978-0-85729-262-9.

[15] E. Fontes and H. Ekström, 'Modeling and Simulation in Fuel Cell Development'.

[16] 'Fuel Cell Handbook (Seventh Edition)'.

[17] M. A. Abdelkareem, K. Elsaid, T. Wilberforce, M. Kamil, E. T. Sayed, and A. Olabi, 'Environmental aspects of fuel cells: A review', *Sci. Total Environ.*, vol. 752, p. 141803, Jan. 2021, doi: 10.1016/j.scitotenv.2020.141803.

[18] J. Botti and C. E. Speck, 'Solid Oxide Fuel Cell Power Unit for Hybrid Vehicles and Electric Vehicles', presented at the 7th International Conference on Engines for Automobile, Sep. 2005, pp. 2005-24–094. doi: 10.4271/2005-24-094.

[19] P. Corbo, F. Migliardini, and O. Veneri, *Hydrogen Fuel Cells for Road Vehicles*. in Green Energy and Technology. London: Springer London, 2011. doi: 10.1007/978-0-85729-136-3.

[20] M. A. Azizi and J. Brouwer, 'Stall/surge dynamics of a multi-stage air compressor in response to a load transient of a hybrid solid oxide fuel cell-gas turbine system', *J. Power Sources*, vol. 365, pp. 408–418, Oct. 2017, doi: 10.1016/j.jpowsour.2017.09.010.

[21] S. Campanari, G. Manzolini, A. Beretti, and U. Wollrab, 'Performance Assessment of Turbocharged Pem Fuel Cell Systems for Civil Aircraft Onboard Power Production', *J. Eng. Gas Turbines Power*, vol. 130, no. 2, p. 021701, Mar. 2008, doi: 10.1115/1.2772636.

[22] G. Kaur, Ed., *PEM fuel cells: fundamentals, advanced technologies, and practical application*. Amsterdam Kidlington Cambridge, MA: Elsevier, 2022.
[23] K. Kendall and M. Kendall, *High-temperature solid oxide fuel cells for the 21st century: fundamentals, design and applications*. London: Academic Press is an imprint of Elsevier, 2016.
[24] R. Bove and S. Ubertini, *Modeling Solid Oxide Fuel Cells: Methods, Procedures and Techniques*. 2008.
[25] M. Boaro and A. A. Salvatore, Eds., *Advances in Medium and High Temperature Solid Oxide Fuel Cell Technology*, vol. 574. in CISM International Centre for Mechanical Sciences, vol. 574. Cham: Springer International Publishing, 2017. doi: 10.1007/978-3-319-46146-5.
[26] S. K. Park and T. S. Kim, 'Comparison between pressurized design and ambient pressure design of hybrid solid oxide fuel cell-gas turbine systems', *J. Power Sources*, vol. 163, no. 1 SPEC. ISS., pp. 490–499, 2006, doi: 10.1016/j.jpowsour.2006.09.036.
[27] D. P. Bakalis and A. G. Stamatis, 'Incorporating available micro gas turbines and fuel cell: Matching considerations and performance evaluation', *Appl. Energy*, vol. 103, pp. 607–617, Mar. 2013, doi: 10.1016/j.apenergy.2012.10.026.
[28] A. Nakajo, Z. Wuillemin, J. Van Herle, and D. Favrat, 'Simulation of thermal stresses in anode-supported solid oxide fuel cell stacks. Part II: Loss of gas-tightness, electrical contact and thermal buckling', *J. Power Sources*, vol. 193, no. 1, pp. 216–226, Aug. 2009, doi: 10.1016/j.jpowsour.2008.12.039.
[29] S. Celik, B. Ibrahimoglu, M. D. Mat, Y. Kaplan, and T. N. Veziroglu, 'Micro level two dimensional stress and thermal analysis anode/electrolyte interface of a solid oxide fuel cell', *Int. J. Hydrog. Energy*, vol. 40, no. 24, pp. 7895–7902, Jun. 2015, doi: 10.1016/j.ijhydene.2014.10.057.
[30] H. Djamel, A. Hafsia, Z. Bariza, B. M. Hocine, and O. Kafia, 'Thermal field in SOFC fed by hydrogen: Inlet gases temperature effect', *Int. J. Hydrog. Energy*, vol. 38, no. 20, pp. 8575–8583, Jul. 2013, doi: 10.1016/j.ijhydene.2013.01.004.
[31] A. Himansu, J. E. Freeh, C. J. Steffen, R. T. Tornabene, and X.-Y. J. Wang, 'Hybrid Solid Oxide Fuel Cell/Gas Turbine System Design for High Altitude Long Endurance Aerospace Missions', 2006.
[32] B. K. Park and S. A. Barnett, 'Boosting solid oxide fuel cell performance: Via electrolyte thickness reduction and cathode infiltration', *J. Mater. Chem. A*, vol. 8, no. 23, pp. 11626–11631, 2020, doi: 10.1039/d0ta04280c.
[33] J. T. Pukrushpan, A. G. Stefanopoulou, and H. Peng, *Control of Fuel Cell Power Systems*. in Advances in Industrial Control. London: Springer London, 2004. doi: 10.1007/978-1-4471-3792-4.
[34] T. Wittmann, S. Lück, C. Bode, and J. Friedrichs, 'Modelling the Condensation Phenomena within the Radial Turbine of a Fuel Cell Turbocharger', *Int. J. Turbomach. Propuls. Power*, vol. 6, no. 3, p. 23, Jul. 2021, doi: 10.3390/ijtpp6030023.
[35] A. Kerviel, A. Pesyridis, A. Mohammed, and D. Chalet, 'An Evaluation of Turbocharging and Supercharging Options for High-Efficiency Fuel Cell Electric Vehicles', *Appl. Sci.*, vol. 8, no. 12, p. 2474, Dec. 2018, doi: 10.3390/app8122474.
[36] B. Ghorbani and K. Vijayaraghavan, '3D and simplified pseudo-2D modeling of single cell of a high temperature solid oxide fuel cell to be used for online control strategies', *Int. J. Hydrog. Energy*, vol. 43, no. 20, pp. 9733–9748, May 2018, doi: 10.1016/j.ijhydene.2018.03.211.
[37] A. Subramanian, T. Gundersen, and T. Adams, 'Modeling and Simulation of Energy Systems: A Review', *Processes*, vol. 6, no. 12, p. 238, Nov. 2018, doi: 10.3390/pr6120238.
[38] Caisheng Wang and M. H. Nehrir, 'A Physically Based Dynamic Model for Solid Oxide Fuel Cells', *IEEE Trans. Energy Convers.*, vol. 22, no. 4, pp. 887–897, Dec. 2007, doi: 10.1109/TEC.2007.895468.
[39] S. Song, X. Xiong, X. Wu, and Z. Xue, 'Modeling the SOFC by BP neural network algorithm', *Int. J. Hydrog. Energy*, vol. 46, no. 38, pp. 20065–20077, Jun. 2021, doi: 10.1016/j.ijhydene.2021.03.132.
[40] R. Sinha, C. J. J. Paredis, V.-C. Liang, and P. K. Khosla, 'Modeling and Simulation Methods for Design of Engineering Systems', *J. Comput. Inf. Sci. Eng.*, vol. 1, no. 1, pp. 84–91, Mar. 2001, doi: 10.1115/1.1344877.
[41] N. K. Borer, 'Catalyzing disruptive mobility opportunities through transformational aviation

power', *2018 Aviat. Technol. Integr. Oper. Conf.*, pp. 1–16, 2018, doi: 10.2514/6.2018-3356.
[42] S. C. Singhal and K. Kendall, *High-temperature Solid Oxide Fuel Cells: Fundamentals, Design and Applications*. 2003. doi: 10.1016/B978-1-85617-387-2.X5016-8.
[43] D. W. Ni, B. Charlas, K. Kwok, T. T. Molla, P. V. Hendriksen, and H. L. Frandsen, 'Influence of temperature and atmosphere on the strength and elastic modulus of solid oxide fuel cell anode supports', *J. Power Sources*, vol. 311, pp. 1–12, 2016, doi: 10.1016/j.jpowsour.2016.02.027.
[44] X. Wu, D. Yang, J. Wang, and X. Li, 'Temperature gradient control of a solid oxide fuel cell stack', *J. Power Sources*, vol. 414, no. November 2018, pp. 345–353, 2019, doi: 10.1016/j.jpowsour.2018.12.058.
[45] J. C. Goldsby, I. J. Jakupca, S. C. Farmer, R. D. Green, B. T. Demattia, and P. L. Loyselle, 'Evaluation studies of an 800 W solid oxide-based fuel cell stack for electrical power in aviation', *2018 Aviat. Technol. Integr. Oper. Conf.*, 2018, doi: 10.2514/6.2018-3360.
[46] D. Verstraete, K. Lehmkuehler, A. Gong, J. R. Harvey, G. Brian, and J. L. Palmer, 'Characterisation of a hybrid, fuel-cell-based propulsion system for small unmanned aircraft', *J. Power Sources*, vol. 250, pp. 204–211, 2014, doi: 10.1016/j.jpowsour.2013.11.017.
[47] D. F. Waters and C. P. Cadou, 'Engine-integrated solid oxide fuel cells for efficient electrical power generation on aircraft', *J. Power Sources*, vol. 284, pp. 588–605, 2015, doi: 10.1016/j.jpowsour.2015.02.108.
[48] D. F. Waters and C. P. Cadou, 'Engine-integrated solid oxide fuel cells for efficient electrical power generation on aircraft', *J. Power Sources*, vol. 284, pp. 588–605, 2015, doi: 10.1016/j.jpowsour.2015.02.108.
[49] Z. Ji, J. Qin, K. Cheng, H. Liu, S. Zhang, and P. Dong, 'Performance evaluation of a turbojet engine integrated with interstage turbine burner and solid oxide fuel cell', *Energy*, vol. 168, pp. 702–711, 2019, doi: 10.1016/j.energy.2018.11.088.
[50] T. Choudhary, M. Sahu, and S. Krishna, 'Thermodynamic Analysis of Solid Oxide Fuel Cell Gas Turbine Hybrid System for Aircraft Power Generation', *SAE Tech. Pap.*, vol. 2017-Septe, no. May 2000, 2017, doi: 10.4271/2017-01-2062.
[51] Z. Jia, J. Sun, H. Dobbs, and J. King, 'Feasibility study of solid oxide fuel cell engines integrated with sprinter gas turbines: Modeling, design and control', *J. Power Sources*, vol. 275, pp. 111–125, 2015, doi: 10.1016/j.jpowsour.2014.10.203.
[52] D. McLarty, J. Brouwer, and S. Samuelsen, 'Fuel cell-gas turbine hybrid system design part I: Steady state performance', *J. Power Sources*, vol. 257, pp. 412–420, 2014, doi: 10.1016/j.jpowsour.2013.11.122.
[53] R. Peters *et al.*, 'Efficiency analysis of a hydrogen-fueled solid oxide fuel cell system with anode off-gas recirculation', *J. Power Sources*, vol. 328, pp. 105–113, 2016, doi: 10.1016/j.jpowsour.2016.08.002.
[54] N. K. Borer, S. C. Geuther, B. L. Litherland, and L. Kohlman, 'Design and performance of a hybrid-electric fuel cell flight demonstration concept', *2018 Aviat. Technol. Integr. Oper. Conf.*, pp. 1–15, 2018, doi: 10.2514/6.2018-3357.
[55] K. V. Papathakis, O. C. Shnarr, T. M. Lavelle, N. K. Borer, T. Stoia, and S. Atreya, 'Integration concept for a hybrid-electric solid-oxide fuel cell power system into the X-57 "Maxwell"', in *2018 Aviation Technology, Integration, and Operations Conference*, 2018, pp. 1–10. doi: 10.2514/6.2018-3359.
[56] D. McLarty, Y. Kuniba, J. Brouwer, and S. Samuelsen, 'Experimental and theoretical evidence for control requirements in solid oxide fuel cell gas turbine hybrid systems', *J. Power Sources*, vol. 209, pp. 195–203, 2012, doi: 10.1016/j.jpowsour.2012.02.102.
[57] P. Aguiar, D. J. L. Brett, and N. P. Brandon, 'Solid oxide fuel cell/gas turbine hybrid system analysis for high-altitude long-endurance unmanned aerial vehicles', *Int. J. Hydrog. Energy*, vol. 33, no. 23, pp. 7214–7223, 2008, doi: 10.1016/j.ijhydene.2008.09.012.
[58] E. Valencia, V. Hidalgo, P. Laskaridis, D. Nalianda, and C. Liu, 'Design point analysis of a hybrid fuel cell gas turbine cycle for advanced distributed propulsion systems', in *51st AIAA/SAE/ASEE Joint Propulsion Conference*, 2015.
[59] K. Okai, H. Fujiwara, H. Nomura, T. Tagashira, and R. Yanagi, 'Performance analysis of a fuel cell hybrid aviation propulsion system', in *10th Annual International Energy Conversion Engineering Conference, IECEC 2012*, 2012, pp. 1–6.
[60] A. Bierig, F. Nikodem, P. Gallun, and C. Greiner-Perth, 'Design of the general systems for the SAGITTA demonstrator UAV', in *2017 International Conference on Unmanned*

*Aircraft Systems (ICUAS)*, Miami, FL, USA: IEEE, Jun. 2017, pp. 1767–1777. doi: 10.1109/ICUAS.2017.7991305.
[61] M. D. Fernandes *et al.*, 'SOFC-APU systems for aircraft: A review', *Int. J. Hydrog. Energy*, vol. 43, no. 33, pp. 16311–16333, Aug. 2018, doi: 10.1016/j.ijhydene.2018.07.004.
[62] A. M. Abdalla, S. Hossain, O. B. Nisfindy, A. T. Azad, M. Dawood, and A. K. Azad, 'Hydrogen production, storage, transportation and key challenges with applications: A review', *Energy Convers. Manag.*, vol. 165, pp. 602–627, Jun. 2018, doi: 10.1016/j.enconman.2018.03.088.
[63] R. Kirner, L. Raffaelli, A. Rolt, P. Laskaridis, G. Doulgeris, and R. Singh, 'An assessment of distributed propulsion: Part B – Advanced propulsion system architectures for blended wing body aircraft configurations', *Aerosp. Sci. Technol.*, vol. 50, pp. 212–219, Mar. 2016, doi: 10.1016/j.ast.2015.12.020.
[64] N. Stetson and M. Wieliczko, 'Hydrogen technologies for energy storage: A perspective', *MRS Energy & Sustainability*, vol. 7, no. 1. 2020. doi: 10.1557/mre.2020.43.
[65] R. M. Sullivan *et al.*, 'Engineering Analysis Studies for Preliminary Design of Lightweight Cryogenic Hydrogen Tanks in UAV Applications', 2006.
[66] A. Eftekhari and B. Fang, 'Electrochemical hydrogen storage: Opportunities for fuel storage, batteries, fuel cells, and supercapacitors', *Int. J. Hydrog. Energy*, vol. 42, no. 40, pp. 25143–25165, Oct. 2017, doi: 10.1016/j.ijhydene.2017.08.103.
[67] J.-P. Ansermet and S. D. Brechet, *Principles of Thermodynamics*, 1st ed. Cambridge University Press, 2018. doi: 10.1017/9781108620932.
[68] M. Peksen, A. Al-Masri, L. Blum, and D. Stolten, '3D transient thermomechanical behaviour of a full scale SOFC short stack', *Int. J. Hydrog. Energy*, vol. 38, no. 10, pp. 4099–4107, Apr. 2013, doi: 10.1016/j.ijhydene.2013.01.072.
[69] B. Todd and J. B. Young, 'Thermodynamic and transport properties of gases for use in solid oxide fuel cell modelling', *J. Power Sources*, vol. 110, no. 1, pp. 186–200, Jul. 2002, doi: 10.1016/S0378-7753(02)00277-X.
[70] B. Huang, Y. Qi, and A. M. Murshed, *Dynamic Modelling and Predictive Control in Solid Oxide Fuel Cells: First Principle and Data-Based Approaches: Huang/Dynamic Modelling and Predictive Control in Solid Oxide Fuel Cells: First Principle and Data-Based Approaches*. Chichester, UK: John Wiley & Sons, Ltd, 2013. doi: 10.1002/9781118501054.
[71] Mathworks Inc., 'Matlab Documentation 2023b', in *Matlab Documentation 2023b*. [Online]. Available: https://uk.mathworks.com/help/hydro/ug/sscfluids_brayton_cycle.html?s_tid=srchtitle_site_search_2_brayton%2520cycle
[72] F. Gao, B. Blunier, and A. Miraoui, Eds., *Proton exchange membrane fuel cells modeling*. London : Hoboken, NJ: ISTE ; Wiley, 2012.
[73] S. Dutta, S. Shimpalee, and J. W. Van Zee, 'Numerical prediction of mass-exchange between cathode and anode channels in a PEM fuel cell', *Int. J. Heat Mass Transf.*, vol. 44, no. 11, pp. 2029–2042, Jun. 2001, doi: 10.1016/S0017-9310(00)00257-X.
[74] T. L. Bergman and F. P. Incropera, Eds., *Fundamentals of heat and mass transfer*, 7th ed. Hoboken, NJ: Wiley, 2011.
[75] P. Meier, *Energy Systems Analysis for Developing Countries*. Berlin, Heidelberg: Springer Berlin Heidelberg, 1984.
[76] W. Borutzky, Ed., *Bond Graph Modelling of Engineering Systems: Theory, Applications and Software Support*. New York, NY: Springer New York, 2011. doi: 10.1007/978-1-4419-9368-7.
[77] D. Karnopp, D. L. Margolis, and R. C. Rosenberg, *System dynamics: modeling, simulation, and control of mechatronic systems*, 5. ed. Hoboken, NJ: Wiley, 2012.
[78] H. Raiffa and R. Schlaifer, *Applied statistical decision theory*, Wiley classics library ed. in Wiley classics library. New York: Wiley, 2000.
[79] N. Metropolis and S. Ulam, 'The Monte Carlo Method', *J. Am. Stat. Assoc.*, vol. 44, no. 247, pp. 335–341, Sep. 1949, doi: 10.1080/01621459.1949.10483310.
[80] R. L. Smith, 'Efficient Monte Carlo Procedures for Generating Points Uniformly Distributed over Bounded Regions', *Oper. Res.*, vol. 32, no. 6, pp. 1296–1308, Dec. 1984, doi: 10.1287/opre.32.6.1296.
[81] *Monte Carlo: Concepts, Algorithms, and Applications*. Cham: Springer International Publishing.
[82] R. Y. Rubinstein and D. P. Kroese, *Simulation and the Monte Carlo method*, Third edition.

in Wiley series in probability and statistics. Hoboken, New Jersey: John Wiley & Sons, Inc, 2017.
[83] J. Liang, Z. P. Mourelatos, and J. Tu, 'A single-loop method for reliability-based design optimisation', *Int. J. Prod. Dev.*, vol. 5, no. 1/2, p. 76, 2008, doi: 10.1504/IJPD.2008.016371.
[84] M. N. Hegde, 'Probabilistic Sensitivity Analysis Methods for Design under Uncertainty: Probabilistic Model Reduction', in *New Horizons and Better Practices*, Long Beach, California, United States: American Society of Civil Engineers, Oct. 2007, pp. 1–10. doi: 10.1061/40946(248)102.
[85] P. Finocchi, V. Zaccaria, M. L. Ferrari, and D. Tucker, 'Optimization Under Uncertainties of a Biogas-Fueled SOFC-GT Hybrid System', in *Volume 4: Cycle Innovations; Cycle Innovations: Energy Storage*, Rotterdam, Netherlands: American Society of Mechanical Engineers, Jun. 2022, p. V004T06A017. doi: 10.1115/GT2022-81785.
[86] G. F. Franklin, J. D. Powell, and A. Emami-Naeini, *Feedback control of dynamic systems*, Eighth edition. Ny, NY: Pearson, 2019.
[87] A. D. Le, S. B. Beale, and J. G. Pharoah, 'Validation of a Solid Oxide Fuel Cell Model on the International Energy Agency Benchmark Case with Hydrogen Fuel', *Fuel Cells*, vol. 15, no. 1, pp. 27–41, Feb. 2015, doi: 10.1002/fuce.201300269.
[88] X. J. Luo and K. F. Fong, 'Investigation on part-load performances of combined cooling and power system primed by solid oxide fuel cell with different bottoming cycles', *J. Power Sources*, vol. 429, pp. 127–148, Jul. 2019, doi: 10.1016/j.jpowsour.2019.04.095.
[89] X. J. Luo and K. F. Fong, 'Development of 2D dynamic model for hydrogen-fed and methane-fed solid oxide fuel cells', *J. Power Sources*, vol. 328, pp. 91–104, Oct. 2016, doi: 10.1016/j.jpowsour.2016.08.005.
[90] H. Nabielek, 'SOFC Research in International Cooperation: The IEA SOFC Annex', *ECS Proc. Vol.*, vol. 1997–40, no. 1, pp. 26–34, Jan. 1997, doi: 10.1149/199740.0026PV.
[91] E. Ruiz-Trejo, N. P. Brandon, and P. Boldrin, Eds., *Solid oxide fuel cell lifetime and reliability: critical challenges in fuel cells*. Oxford: Academic Press, 2017.
[92] G. G. Kulikov and H. A. Thompson, Eds., *Dynamic Modelling of Gas Turbines*. in Advances in Industrial Control. London: Springer London, 2004. doi: 10.1007/978-1-4471-3796-2.
[93] Q. Cai, D. J. L. Brett, D. Browning, and N. P. Brandon, 'A sizing-design methodology for hybrid fuel cell power systems and its application to an unmanned underwater vehicle', *J. Power Sources*, vol. 195, no. 19, pp. 6559–6569, Oct. 2010, doi: 10.1016/j.jpowsour.2010.04.078.
[94] X.-J. Wu and X.-J. Zhu, 'Multi-loop control strategy of a solid oxide fuel cell and micro gas turbine hybrid system', *J. Power Sources*, vol. 196, no. 20, pp. 8444–8449, Oct. 2011, doi: 10.1016/j.jpowsour.2011.05.075.
[95] J. Chen, J. Li, D. Zhou, H. Zhang, and S. Weng, 'Control strategy design for a SOFC-GT hybrid system equipped with anode and cathode recirculation ejectors', *Appl. Therm. Eng.*, vol. 132, pp. 67–79, Mar. 2018, doi: 10.1016/j.applthermaleng.2017.12.079.
[96] Department of Electrical Engineering. University of Rome." *et al.*, 'Modelling and simulation of hybrid SOFC-GT systems for distributed generation', *Renew. Energy Power Qual. J.*, vol. 1, no. 05, pp. 243–250, Mar. 2007, doi: 10.24084/repqj05.261.
[97] K. Sedghisigarchi and A. Feliachi, 'Control of grid-connected fuel cell power plant for transient stability enhancement', in *2002 IEEE Power Engineering Society Winter Meeting. Conference Proceedings (Cat. No.02CH37309)*, New York, NY, USA: IEEE, 2002, pp. 383–388. doi: 10.1109/PESW.2002.985024.
[98] 'Dynamic Simulation of an Integrated Solid Oxide Fuel Cell System Including Current-Based Fuel Flow Control', *J. Fuel Cell Sci. Technol.*.
[99] Mathworks Inc., 'Brayton Cycle (Gas Turbine)'. [Online]. Available: https://uk.mathworks.com/help/hydro/ug/sscfluids_brayton_cycle.html
[100] T. Choudhary, M. Sahu, and S. Krishna, 'Thermodynamic Analysis of Solid Oxide Fuel Cell Gas Turbine Hybrid System for Aircraft Power Generation', presented at the AeroTech Congress & Exhibition, Sep. 2017, pp. 2017-01–2062. doi: 10.4271/2017-01-2062.
[101] D. Saebea, Y. Patcharavorachot, S. Assabumrungrat, and A. Arpornwichanop, 'Analysis of a pressurized solid oxide fuel cell–gas turbine hybrid power system with cathode gas recirculation', *Int. J. Hydrog. Energy*, vol. 38, no. 11, pp. 4748–4759, Apr. 2013, doi: 10.1016/j.ijhydene.2013.01.146.

[102] C. Bao, Y. Wang, D. Feng, Z. Jiang, and X. Zhang, 'Macroscopic modeling of solid oxide fuel cell (SOFC) and model-based control of SOFC and gas turbine hybrid system', *Prog. Energy Combust. Sci.*, vol. 66, pp. 83–140, May 2018, doi: 10.1016/j.pecs.2017.12.002.
[103] S. Haugwitz, 'Modelling of microturbine systems', in *2003 European Control Conference (ECC)*, Cambridge, UK: IEEE, Sep. 2003, pp. 1234–1239. doi: 10.23919/ECC.2003.7085129.
[104] J. Chen, M. Liang, H. Zhang, and S. Weng, 'Study on control strategy for a SOFC-GT hybrid system with anode and cathode recirculation loops', *Int. J. Hydrog. Energy*, vol. 42, no. 49, pp. 29422–29432, Dec. 2017, doi: 10.1016/j.ijhydene.2017.09.165.
[105] D. McLarty, J. Brouwer, and S. Samuelsen, 'Fuel cell–gas turbine hybrid system design part II: Dynamics and control', *J. Power Sources*, vol. 254, pp. 126–136, May 2014, doi: 10.1016/j.jpowsour.2013.11.123.
[106] E. Tsoutsanis and N. Meskin, 'Dynamic performance simulation and control of gas turbines used for hybrid gas/wind energy applications', *Appl. Therm. Eng.*, vol. 147, pp. 122–142, Jan. 2019, doi: 10.1016/j.applthermaleng.2018.09.031.
[107] T. Giampaolo, *Gas turbine handbook: principles and practice*, 5th edition. Lilburn, GA: The Fairmont Press, Inc., CRC Press, Taylor & Francis Group, 2014.
[108] W. Zhang, L. Chen, and F. Sun, 'Power and efficiency optimization for combined Brayton and inverse Brayton cycles', *Appl. Therm. Eng.*, vol. 29, no. 14–15, pp. 2885–2894, Oct. 2009, doi: 10.1016/j.applthermaleng.2009.02.011.
[109] S. C. Gülen, *Gas Turbines for Electric Power Generation*, 1st ed. Cambridge University Press, 2019. doi: 10.1017/9781108241625.
[110] J. Chen, Y. Li, H. Zhang, and S. Weng, 'Comparison of different fuel cell temperature control systems in an anode and cathode ejector-based SOFC-GT hybrid system', *Energy Convers. Manag.*, vol. 243, p. 114353, Sep. 2021, doi: 10.1016/j.enconman.2021.114353.
[111] A. Marcellan *et al.*, 'Control Strategy for a SOFC Micro Gas Turbine Hybrid Power Plant Emulator Test Rig', in *AIAA Scitech 2019 Forum*, San Diego, California: American Institute of Aeronautics and Astronautics, Jan. 2019. doi: 10.2514/6.2019-1676.
[112] Light Duty Vehicle Performance and Economy Measure Committee, 'Recommended Practice for Measuring the Exhaust Emissions and Fuel Economy of Hybrid-Electric Vehicles, Including Plug-in Hybrid Vehicles', SAE International. doi: 10.4271/J1711_202302.
[113] J. Gonder and A. Simpson, 'Measuring and Reporting Fuel Economy of Plug-In Hybrid Electric Vehicles', *World Electr. Veh. J.*, vol. 1, no. 1, pp. 134–141, Dec. 2007, doi: 10.3390/wevj1010134.
[114] K. Yadlapati, 'Parametric study of a fuel cell plug-in hybrid electric vehicle powertrain'.
[115] S. Kang and K. Min, 'Dynamic simulation of a fuel cell hybrid vehicle during the federal test procedure-75 driving cycle', *Appl. Energy*, vol. 161, pp. 181–196, Jan. 2016, doi: 10.1016/j.apenergy.2015.09.093.
[116] K. Johansson and P. Alvfors, 'The Effect of Drive Cycles on the Performance of a PEM Fuel Cell System for Automotive Applications', presented at the Automotive and Transportation Technology Congress and Exposition, Oct. 2001, pp. 2001-01–3454. doi: 10.4271/2001-01-3454.
[117] T. D. Gillespie, *Fundamentals of vehicle dynamics*, Revised edition. Warrendale, Pennsylvania, USA: SAE International, 2021.